Lagrangian Analysis Methodology for Power Electronics and Its Application to Industry

July 2015

Kazuhiro Umetani

Interdisciplinary Graduate School of Science and Engineering, Shimane University

TABLE OF CONTENTS

PREFACE

Applications of power electronics are growing fast in industry. Accordingly, technological fields of power electronics is also expanding. Conventionally, power electronics researches are mainly targeted on basic power converter circuits and basic motors. The basic power converters are composed of basic circuit elements, such as transformers, inductors, capacitors, switches, and rectifiers. The basic motors have linear electric characteristics, which can be modeled by basic linear lumped circuit elements. Therefore, these basic techniques are commonly analyzed using the circuit theory. However, recent researches include various techniques that are difficult to analyze using the circuit theory.

Many of these recent techniques appear to contain some keywords that explains the difficulty. Below this thesis gives three typical keywords.

The first keyword is electromagnetic field application.

Some applications utilize the electromagnetic field itself for their industrial purposes. For example, induction heating [1]–[3] utilizes the magnetic field not for obtaining reactance but for inducing eddy current in the object to be heated. Wireless power transfer [4]–[6] also utilizes the electric or magnetic field not for reactance but for energy transfer. Induction heating and wireless power transfer generally need analyses of the behavior of the electromagnetic field to design effective work coils and transmitters/receivers. However, the circuit theory can be hardly employed for calculation of the electromagnetic field.

Integrated magnetic components [7]–[16] are another technique that shares this keyword. They utilize the magnetic field for implementing advanced electric functions. They generally have multiple magnetic couplings with complicated relations between the flux linkage and the magnetomotive force. They are known to be useful for miniaturizing magnetic components [7][8][11] or reducing the copper loss [9]. However, in many cases, the electric circuits with integrated magnetic components are difficult to analyze by the circuit theory because these circuits require calculation of the magnetic behavior as well as the electric behavior.

The second keyword is non-linearity.

Some applications utilize devices with significant electromagnetic non-linearity. For example, the switched reluctance motors [17]–[19] show intense non-linearity because driving the motor generally saturates the magnetic core. This motor utilizes magnetic saturation to achieve higher efficiency. However, magnetic saturation in the motor is difficult to consider in the circuit theory because magnetic saturation is dependent not on the current but on the magnetic flux, which is not concretely calculated in the circuit theory. Certainly, the magnetic saturation can be considered in the circuit theory as decrease of inductance as a function of the current, if there is one flux path as in the simple inductor. However, this approach is not necessarily applicable to the switched reluctance motors, which generally have more complicated dependencies of the torque output on the

magnetic flux of the multiple windings. Therefore, the circuit theory can be hardly applied directly to developing driving techniques of the switched reluctance motors.

The third keyword is system integration.

In recent applications, a number of power converters and motors are often integrated to form a system. The system often require control techniques that optimizes the behavior of both the entire system and each subsystem that constitutes the system. In many cases, the system includes mechanical subsystems, which does not belong to the power electronics. For example, propulsion systems [20][21] of electrified vehicles have multiple power converters and motors. A propulsion system generally contains the battery, the DC-DC converter, the inverter, and the motor. Furthermore, the system also contains mechanical system that transfer the torque to the wheels. Therefore, analysis of the entire vehicle propulsion system is difficult by the circuit theory because the behavior of the system depends on both the mechanics and the power electronics.

As we have seen, the difficulties related to the three keywords appear to be originated to the fact that the circuit theory does not directly analyze the electromagnetism and the mechanics. Hence, these difficulties may be alleviated by an analytical technique that can cover the electromagnetism and the mechanics simultaneously.

The purpose of this thesis is to propose novel analytical methodology to address these difficulties. The proposed methodology is based on Lagrangian dynamics [22][23].

Lagrangian dynamics is one of the most basic analytical tools of the physics. Lagrangian dynamics directly utilizes the principle of the least action [24], which is the basic rule applicable to any types of physical systems. Therefore, Lagrangian dynamics has an attractive feature that it can analyze both the electromagnetic systems and the mechanical systems. Lagrangian dynamics can also be applied to non-linear magnetic field as shown in Chapter 4 of this thesis. Furthermore, Lagrangian dynamics can be applied to systems that incorporates both the electromagnetism and the mechanics, such as a motor driving system. Therefore, Lagrangian dynamics may solve the above mentioned difficulties of the power electronics.

Lagrangian dynamics has already been widely utilized in mechanical systems. In addition, some preceding works [25]–[29] have proposed the method to formulate Lagrangian models for basic power conversion circuits composed of basic lumped circuit elements, such as the inductor, the capacitor, and the switches. However, the preceding method has hardly been applied to more complicated electromagnetic systems including complicated or non-linear magnetics and mechanics. Furthermore, few examples are known to show how to apply Lagrangian dynamics to practical industrial applications.

Therefore, this thesis first proposes the Lagrangian methodology for the power electronics in Part I. Specifically, this thesis presents a set of basic theoretical methods to apply Lagrangian dynamics to power electronics researches. These methods are intended to address difficulties related to the above mentioned three keywords. Part I consists of Chapter 1–4. Chapter 1 presents a generalized Lagrangian modeling method applicable to power converters with complicated magnetics. Chapter 2 derives methods to analyze integrated magnetic components. Therefore, Chapter 1 and Chapter 2 are related to the difficulties of the first keyword, i.e. the electromagnetic field application. Chapter 3 derives a method of the duality transformation [30] based on the correspondence relation between the electricity and the magnetic flux. Therefore, this chapter is also related to the

first keyword. Chapter 4 derives a Lagrangian modeling method of switched reluctance motor and its propulsion system, which is related to the second and third keywords, i.e. the non-linearity and the system integration.

Then, this thesis presents three applications of the Lagrangian methodology to practical power electronics in Part II. Part II consists of Chapter 5–7. Chapter 5 and Chapter 6 contain integrated magnetic components. Therefore, the two applications are related to the first keyword. Chapter 7 proposes a control technique for a synchronous buck converter. This technique is derived by investigating the Lagrangian model incorporating the converter and the load as one system. Hence, this application is related to the third keyword.

The followings present digests of the chapters.

Chapter 1 provides the most basic method for Lagrangian dynamics of the power electronics. This chapter formulates a generalized method to compose Lagrangian models of static power converter circuits. Although some preceding works [25]–[29] have discussed Lagrangian modeling of power converter circuits composed of basic circuit elements, the proposed method can further be applied to modeling of complicated magnetic circuits. Therefore, the proposed method can be used for analyses of the integrated magnetic components. This chapter also presents an example that shows systematic analysis of the circuit behavior of a power converter with an integrated magnetic component.

Chapter 2 proposes a novel method utilizing Lagrangian dynamics to derive equivalent circuits of integrated magnetic components for easier comprehension of the components. Conventionally, two methods have been known to derive equivalent circuits: The inductance matrix method [31] and the duality method [32][33]. However, the inductance matrix method generally suffers from complicated derivation procedure; and the duality method generally suffers from complicated resultant equivalent circuits. On the other hand, the proposed method provides a straightforward and systematic procedure that is applicable to all integrated magnetic components. Furthermore, the proposed method can derive simpler equivalent circuits at least in some cases. In fact, Chapter 2 presents an example in which the proposed method successfully derived the simplest equivalent circuit compared with the conventional methods.

Chapter 3 proposes a novel method for the duality transformation [30]. The duality transformation is a process to transform a voltage-source converter into a dynamically equivalent current-source converter, and vice versa. Conventionally, the duality transformation is performed based on the topological transformation, which replaces series connections of the original circuits by parallel connections and parallel connections by series connections. However, the topological transformation can be applied only to planar circuits [30]. Therefore, the conventional method of the duality transformation cannot be directly applicable to non-planar circuits. Certainly, some methods [34]–[37] are proposed for the duality transformation of non-planar circuits. However, these methods can suffer from the complicated procedure; and furthermore they often suffer from different results, which cannot be derived by the other methods. This difficulty is addressed by the proposed method, which utilizes Lagrangian dynamics to avoid topological transformation. Along with the theory of the proposed method, Chapter 3 also presents an example of the duality transformation of a basic non-linear circuit to show that the proposed method is directly applicable to non-planar circuits.

Chapter 4 presents a method to compose Lagrangian model of switched reluctance motors. The proposed method can model the intense magnetic non-linearity of the switched reluctance motors. Certainly, many preceding analytical model [38]–[42] can also model this non-linearity. However, the Lagrangian model composed using the proposed method can be directly connected to the mechanical model of the load and the Lagrangian model of the power converters, which is discussed in Chapter 1, to form a Lagrangian model of the entire motor drive system including mechanical load. In fact, Chapter 4 presents an example of operation analysis of a simple switched reluctance motor drive system to show that the Lagrangian model of the entire system can be easily obtained by summing Lagrangian models of the constituents of the system.

Chapter 5 presents an application of the methods presented in Chapter 1 and Chapter 2. The integrated magnetic components are expected to miniaturize EMC filters. However, this technique also has a risk that lowers tolerance to the magnetic saturation, which may reduce the miniaturization effect by the magnetic integration. This chapter addresses this problem by proposing a novel integrated magnetic component that improves the tolerance to the magnetic saturation. A theoretical analysis and experiments verified that the proposed structure is equivalent to an EMC filter of series-connected differential-mode and common-mode inductors. Additionally, an analytical estimation revealed that the proposed structure successfully reduced the core volume compared with a conventional integrated magnetic component.

Chapter 6 also presents an application of the methods presented in Chapter 1 and Chapter 2. This chapter targets on the soft-switching technique [43]–[49]. This chapter proposes a novel soft-switching boost chopper with an integrated magnetic component. The integrated magnetic component is utilized for miniaturizing a novel lossless LC snubber in the proposed chopper which achieves the zero-current switching turn-on and the zero-voltage switching turn-off. This chapter shows how this integrated magnetic component works in the lossless LC snubber, as well as the merits and drawbacks of the proposed soft-switching boot chopper compared with various conventional boost chopper topologies. This chapter also presents experimental results that verifies the operating principles of the proposed boost chopper.

Chapter 7 presents an application of the method presented in Chapter 1. Similarly to the method presented in Chapter 2, this chapter utilizes the point transformation [50] of the Lagrangian model. Sliding-mode control for buck converters [51] is beneficial in fast transient response to a step load change in wide operating range. However, buck converters can further require better dynamic load regulation against load current fluctuations within the response speed of the converters. This chapter addresses this issue by proposing a novel control method for synchronous buck converters [52][53] using Lagrangian dynamics. Along with the theoretical derivation of the control method, this chapter also presents simulation results that successfully verified improvement in the dynamic load regulation against sinusoidal load current fluctuations.

Finally, conclusions are given to the thesis.

REFERENCES

[1] J. M. Burdio, F. Monterde, and J. R. Garcia, "A two-output series-resonant inverter for induction-heating cooking appliances," *IEEE Trans. Power Electron.*, vol. 20, no. 4, pp. 815-822, Jul. 2005.

[2] H. Fujita, N. Uchida, and K. Ozaki, "A new zone-control induction heating system using multiple inverter units applicable under mutual magnetic coupling conditions," *IEEE Trans. Power Electron.*, vol. 26, no. 7, pp. 2009-2017, Jul. 2011.

[3] H. Samago, A. Mediano, and O. Lucia, "High efficiency AC–AC power electronic converter applied to domestic induction heating," *IEEE Trans. Power Electron.*, vol. 27, no. 8, pp. 3676-3684, Aug. 2012

[4] J. O. Mur-Miranda, G. Fanti, Y. Feng, K. Omanakutta, R. Ongie, A. Setjoadi and N. Sharpe, "Wireless power transfer using weakly coupled magnetostatic resonators", in *Proc. Energy Conversion Congr. Expo.*, 2010, pp. 4179-4186.

[5] T. Imura and H. Yoichi, "Maximizing air gap and efficiency of magnetic resonant coupling for wireless power transfer using equivalent circuit and neumann formula", *IEEE Trans. Ind. Appl.*, vol. 58, no. 10, pp. 4746-4752, Oct. 2011.

[6] S. Y. R. Hui, W. Zhong, C. K. Lee, "A critical review of recent progress in mid-range wireless power transfer," *IEEE Trans. Power Electron.*, vol. 29, no. 9, pp. 4500-4511, Sept. 2014.

[7] P. Zumel, O. Garcia, J. A. Cobos, and J. Uceda, "Magnetic integration for interleaved converters," in *Proc. Appl. Power Electron. Conf. Expo.*, 2003, vol. 2, pp. 1143-1149.

[8] S. Chandrasekaran and L. U. Gokdere, "Integrated magnetics for interleaved DC-DC boost converter for fuel cell powered vehicles," in *Proc. Power Electronics Specialists Conf.*, 2004, pp. 356-361.

[9] Wei Wen, and Y.-S. Lee, "A two-channel interleaved boost converter with reduced core loss and copper loss," in *Proc. Power Electronics Specialists Conf.*, 2004, pp. 1003-1009.

[10] N. Zhu, J. Kang, D. Xu, B. Wu, and Y. Xiao, "An integrated AC choke design for common-mode current suppression in neural-connected power converter systems," *IEEE Trans. Power Electron.*, vol. 27, no. 3, pp. 1228-1236, Mar. 2012.

[11] W. Li, P. Li, H. Yang, and X. He, "Three-level forward-flyback phase-shift ZVS converter with integrated series-connected coupled inductors," *IEEE Trans. Power Electron.*, vol. 27, no. 6, pp. 2846-2856, Jun. 2012.

[12] W. Li, P. Li, H. Yang, and X. He, "Three-level forward-flyback phase-shift ZVS converter with integrated series-connected coupled inductors," *IEEE Trans. Power Electron.*, vol. 27, no. 6, pp. 2846-2856, Jun. 2012.

[13] K. J. Hartnett, J. G. Hayes, M. G. Egan, and M. S. Rylko, "CCTT-core split-winding integrated magnetic for high-power DC-DC converters," *IEEE Trans. Power Electron.*, vol. 28, no. 11, pp. 4970-4984, Nov. 2013.

[14] C. Deng, D. Xu, P. Chen, C. Hu, W. Zhang, Z. Wen, and X. Wu, "Integration of both EMI filter and boost inductor for 1kW PFC converter," *IEEE Trans. Power Electron.*, vol. PP, issue 99, pp. 1, 2014

[15] K. Umetani, F. Iwamoto, and K. Yagyu , "A unidirectional boost chopper with snubber energy regeneration using a coupled inductor," *IEEJ Trans. Elect. Electron. Eng.*, vol 9, no. 3, pp. 315-323, May 2014.

[16] K. Umetani, T. Tera, K. Shirakawa, "A Magnetic Structure Integrating Differential-Mode and Common-Mode Inductors with Improved Tolerance to DC Saturation," *IEEJ J. Ind. Appl.*, vol. 4, no. 3, pp. 166-173, May 2015.

[17] Z. Q. Zhu, C. C. Chan, "Electrical machine topologies and technologies for electric, hybrid, and fuel cell vehicles", in *Proc. IEEE Vehicle Power Propulsion Conf.*, Harbin, China, 2008, pp. 1–6.

[18] D. Panda and V. Ramanarayanan, "Reduced acoustic noise variable DC-bus-voltage-based sensorless switched reluctance motor drive for HVAC applications," *IEEE Trans. Ind. Electron.*, vol. 54, no. 4, pp. 2065-2078, Aug. 2007.

[19] W. Suppharangsan and J. Wang, "Experimental validation of a new switching technique for DC-link capacitor minimization in switched reluctance machine drives," in *Proc. IEEE Intl. Elect. Mach. Drives Conf.*, Chicago, USA, 2013, pp. 1031–1036.

[20] A. Emadi, S. S. Wiliamson, and A. Khaligh, "Power electronics intensive solutions for advanced electric, hybrid electric, and fuel cell vehicular power system," *IEEE Trans. Power Electron.*, vol. 21, no. 3, pp.567-577, May 2006.

[21] M. R. Nikzad and A. Radan, "effects of fuel cell and dc-link voltage on boost converter efficiency in fuel cell-battery hybrid vehicles," in *Proc. IEEE Intl. Power Electron. Motion Control Conf. (IPEMC)*, Wuhan, China, 2009, pp.2313-2317.

[22] D. A. Wells, "Applications of Lagrange's equations to electrical and electromechanical systems," in *Schaum's Outline of Theory and Problems of Lagrangian Dynamics*, New York: McGraw-Hill, 1976, pp.302-315.

[23] K. Kawamura, *Electromagnetism*. Tokyo, Japan: Iwanami, 1994, pp.218-223. (in Japanese)

[24] L. D. Landau and E. M. Lifshitz, "The equations of motion" in *Mechanics*, Oxford, U. K.: Butterworth- Heinemann, 1976, pp.1-8.

[25] H. Sira-Ramírez, R. Ortega, and G. Escobar, "Lagrangian modeling of switch regulated DC-to-DC power converters," in Proc. 35th Conf. Decision Control, 1996, vol. 4, pp. 4492-4496.

[26] H. Sira-Ramírez and M. D. de Nieto, "A Lagrangian approach to average modeling of pulsewidth-modulation controlled DC-to-DC power converters," *IEEE Trans. Circuits Syst. I*, vol. 43, no. 5, pp. 427-430, May 1996.

[27] J. M. A. Scherpen, D. Jeltsema, and J. B. Klaasens, "Lagrangian modeling of switching electrical networks," *Syst. Control Lett.*, vol. 48, pp. 365-374, April 2003.

[28] J. Clemente-Gallardo and J. M. A. Scherpen, "Relating Lagrangian and Hamiltonian formalisms of LC circuits," *IEEE Trans. Circuits Syst. I*, vol. 50, no. 10, pp. 1359-1363. Oct. 2003.

[29] T. S. Lee, "Lagrangian modeling and passivity-based control of three-phase AC/DC voltage-source converters," *IEEE Trans. Ind. Electron.*, vol. 51, no. 4, pp. 892-902, Aug. 2004.

[30] S. D. Freeland, "Techniques for the practical application of duality to power circuits," IEEE Trans. Power Electron., vol. 7, no. 2, pp. 374-384, April 1992.

[31] M. Nakahama, M. Yamamoto, and Y. Satake, "Trans-linked multi-phase boost converter for electric vehicle," in *Proc. Energy Conversion Congr. Expo.*, 2010, Atlanta, pp. 2458-2463.

[32] S. A. El-Hamamsy and E. I. Chang, "Magnetics modeling for computer-aided design of power electroncs circuits," in *Proc. Power Electron. Specialist Conf. (PESC)*, 1989, vol. 2, pp. 635-645.

[33] G. W. Ludwig and S. A. El-Hamamsy, "Coupled inductor and reluctance models of magnetic components," *IEEE Trans. Power Electron.*, vol. 6, no. 2, pp. 240-250, April 1991.

[34] B. A. Bloch, "On method for the construction of networks dual to non-planar networks," in *Proc. Phys. Soc.*, 1946, vol. 58, pp. 677-694.

[35] P. J. Wolfs, G. F. Ledwich, and K. C. Kwong, "The application of the duality principle to nonplanar circuits", *IEEE Trans. Power Electron.*, vol. 8, no. 2, pp. 104-111, April 1993.

[36] J. W. Kolar, H. Ertl, and F. C. Zach, "Analysis of the duality of three phase PWM converters with DC voltage link and DC current link," in *Proc. Ind. Appl. Soc. Annu. Meeting*, 1989, vol. 1, pp. 724-737.

[37] M. Bierhoff, F. W. Fuchs, and S. Pischke, "Theoretical output current spectra of three phase current source converters," in *Proc. Europ. Conf. Power Electron. Appl. (EPE)*, 2005, pp. P1-P9.

[38] D. N. Essah and S. D. Sudhoff, "An improved analytical model for the switched reluctance motor," *IEEE Trans. Energy Convers.*, vol. 18, no. 3, pp. 349-356, Sept. 2003.

[39] M. Farshad, J. Faiz, and C. Lucas, "Development of analytical models of switched reluctance motor in two-phase excitation mode: extended miller model," *IEEE Trans. Magn.*, vol. 41, no. 6, pp. 2145-2155, Jun. 2005.

[40] A. Khalil and I. Husain, “A fourier series generalized geometry-based analytical model of switched reluctance machines,” *IEEE Trans. Ind. Appl.*, vol. 43, no. 3, pp. 673-684, May/Jun. 2007.

[41] H. Chen, D. Jiang, J. Yang, and L. Shi, “A new analytical model for switched reluctance motors,” *IEEE Trans. Magn.*, vol. 45, no. 8, pp. 3107–3113, Aug. 2009.

[42] D. Lin, P. Zhou, S. Stanton, and Z. J. Cendes, “An analytical circuit model of switched reluctance motors,” *IEEE Trans. Magn.*, vol. 45, no. 12, pp. 5368–5375, Aug. 2009.

[43] P. S. G. Giacomini, J. S. Scholtz, and M. Mezaroba, “Step-up / step-down DC-DC ZVS PWM converter with active clamping,” *IEEE Trans. Ind. Electron.*, vol. 55, no. 10, pp.3635-3643. Oct. 2008.

[44] W. Li, W. Li, Y. Deng, and X. He, “Single-stage single-phase high-step-up ZVT boost converter for fuel-cell microgrid system,” *IEEE Trans. Ind. Electron.*, vol. 25, no. 12, pp.3057-3065, Dec. 2010.

[45] J. Bauman and M. Kazerani, “A novel capacitor-switched regenerative snubber for DC/DC boost converters,” *IEEE Trans. Ind. Electron.*, vol. 58, no. 2, pp.514-523, Feb. 2011.

[46] J. P. Gegner and C. Q. Lee, “Zero-voltage-transition converters using an inductor feedback technique,” in *Proc. IEEE Appl. Power Electron. Conf. Expo.(APEC)*, Orlando, Florida, USA, 1994, vol. 2, pp.862-868.

[47] R. L. Lin, Y. Zhao, and F. C. Lee, “Improved soft-switching ZVT converters with active snubber,” in *Proc. IEEE Appl. Power Electron. Conf. Expo.(APEC)*, Anaheim, California, USA, 1998, vol. 2, pp.1063-1069.

[48] X. Wu, X. Jin, L. Huang, and G. Feng, “A lossless snubber for DC/DC converters and its application in PFC,” in *Proc. IEEE Intl. Power Electron. Motion Control Conf. (IPEMC)*, Beijing, China, 2000, vol. 3, pp.1144-1149.

[49] M. Nakamura, T. Myoui, M. Ishitobi, and M. Nakaoka, “A soft-switching PWM boost chopper controlled DC-DC converter with a single passive auxiliary resonant snubber and its performance evaluation”, *IEEJ Trans. Ind. Appl.*, vol. 122-D, no. 10, pp.1006-1016, 2002. (in Japanese)

[50] L. D. Landau and E. M. Lifshitz, “Canonical tranformations” in *Mechanics*, Oxford, U. K.: Butterworth- Heinemann, 1976, pp.143-146.

[51] S. C. Tan, Y. M. Lai, and C. K. Tse, “General design issues of sliding-mode controllers in DC-DC converters,” *IEEE Trans. Ind. Electron.*, vol. 55, no. 3, pp. 1160-1174, Mar. 2008.

[52] M. Castilla, L. G. de Vicuna, J. M. Guerrero, J. Miret, and N. Berbel, “Simple low-cost hysteretic controller for single-phase synchronous buck converters,” *IEEE Trans. Power Electron.*, vol. 22, no. 4, pp. 1232-1241, Jul. 2007.

[53] M. Orabi and A. Shawky, “Proposed Switching Losses Model for Integrated Point-of-Load Synchronous Buck Converters,” IEEE Trans. Power Electron., vol. 30, no. 9, pp. 5136-5149, Sept. 2015.

PART I:

Lagrangian Analytical Methodology for Power Electonics

Chapter 1

GENERALIZED LAGRANGIAN CIRCUIT THEORY OF STATIC POWER CONVERSION CIRCUIT

1.1. Introduction

This chapter derives a Lagrangian modeling applicable to both electric and magnetic circuits. Power electronics theories have been mainly based on analysis of an electric circuit because basic power converters are composed of simple electric components such as capacitors, inductors, transformers, switches, and diodes. Certainly, inductors and transformers have magnetic circuits [1]. However, their magnetic circuits are simple enough to regard them as black boxes and model their electric functions by simple voltage-current relations. As a result, we can analyze operation of basic power converters entirely using the electric circuit theory.

However, recent growing requirement for miniaturization and efficiency improvement attracts researchers' attention to magnetic components with complicated magnetic circuits. These components are generally referred to as integrated magnetic components [2]–[26].

Application of integrated magnetic components is a useful remedy for reducing both the volume and the energy loss of magnetic components. An integrated magnetic component can integrate plural individual inductors and transformers onto a single magnetic core. In a well-designed component, each inductor or transformer shares its magnetic path and winding with others, thus reducing the total amount of core [3], [4], [20] and copper [5] in the circuit. In addition, the dead space between magnetic components may also be reduced by the integration.

The cutback in core and copper contributes to reducing not only volume but also energy loss. Because the iron loss and the copper loss are generated in the core and the windings, their cutback generally leads to reducing the energy loss. Owing to these benefits, industrial applications of the integrated magnetic components are energetically proposed and studied in the number of cases [2]–[26].

On the other hand, integrated magnetic components have been rarely employed in practical uses. A probable reason may lie in the fact that analytical comprehension of the circuit behavior of the components is difficult in the conventional electric circuit theory because their voltage –current relation is not simple due to their complicated magnetic circuit structure.

Certainly, some latest simulators can predict precise behaviors of the integrated magnetic components, as shown in [2], [6]. Contrarily, analytical methods are hardly employed for non-linear behaviors in general. Nonetheless, the analytical methods can ensure circuit behaviors for any possible conditions, whereas the numerical results are

[†] Reprinted, with permission, from K. Umetani, A generalized method of Lagrangian modeling of power conversion circuit with integrated magnetic components, IEEJ Transactions on Electrical and Electronic Engineering, Nov 2012.

valid for specific operating conditions. Hence, analytical methods still play an important role in circuit analysis.

Power converters with integrated magnetic components can be analyzed directly by solving the electric circuits and the magnetic circuits individually and then integrating the results to obtain one solution. Examples of this approach are presented in [2]–[5], [7], [14], [17], [19], [21]. However, this brute-force analysis tends to be complicated compared to that only of electric circuits. Instead, multiple analytical methods that models electric functions of magnetic circuits have been proposed in order to allow the electric circuit theory to handle the integrated magnetic components.

These methods can be classified into two major categories. One is the inductance matrix [8], [27]; and the other is the gyrator-capacitor modeling [6], [28]. However, neither of them necessarily provide a simple and systematic procedure, particularly when applied to highly integrated magnetic components.

The former theory expresses a magnetic circuit by an inductance matrix [13] composed of the self-inductance of all windings and the mutual inductance [29] of all winding pairs. If the theory is applied to a single flux path, such as a basic transformer, the matrix can be easily found. However, as for a more complicated magnetic circuit, determining the matrix is generally difficult because of its great dimension and poor correspondence relation between the physical magnetic structure and the matrix elements. To summarize, the complicated modeling procedure, as well as poor correspondence relation, can hinder straightforward analysis of the circuit behavior.

The latter method converts a magnetic circuit into an electric circuit with gyrators [30]. Unlike electric components in a real circuit, a gyrator is a non-reciprocal component whose impedance matrix is asymmetric. Because the model does not belong to a real electric circuit, its analysis is generally difficult. In addition, the gyrator-capacitor modeling is limited to an integrated magnetic component whose winding interlinks with a single magnetic path. This limitation hinders modeling leakage flux. Hence, if we consider leakage flux, we need to convert in advance the physical magnetic structure into another that allow the modeling method. To summarize, the difficulty in analysis and the limitation of modeling can hinder straightforward analysis of the circuit behavior.

As we have seen, these two methods expand the electric circuit theory to analyze integrated magnetic components. However, this approach seems to result in complicated handling of a magnetic circuit. Another promising approach may lie in reconstructing a circuit theory that naturally incorporates both electric circuits and magnetic circuits.

The purpose of this chapter is to derive this novel circuit theory through simplification of the electromagnetism. For the straightforward simplification, great concern should be paid on the features of the intended system. The integrated magnetic components are expected to be applied to power conversion circuits, i.e. energy conserving systems. In this respect, the Lagrangian dynamics seems to be a promising candidate for the simplification method.

In [31]–[36], the Lagrangian dynamics has been applied to power converters without integrated magnetic components. However, their Lagrangian is based rather on the analogical relation between electric circuit and mechanics. For example, an inductor is regarded as mass, a capacitor as a spring, and charge as position. Because they do not contain magnetism in the concrete manner, the above-mentioned difficulty remains

unsolved. Indeed, the inductance matrix is utilized in [33], [34], which discuss handling integrated magnetic components using Lagrangian dynamics.

In contrast to these preceding Lagrangian theories, this chapter proposes a novel Lagrangian theory that is naturally applicable to integration of both electric circuits and magnetic circuits. We will begin our discussion with expressing the electromagnetic field in Lagrangian dynamics. Through simplification of the electromagnetism, we obtain the novel circuit theory in the second section.

For convenience, we limit our discussion to linear media in this chapter because analytical methods are usually applied to the linear behavior of a circuit in practice. As a result, we ignore the non-linear characteristic of magnetic material, such as magnetic saturation, hysteresis, and the dependency of the B-H curve on frequency. Accordingly, we also ignore non-linearity dependent on geometry of a core, which is caused by the non-linearity of the material and local flux distribution inside the core [37].

In the third section, an example of a circuit analysis is presented. The example shows the systematic method to derive the state-space model of a converter with an integrated magnetic component. From the state-space model, we can easily obtain the circuit behavior.

1.2. Lagrangian Modeling

A. Lagrangian Expression for Electromagnetism in Linear Media

Let us assume that the intended circuit, along with the media of electric and magnetic field, remains at rest in a coordinate system. Additionally we assume the linear media. Then the field in the coordinate is described by following Maxwell equations [38].

$$\mathrm{div}(\varepsilon\mathbf{E}) = \rho, \tag{1.1}$$

$$\mathrm{rot}\,(\mathbf{B}/\mu) - \partial(\varepsilon\mathbf{E})/\partial t = \mathbf{j}, \tag{1.2}$$

$$\mathrm{div}\mathbf{B} = \mathbf{0}, \tag{1.3}$$

$$\mathrm{rot}\mathbf{E} = -\partial\mathbf{B}/\partial t, \tag{1.4}$$

where **E** is electric field, **B** is flux density, ε is permittivity, μ is permeability, ρ is electric charge, **j** is current density vector.

By introducing scalar potential ψ and vector potential **A** defined as (1.5) and (1.6) and substituting them for **E** and **B**, we can omit (1.3) and (1.4) because they are always satisfied.

$$\mathbf{B} = \mathrm{rot}\mathbf{A} \tag{1.5}$$

$$\mathbf{E} = -\mathrm{grad}\,\psi - \partial\mathrm{A}/\partial t \tag{1.6}$$

The Maxwell equations in a vacuum are known to be derived by applying the following Lagrangian density L_{d0} to the variational principle [39]:

$$L_{d0} = -\rho\psi + \mathbf{j}\cdot\mathbf{A} + \frac{\varepsilon_0}{2}\mathbf{E}^2 - \frac{1}{2\mu_0}\mathbf{B}^2 \tag{1.7}$$

where ε_0, μ_0 are the permittivity and the permeability of vacuum, respectively.

As (1.1) and (1.2) differ from the Maxwell equations in a vacuum only in the permittivity and the permeability, the Lagrangian density for (1.1) and (1.2) can be expressed by:

$$L_d = -\rho\psi + \mathbf{j}\cdot\mathbf{A} + \frac{\varepsilon}{2}\mathbf{E}^2 - \frac{1}{2\mu}\mathbf{B}^2. \tag{1.8}$$

The Lagrangian density L_d corresponds to that proposed by Zheng and Wang [38], if both current and density of monopole is assumed to be zero.

We can confirm that (1.8) gives the Maxwell equation of a linear media. We consider a system of electromagnetic field and integrate L_d over a large region V containing this system. Then, the result of the integration gives Lagrangian L_{tmp} of this system. Hence, we have

$$L_{tmp} = -\int_V \rho\psi d\mathbf{x} + \int_V \mathbf{j}\cdot\mathbf{A}d\mathbf{x} + \int_V \frac{\varepsilon}{2}\mathbf{E}^2 d\mathbf{x} - \int_V \frac{1}{2\mu}\mathbf{B}^2 d\mathbf{x}. \tag{1.9}$$

where $d\mathbf{x}$ is the volume element.

Next, we take the variation of L_{tmp} with respect to ψ, $\mathbf{A}$, and $\dot{\mathbf{A}}$. The variable $\dot{\mathbf{A}}$ refers to the time derivative of $\mathbf{A}$. Hereafter; we denote the time derivative of a variable by a dot over the variable. We consider arbitrary infinitesimal changes $\delta\psi$, $\delta\mathbf{A}$, and $\delta\dot{\mathbf{A}}$ in ψ, $\mathbf{A}$, and $\dot{\mathbf{A}}$, respectively, inside the region V. On the other hand, we assume $\delta\psi$=0 and $\delta\dot{\mathbf{A}} = \delta\mathbf{A} = \mathbf{0}$ at the surface of V. We replace ψ, $\mathbf{A}$, and $\dot{\mathbf{A}}$ in (1.9) by $\psi+\delta\psi$, $\mathbf{A}+\delta\mathbf{A}$ and $\dot{\mathbf{A}} + \delta\dot{\mathbf{A}}$, respectively. Then, we subtract L_{tmp} from the resultant Lagrangian $L_{tmp}+\delta L_{tmp}$ to obtain the infinitesimal change δL_{tmp} in the Lagrangian:

$$\delta L_{tmp} = -\int_V \rho\delta\psi d\mathbf{x} + \int_V \mathbf{j}\cdot\delta\mathbf{A}d\mathbf{x} + \int_V \varepsilon\mathbf{E}\cdot\delta\mathbf{E}d\mathbf{x} - \int_V \frac{\mathbf{B}}{\mu}\cdot\delta\mathbf{B}d\mathbf{x}, \tag{1.10}$$

where $\delta\mathbf{E} = -\mathrm{grad}\,\delta\psi - \delta\dot{\mathbf{A}}$ and $\delta\mathbf{B} = \mathrm{rot}\,\delta\mathbf{A}$. In the above equation, we neglect the second order of $\delta\psi$, $\delta\mathbf{A}$, and $\delta\dot{\mathbf{A}}$.

The third right-hand term can be developed as follows:

$$\int_V \varepsilon\mathbf{E}\cdot\delta\mathbf{E}d\mathbf{x} = -\int_V \varepsilon\mathbf{E}\cdot\mathrm{grad}\,\delta\psi d\mathbf{x} - \int_V \varepsilon\mathbf{E}\cdot\delta\dot{\mathbf{A}}d\mathbf{x}$$

$$= -\int_{\Omega} \varepsilon \mathbf{E}\, \delta\psi d\Omega + \int_{V} \mathrm{div}(\varepsilon \mathbf{E}) \delta\psi d\mathbf{x} - \int_{V} \varepsilon \mathbf{E} \cdot \delta\dot{\mathbf{A}} d\mathbf{x}$$

$$= \int_{V} \mathrm{div}(\varepsilon \mathbf{E}) \delta\psi d\mathbf{x} - \int_{V} \varepsilon \mathbf{E} \cdot \delta\dot{\mathbf{A}} d\mathbf{x}, \tag{1.11}$$

where Ω is the surface of the region V and $d\Omega$ is its area element.

Similarly, the fourth right-hand term in (1.10) can be developed as follows:

$$-\int_{V} \frac{\mathbf{B}}{\mu} \cdot \delta\mathbf{B} d\mathbf{x} = \int_{\Omega} \frac{\mathbf{B}}{\mu} \times \delta\mathbf{A} d\Omega - \int_{V} \mathrm{rot}\left(\frac{\mathbf{B}}{\mu}\right) \cdot \delta\mathbf{A} d\mathbf{x} = -\int_{V} \mathrm{rot}\left(\frac{\mathbf{B}}{\mu}\right) \cdot \delta\mathbf{A} d\mathbf{x}. \tag{1.12}$$

Substituting (1.11) and (1.12) into (1.10) yields

$$\delta L_{tmp} = \int_{V} \{-\rho + \mathrm{div}(\varepsilon \mathbf{E})\} \delta\psi d\mathbf{x} - \int_{V} \varepsilon \mathbf{E} \cdot \delta\dot{\mathbf{A}} d\mathbf{x} + \int_{V} \left\{ \mathbf{j} - \mathrm{rot}\left(\frac{\mathbf{B}}{\mu}\right) \right\} \cdot \delta\mathbf{A} d\mathbf{x}, \tag{1.13}$$

Hence, we obtain functional derivatives $\delta L_{tmp} / \delta\psi$, $\delta L_{tmp} / \delta\mathbf{A}$, $\delta L_{tmp} / \delta\dot{\mathbf{A}}$ as follows:

$$\frac{\delta L_{tmp}}{\delta\psi} = -\rho + \mathrm{div}(\varepsilon \mathbf{E}), \quad \frac{\delta L_{tmp}}{\delta\dot{\mathbf{A}}} = -\varepsilon \mathbf{E}, \quad \frac{\delta L_{tmp}}{\delta\mathbf{A}} = \mathbf{j} - \mathrm{rot}\left(\frac{\mathbf{B}}{\mu}\right). \tag{1.14}$$

The functional derivatives of a Lagrangian must satisfy Euler-Lagrange's equation [39]. Hence, we have

$$\frac{d}{dt}\left(\frac{\delta L_{tmp}}{\delta\dot{\mathbf{A}}}\right) - \frac{\delta L_{tmp}}{\delta\mathbf{A}} = 0, \tag{1.15}$$

$$-\frac{\delta L_{tmp}}{\delta\psi} = 0. \tag{1.16}$$

Substituting (1.14) into (1.15) and (1.16) yields (1.2) and (1.1).

B. From Electromagnetism to Circuit Theory

Now, we consider an electric circuit contained in a volumetric region V. Then, integrating Lagrangian density L_d over V gives Lagrangian L of the whole circuit:

$$L = \int_{V} L_d dV \,. \tag{1.17}$$

Then, we step in simplification of the above expression of L and translate it into a circuit theory. In the whole process we introduce the following three approximations:

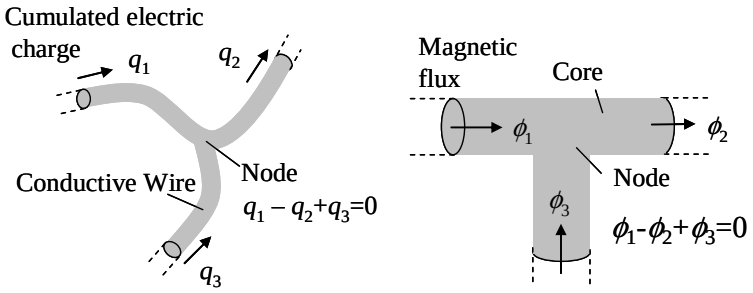

(a) A node of conductive wire (b) A node of magnetic path

Fig. 1.1. Electric and magnetic constraint at node of electric current and magnetic flux path

(1) There is no field (**E**=**0**, **B**=**0**) outside the circuit component. The same holds for conductive wire.

(2) There is neither charge nor current (ρ=0, **j**=**0**) outside the circuit component and conductive wire.

(3) There is no interference of electric and magnetic field between components. Specifically, **A** produced by a component is ignorable inside the others. Similarly, ψ produced by a component is also ignorable inside the others which are not electrically connected by a conductive wire.

The approximations (1) and (2) lead to $L_d \neq 0$ only inside the circuit components and conductive wire. Therefore, we can divide the circuit region V into regions of each circuit component V_i and the whole conductive wire V_w, and rewrite L in the form:

$$L = \sum_i \ell_i + \ell_w . \tag{1.18}$$

Where i is the index of the circuit components; ℓ_i and ℓ_w is Lagrangian of a circuit component and the whole conductive wire, respectively, defined as follows:

$$\ell_i = \int_{V_i} L_d dV \ , \quad \ell_w = \int_{V_w} L_d dV \ . \tag{1.19}$$

The conductive wire not only constitutes a part of the Lagrangian L, but also gives constraints among parameters that characterize L. Since $E = 0$ both inside the wire and at the boundary of the wire, (1.1) leads to $\rho = 0$ there. Accordingly, as shown in Fig. 1.1(a), the sum of the electric charge that flows into a node of the wire equals zero. If we define cumulated charge q as time integrated electric current that flows across a cross-section surface S from the initial time t_0 to the time t, i.e. by (1.20), the constraint on q at the node is expressed by (1.21).

$$q_k = \int_{t_0}^{t} \int_S \mathbf{j} \cdot d\mathbf{S} dt \ . \tag{1.20}$$

$$\sum_k d_k q_k = 0. \tag{1.21}$$

where $d\mathbf{S}$ is the area element of S, and d is an integer that takes 1 if the direction of $d\mathbf{S}$ is toward the node and −1 if it is opposite direction.

Likewise, the node of magnetic paths also gives a constraint. Consider the magnetic node shown in Fig. 1.1(b). If we define the magnetic flux ϕ by (1.22), we obtain the constraint expressed as in (1.23) because (1.3) leads to neither creation nor annihilation of the flux.

$$\phi_k = \int_S \mathbf{B} \cdot d\mathbf{S}. \tag{1.22}$$

$$\sum_k d_k \phi_k = 0. \tag{1.23}$$

Now, we suppose that the circuit Lagrangian L is the function of ϕ and q, as shown later. Then, the Lagrangian multiplier method can be employed to model the electric and magnetic circuit networks because (1.21) and (1.23) are holonomic constraints on ϕ and q. In the method, the modified Lagrangian L', written in the following equation, is substituted for the original Lagrangian L.

$$L' = \sum_i \ell_i + \ell_w + \sum_n \lambda_n f_n(q, \phi). \tag{1.24}$$

where n is the index of an electric node and a magnetic node, λ is the Lagrange multiplier, and $f(q,\phi)$ is the left-hand side of (1.21) or (1.23).

A power converter is ordinarily equipped with semiconductor switches or diodes. By means of the switches and diodes, the wire connection of the circuit is toggled from one to another periodically. Therefore, a general power converter has some electric nodes whose constraint conditions $f(q,\phi)$ are dependent on the conduction states of the switches.

Besides the semiconductor switches, an analysis of power converter commonly requires power dissipation by a load and parasitic resistance. However, our Lagrangian L' itself is insufficient for including lossy devices, since it is derived from electromagnetic field of lossless environment, i.e. the linear media. One of the simple methods to introduce lossy devices is to employ Rayleigh's dissipation function [41], [42] along with Lagrangian L'. Rayleigh's dissipation function D is defined by (1.25). Then, the movement of the system, namely the behavior of the circuit is known to be determined by Euler-Lagrange equation (1.26) [41], [42].

$$D = \frac{1}{2} \sum_s R_s \dot{q}_s^{\,2}. \tag{1.25}$$

$$\frac{d}{dt}\left(\frac{\partial L'}{\partial \dot{x}}\right) - \frac{\partial L'}{\partial x} = -\frac{\partial D}{\partial \dot{x}}. \tag{1.26}$$

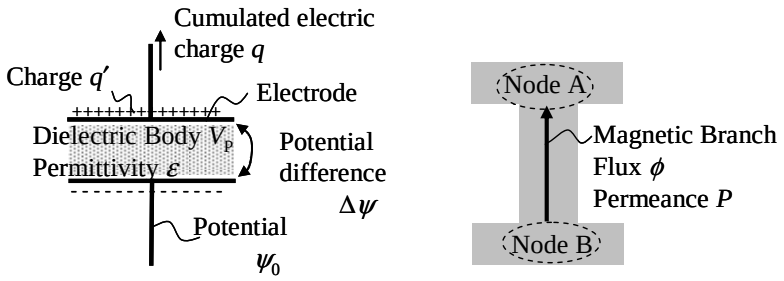

(a) Capacitor (b) Magnetic Branch

Fig. 1.2. Schematic illustrations of energy storage components used in power converter

where R_s is resistance of a resistor s, and x is any independent variable contained in either L' or D. As shown later, the variable x is any one of fluxes ϕ, cumulated electric charges q, or Lagrangian multipliers λ that are independent in the system.

Equations (1.24)–(1.26) are the basic structure of the circuit theory on Lagrangian dynamics. In order to perform an analysis of a real system, we should determine L'. The remaining question is in determining the component Lagrangian ℓ_i and the wire Lagrangian ℓ_w. In the next subsection, we discuss their practical expressions.

C. Component and Winding Lagrangian

A converter circuit with integrated magnetic components is generally composed of six kinds of components: namely, capacitors, voltage sources, magnetic cores (including coreless magnetic path), conductive wires (including windings), switches (including diode), and loads. As mentioned above, the switches and the loads are implemented in the constraint terms and the dissipation function D, respectively. Thus, the remaining four components have their own Lagrangian expression. Among them, the Lagrangian of a capacitor ℓ_C and that of voltage source ℓ_E have already been identified for LC circuits in preceding works [43]. They are defined as follows:

$$\ell_C = -q'^2/2C\,. \tag{1.27}$$

$$\ell_E = Eq\,. \tag{1.28}$$

where q' is the electric charge stored in the capacitor, C is the capacitance, E is the voltage, and q is the cumulated electric charge that flows out of the component. Note that q' is not identical to the cumulated charge q. The value q' is actually defined by (1.29), if we introduce the initial charge of the capacitor Q.

$$q' = Q - q\,. \tag{1.29}$$

Equations (1.27) and (1.28) can also be derived from (1.19). As for ℓ_C, consider a simple capacitor as shown in Fig. 1.2(a). We neglect the magnetic field **B** and vector

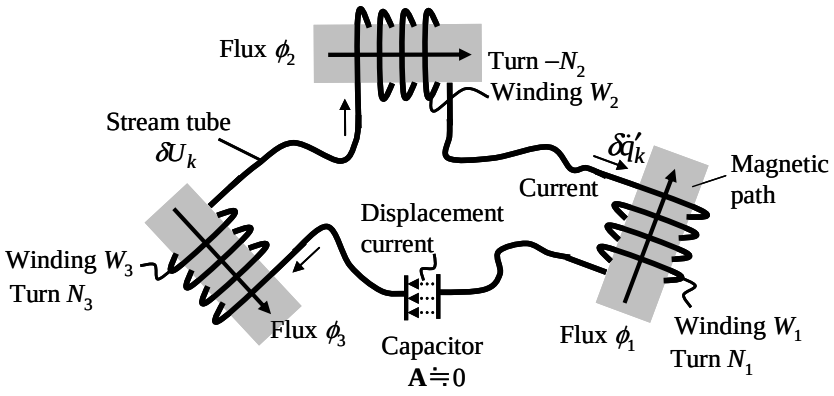

Fig. 1.3. Schematic illustration of a stream tube of electric current

potential **A** induced by the current in the electrode or displacement current in the dielectric body. Then, the Lagrangian density in the electrode is reduced to the first term of the right-hand side of (1.8). In addition, that of the dielectric body is reduced to the third term. Therefore, ℓ_C is obtained as follows:

$$\ell_C = \{-q'(\psi_0 + \Delta\psi) + q'\psi_0\} + \int_{V_P} \frac{\varepsilon}{2}\mathbf{E}^2 dV \,.$$

$$= -q'\Delta\psi + \frac{1}{2}C\Delta\psi^2 = -\frac{q'^2}{2C}. \tag{1.30}$$

The Lagrangian of voltage source is obtained by regarding C is infinitely great under condition that $Q/C = E$;

$$\ell_E = -\frac{q'^2}{2C} \approx -\frac{Q^2}{2C} + \frac{Q}{C}q = Eq. \tag{1.31}$$

The rightmost equality in (1.31) is derived using the fact that the Lagrangian is invariant under adding a constant.

Next, we step in determining the Lagrangian of a magnetic core ℓ_M. Here we define the magnetic core is a volumetric region where magnetic flux exists. Hence, a magnetic core includes air gaps and coreless magnetic paths, such as leakage flux paths.

We derive ℓ_M again using (1.19). We divide the component region V_i into magnetic branches, which are segments of magnetic paths divided by magnetic nodes, as shown in Fig. 1.2(b). Consequently, ℓ_M is obtained as (1.32) by summing the volumetric integrations of L_d over each branch.

$$\ell_M = -\sum_j \int_{V_j} \frac{\mathbf{B}^2}{2\mu} dV = -\sum_j \frac{\phi_j^{\,2}}{2P_j}. \tag{1.32}$$

where j is the index of the magnetic branches; V_j, ϕ_j, and P_j are the volumetric region, the flux and the permeance of a branch j, respectively.

Finally, we derive the Lagrangian of the whole conductive wire ℓ_W. Here the conductive wire includes not only the wire connecting the circuit components, but also the windings wound on magnetic paths. In the conductive wire we regard ρ=0, **E**=**0**, and **B** = **0**, referring to the above-mentioned approximations. Thus, the Lagrangian density L_d is reduced there to the second term of the right-hand side of (1.8). The Lagrangian ℓ_W is also obtained using (1.19). In order to straightforward calculation, we divide the component region V_i into stream tubes of electric current.

Electric current including displacement current constitutes stream tubes in a circuit because the divergence of this current's vector $\mathbf{j}'$ equals zero. The fact is derived by performing the divergence on (1.2):

$$\mathrm{div}\mathbf{j}' = \mathrm{div}\left(\mathbf{j} + \frac{\partial(\varepsilon\mathbf{E})}{\partial t} \right) = 0 . \tag{1.33}$$

Because the electric and displacement current is confined to the circuit, all the stream tubes compose circular paths inside the region V as illustrated in Fig. 1.3.

Now, we regard the whole paths of the electric and displacement current as a set of tiny stream tubes $\delta U'$. If we denote the region of the electric current in $\delta U'$ by δU, the whole conductive wire is a set of δU.

We denote the electric and displacement current inside a stream tube $\delta U'_k$ by $\delta j'_k$. Furthermore, we introduce a constant G_{kn} as the indicator of the relation between $\delta j'_k$ and ϕ_n, where ϕ_n is the flux that passes through the winding W_n (number of turns N_n). Specifically, G_{kn}=0, if $\delta U'_k$ does not constitute W_n; G_{kn}=1, else if the current flow of positive $\delta j'_k$ and the direction of positive ϕ_n satisfy the right hand grip rule; and otherwise G_{kn}=−1. We again neglect the vector potential **A** induced by the displacement current, similarly to the discussion of the capacitor Lagrangian. We also neglect **A** inside the component in which the displacement current takes place, according to the assumption (3).

Then, the volumetric integration of L_d over δU_k yields:

$$\int_{\delta U_k} \mathbf{A}\cdot\mathbf{j} dV = \int_{\delta U'_k} \mathbf{A}\cdot\mathbf{j}' dV = \delta j'_k \sum_n G_{kn} N_n \phi_n . \tag{1.34}$$

The left equality is satisfied because **j**=**j**′ in the conductive wire, where **E**=**0** according to the approximation (1), and **A**=**0** in the displacement current region.

By summing (1.34) over all stream tubes δU_k in the circuit, we finally obtain ℓ_W as follows:

$$\ell_W = \sum_k \int_{\delta U_k} \mathbf{A}\cdot\mathbf{j} dV = \sum_k \delta j'_k \left(\sum_n G_{kn} N_n \phi_n \right)$$

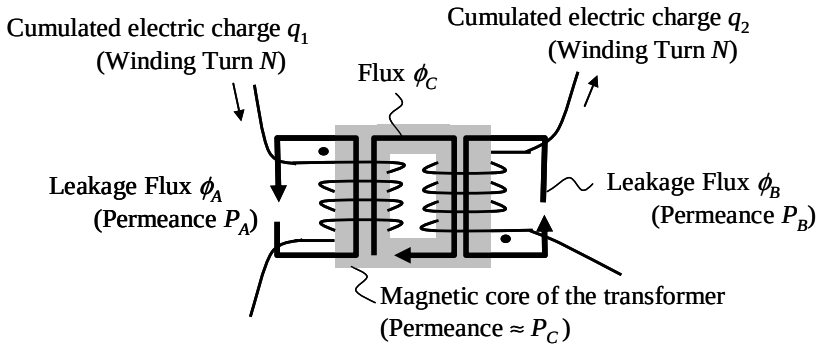

Fig. 1.4. A magnetic circuit of a basic transformer with leakage flux

$$= \sum_n N_n \phi_n \left(\sum_k G_{kn} \delta \mathbf{j}'_k \right) = \sum_n N_n \phi_n \dot{q}_n \,, \tag{1.35}$$

where q_n is cumulative charge that passes the winging W_n. The sign of q_n is defined so that the current flow of positive $\dot{q}_n$ and the direction of positive ϕ_n satisfy the right hand grip rule. When deriving the rightmost equality, we used that $\mathbf{j}=\mathbf{j}'$ in the winding.

D. Circuit Lagrangian

In the discussion made in the previous subsection, the Lagrangian of the circuit components and the conductive wire is all determined. Summarizing the result, i.e. (1.27), (1.28), (1.32) and (1.35), we obtain the following expression for Lagrangian L' of the whole circuit:

$$L' = \sum_i N_i \phi_i \dot{q}_i - \sum_j \frac{\phi_j^{\,2}}{2P_j} - \sum_k \frac{(Q_k - q_k)^2}{2C_k} + \sum_m E_m q_m + \sum_n \lambda_n f_n(q, \phi), \tag{1.36}$$

where i, j, k, m, n is the index of a winding, a magnetic branch, a capacitor, a voltage source and a node, respectively. Note that ϕ_i is total flux interlinking with the winding i, while ϕ_j is a total flux that passes the branch j.

Each term of Lagrangian L' corresponds to a circuit component or a node of electric or magnetic circuit network. Hence, we can configure L' of a circuit by directly translating physical structures of the electric and magnetic circuits.

The obtained Lagrangian is different from the conventional Lagrangian [31]–[36] in three points:

(1) Flux ϕ is introduced as an independent variable.

(2) Constraint terms for magnetic path are introduced

(3) Lagrangian expression that corresponds to magnetic components is divided into two terms: the windings and the core.

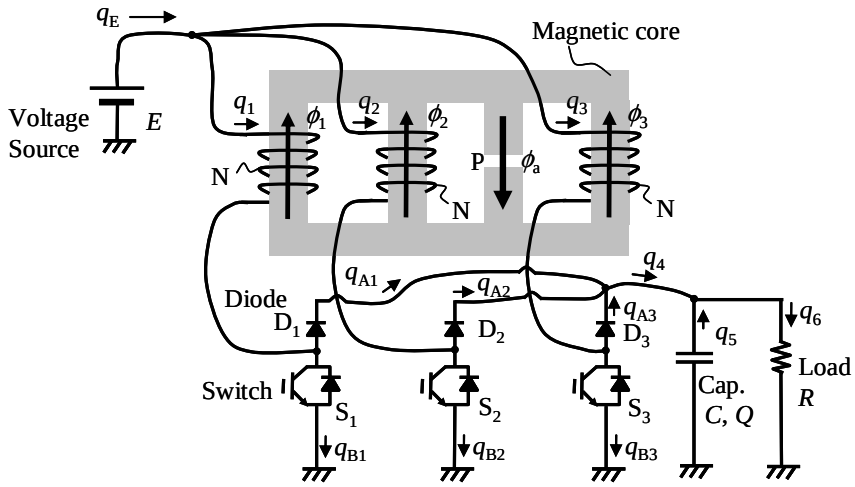

Fig. 1.5. Schematic diagram of the trans-linked three phase boost converter

These features are implemented as natural expansion of the conventional Lagrangian, which is proposed for converters based on LC circuit. In fact, our Lagrangian ℓ_1 for an inductor with a single magnetic path and a single winding (inductance Λ) is reduced to the same Lagrangian as the conventional theory;

$$\ell_1 = N\phi\dot{q} - \frac{\phi^2}{2P} = \frac{1}{2}PN^2\dot{q}^2 = \frac{1}{2}\Lambda\dot{q}^2 . \tag{1.37}$$

Our Lagrangian is configurable directly from the structure of magnetic circuit because the constituting elements, i.e. the windings and the core, are modeled individually. This feature allows systematic modeling of integrated magnetic core.

Leakage flux can be also implemented in our modeling, if the permeance of the leakage flux path is given. As an example, we derive Lagrangian of the basic transformer illustrated in Fig. 1.4. Translating each windings and each magnetic path into Lagrangian and summing the results, we obtain the following model ℓ_2:

$$\ell_2 = N(\phi_A + \phi_C)\dot{q}_1 + N(\phi_B + \phi_C)\dot{q}_2 - \frac{\phi_A^{\,2}}{2P_A} - \frac{\phi_B^{\,2}}{2P_B} - \frac{\phi_C^{\,2}}{2P_C} . \tag{1.38}$$

1.3. Example: analysis of trans-linked three phase boost converter

In this section, an example of the circuit analysis using the proposed Lagrangian is presented. The sample circuit is trans-linked three phase boost converter [13], which has an integrated magnetic component with three windings. The purpose of this example is to show the usefulness of Lagrangian dynamics in analyzing the circuit behavior. Here, we derive a state-space model of the trans-linked three phase boost converter

Figure 1.5 illustrates the schematic diagram of the trans-linked three phase boost converter. The magnetic core has four legs. Except one leg, each leg has its own winding of the same number of turns. We assume the leg with the winding, along with the top and bottom beams connecting the legs, is not gapped and has sufficiently high permeance compared to the leg without the winding. We denote the permeance of the leg without the winding by P.

One terminal of each winding is connected to the junction of a diode and a switch. Because the wire connection of this node is toggled by the switch, its electrical constraint is not static but dependent on the state of the switch. This type of the node is commonly utilized in a power converter. As for the junction of D1 and S1, its constraint term in the circuit Lagrangian L' is expressed as follows by introducing the indicator s_1 such that $s_1 = 1$, if the switch S1 is in on-state, and else $s_1 = 0$.

$$\lambda_{A1}\{(1-s_1)q_1 - q_{A1}\} + \lambda_{B1}(s_1 q_1 - q_{B1}), \tag{1.39}$$

where λ_{A1} and λ_{B1} are the Lagrangian multipliers.

Expression (1.39) corresponds to the constraint condition of $q_{A1}=0$ and $q_1=q_{B1,}$ if $s_1=1$; and $q_1=q_{A1}$ and $q_{B1}=0$, if $s_1=0$. Therefore, (1.39) successfully represents the function of the switch.

As a result, the circuit Lagrangian L' and the dissipation function D for the trans-linked three phase boost converter can be configured directly from Fig. 1.5:

$$\begin{aligned} L' = {} & N\sum_{i=1}^{3}\phi_i\dot{q}_i - \frac{\phi_a{}^2}{2P} - \frac{(Q-q_5)^2}{2C} + Eq_E + \sum_{i=1}^{3}\lambda_{Ai}\{(1-s_i)q_i - q_{Ai}\} + \sum_{i=1}^{3}\lambda_{Bi}\{s_i q_i - q_{Bi}\} \\ & + \lambda_0\left(\sum_{i=1}^{3}q_i - q_E\right) + \lambda_4\left(\sum_{i=1}^{3}q_{Ai} - q_4\right) + \lambda_5(q_4 + q_5 - q_6) \\ & + \lambda_6\left(\sum_{i=1}^{3}q_{Bi} - q_E - q_5 + q_6\right) + \lambda_a\left(\sum_{i=1}^{3}\phi_i - \phi_a\right), \end{aligned} \tag{1.40}$$

$$D = \frac{1}{2}R\dot{q}_6{}^2. \tag{1.41}$$

Equation (1.40) is reducible because it contains several ignorable variables [44]. An ignorable variable is a variable x whose time derivative constitute neither Lagrangian L' nor the dissipation function D. We can eliminate the variable from L' by substituting the formula $\partial L'/\partial x=0$ into the expression of L'. Hence, we can substitute $\lambda_{Ai}=\lambda_4=\lambda_5$ and $\lambda_{Bi}=0$ into (1.40) as a result of the formula $\partial L'/\partial x=0$ with respect to $x=q_4$, q_{Ai}, or q_{Bi}. Furthermore, we will eliminate q_E, q_{Ai}, and q_{Bi} using the ignorable variables λ_0, λ_{Ai}, and λ_{Bi}. Finally, we obtain the reduced expression of L' as follows:

$$L' = N\sum_{i=1}^{3}\phi_i\dot{q}_i - \frac{\phi_a{}^2}{2P} - \frac{(Q-q_5)^2}{2C} + E\sum_{i=1}^{3}q_i + \lambda_a\left(\sum_{i=1}^{3}\phi_i - \phi_a\right) + \lambda_5\left(\sum_{i=1}^{3}(1-s_i)q_i + q_5 - q_6\right). \tag{1.42}$$

When we develop (1.40), we omit the 10th right-hand term because the term reduces to the same constraint as the sixth right-hand term of (1.42).

Applying (1.42) to Euler-Lagrange equation (1.26) yields the circuit behavior:

$$N\dot{\phi}_i = E + (1 - s_i)\lambda_5 , \tag{1.43}$$

$$\sum_{i=1}^{3} (1 - s_i) q_i + q_5 - q_6 = 0 , \tag{1.44}$$

$$\phi_a = -P\lambda_a = \sum_{i=1}^{3} \phi_i , \tag{1.45}$$

$$\lambda_5 = -\frac{(Q - q_5)}{C} = -R\dot{q}_6 , \tag{1.46}$$

$$N\dot{q}_i = -\lambda_a . \tag{1.47}$$

Eliminating λ_a, λ_5, and q_6 from the above equations, and introducing the output voltage $V = (Q\text{-}q_5)/C$, we obtain the following system of equations.

$$\begin{cases} \dot{\phi}_i = \dfrac{E}{N} - (1 - s_i)\dfrac{V}{N}, \\ \dot{V} = -\dfrac{V}{CR} + \dfrac{\left\{\sum_{i=1}^{3} (1 - s_i)\right\}\left(\sum_{i=1}^{3} \phi_i\right)}{PCN}. \end{cases} \tag{1.48}$$

System (1.48) can be expressed by the state-space model, if we introduce the state variable $\mathbf{u} = (V\ \phi_1\ \phi_2\ \phi_3)^T$

$$\frac{d\mathbf{u}}{dt} = \begin{pmatrix} -1/CR & 3\bar{D}/PCN & 3\bar{D}/PCN & 3\bar{D}/PCN \\ -\bar{D}_1/N & 0 & 0 & 0 \\ -\bar{D}_2/N & 0 & 0 & 0 \\ -\bar{D}_3/N & 0 & 0 & 0 \end{pmatrix} \mathbf{u} + \begin{pmatrix} 0 \\ E/N \\ E/N \\ E/N \end{pmatrix}, \tag{1.49}$$

where $\bar{D}_i = 1 - s_i$ and $\bar{D} = (\bar{D}_1 + \bar{D}_2 + \bar{D}_3)/3$. In the state-space averaging method, we take time average on $\bar{D}_i$ and $\bar{D}$. Thus, $\bar{D}_i$ and $\bar{D}$ are now real numbers that satisfy $0 \le \bar{D}_i \le 1$ and $0 \le \bar{D} \le 1$. The value $1 - \bar{D}_i$ is interpreted as duty of the switch S_i; and the value $1 - \bar{D}$ is interpreted as the averaged duty of the switches S1, S2 and S3.

As we have seen above, the whole system of the converter is expressed by the movement of the output voltage, namely q_5, and the fluxes. Our Lagrangian L' regards the cumulated electric charge q and the flux ϕ as the independent variables. Because the electric current is dependent variables, observing all of the current is not necessarily sufficient to determine all of the independent flux. Indeed, the current of this example is expressed only by the sum of the flux, as shown in (1.50).

$$\dot{q}_1 = \dot{q}_2 = \dot{q}_3 = -\sum_{i=3}^{3} \frac{\phi_i}{PN} . \tag{1.50}$$

Therefore, observation of the voltage and the current is unable to determine the state of the system. The perfect observation of the system requires the additional observation of any two fluxes of ϕ_1, ϕ_2, and ϕ_3.

To summarize, as this example shows, Lagrangian L' of a converter is directly configurable from the physical structures of the electric and magnetic circuits; and the circuit behavior is systematically obtained by applying L' and D to Euler-Lagrange equation.

1.4. Conclusions

The integrated magnetic component is expected to improve power conversion efficiency and downsize the total volume of magnetic components. Although a number of preceding works reported its usefulness, its practical applications are still limited. One probable reason may lie in difficulty of analytic understanding of complicated magnetic circuit.

In order to address the problem, we presented a novel circuit theory that directly handles integration of electric and magnetic circuits. As shown in the analysis example, the Lagrangian model is configurable directly from the physical structure of the electric and magnetic circuit. Furthermore, the state-space model is systematically obtained by predetermined procedure. This result demonstrates that this theory can be a promising tool for applying integrated magnetic components to practical uses.

REFERENCES

[1] S. V. Marshall, and G. G. Skitek, "Magnetic circuits," in *Electromagnetic concepts and applications*, 3rd ed., New Jersey: Prentice Hall, 1990, pp. 276-283.

[2] D. K.-W. Cheng, Leung-Pong Wong, and Y.-S. Lee, "Design, modeling, and analysis of integrated magnetics for power converters," in *Proc. Power Electronics Specialists Conf.*, 2000, vol. 1, pp. 320-325.

[3] P. Zumel, O. Garcia, J. A. Cobos, and J. Uceda, "Magnetic integration for interleaved converters," in *Proc. Appl. Power Electron. Conf. and Expo.*, 2003, vol. 2, pp. 1143-1149.

[4] S. Chandrasekaran and L. U. Gokdere, "Integrated magnetics for interleaved DC-DC boost converter for fuel cell powered vehicles," in *Proc. Power Electronics Specialists Conf.*, 2004, pp. 356-361.

[5] Wei Wen, and Y.-S. Lee, "A two-channel interleaved boost converter with reduced core loss and copper loss," in *Proc. Power Electronics Specialists Conf.*, 2004, pp. 1003-1009.

[6] Leung-Pong Wong, Y. S. Lee, D. K. W. Cheng, and M. H. L. Chow, "Two-phase forward converter using an integrated magnetic component," *IEEE Trans. Aerosp. Electron. Syst.*, vol. 40, no. 4, pp. 1294-1310, Oct. 2004.

[7] L. Yan, and B. Lehman, "An integrated magnetic isolated two-inductor boost converter: analysis, design and experimentation," *IEEE Trans. Power Electron.*, vol. 20, no. 2, pp. 332-342, Mar. 2005.

[8] E. Laboure, A. Cuniere, T. A. Meynard, F. Forest, and E. Sarraute, "A theoretical approach to intercell transformers, application to interleaved converters," *IEEE Trans. Power Electron.*, vol. 23, no. 1, pp. 464-474, Jan. 2008

[9] L. P. Wong, Y. S. Lee, M. H. L. Chow, and D. K. W. Cheng, "A four-phase forward converter using an integrated transformer," *IEEE Trans. Ind. Electron.*, vol. 55, no. 2, pp.817-831, Feb. 2008.

[10] J. Sun and V. Mehrotra, "Orthogonal winding structures and design for planar integrated magnetics," *IEEE Trans. Ind. Electron.*, vol. 55, no. 3, pp. 1463-1469, Mar. 2008.

[11] T. Kawashima, S. Funabiki, and M. Yamamoto, "Recovery-less boost converter for electric vehicle," in *Proc. European Conf. Power Electron. and Applicat.*, 2009, pp. 1-10.

[12] J. Salmon, J. Ewanchuk, and A. M. Knight, "PWM inverters using split-wound coupled inductors," *IEEE Trans. Ind. Appl.*, vol. 45, no. 6, pp. 2001-2008, Nov./Dec. 2009.

[13] M. Nakahama, M. Yamamoto, and Y. Satake, "Trans-linked multi-phase boost converter for electric vehicle," in *Proc. Energy Conversion Congr. and Expo.*, 2010, Atlanta, pp. 2458-2463.

[14] H. N. Nagaraja, D. Kastha, and A. Patra, “Design principles of a symmetrically coupled inductor structure for multiphase synchronous buck converters,” *IEEE Trans. Ind. Electron.*, vol. 58, no. 3, pp. 988-997, Mar. 2011.

[15] S. Roy and L. Umanand, “Integrated magnetics-based multisource quality AC power supply,” *IEEE Trans. Ind. Electron.*, vol. 58, no. 4, pp. 1350-1358, April 2011.

[16] F. Yang, X. Ruan, Y. Yang, and Z. Ye, “Interleaved critical current mode boost PFC converter with coupled inductor,” *IEEE Trans. Power Electron.*, vol. 26, no. 9, pp. 2404-2413, Sept. 2011.

[17] Z. Ouyang, Z. Zhang, O. C. Thomson, and M. A. E. Andersen, “Planar-integrated magnetics (PIM) module in hybrid bidirectional DC-DC converter for fuel cell application,” *IEEE Trans. Power Electron.*, vol. 26, no. 11, pp. 3254-3264, Nov. 2011.

[18] S. Utz and J. Pforr, “Operation of multi-phase with coupled inductors at reduced numbers of phases,” in *Proc. 14th European Conf. Power Electron. Applicat.* (EPE), 2011, pp. 1-10.

[19] N. Zhu, J. Kang, D. Xu, B. Wu, and Y. Xiao, “An integrated AC choke design for common-mode current suppression in neural-connected power converter systems,” *IEEE Trans. Power Electron.*, vol. 27, no. 3, pp. 1228-1236, Mar. 2012.

[20] W. Li, P. Li, H. Yang, and X. He, “Three-level forward-flyback phase-shift ZVS converter with integrated series-connected coupled inductors,” *IEEE Trans. Power Electron.*, vol. 27, no. 6, pp. 2846-2856, Jun. 2012.

[21] D. O. Boillat and J. W. Kolar, “Modeling and experimental analysis of a coupled inductor employed in a high performance AC power source,” in *Proc. Intl. Conf. Renewable Energy Research Applicat.* (ICRERA), 2012, pp. 1-18.

[22] J. Imaoka, M. Yamamoto, K. Umetani, S. Arimura, and T. Hirano, “Characteristics analysis and performance evaluation for interleaved boost converter with integrated winding coupled inductor,” in *Proc. Energy Conversion Congr. Expo.*, 2013, pp. 3711-3718.

[23] K. J. Hartnett, J. G. Hayes, M. G. Egan, and M. S. Rylko, “CCTT-core split-winding integrated magnetic for high-power DC-DC converters,” *IEEE Trans. Power Electron.*, vol. 28, no. 11, pp. 4970-4984, Nov. 2013.

[24] C. Deng, D. Xu, P. Chen, C. Hu, W. Zhang, Z. Wen, and X. Wu, “Integration of both EMI filter and boost inductor for 1kW PFC converter,” *IEEE Trans. Power Electron.*, vol. PP, issue 99, pp. 1, 2014

[25] K. Umetani, F. Iwamoto, and K. Yagyu , “A unidirectional boost chopper with snubber energy regeneration using a coupled inductor,” *IEEJ Trans. Elect. Electron. Eng.*, vol 9, no. 3, pp. 315-323, May 2014.

[26] K. Umetani, T. Tera, K. Shirakawa, “Novel magnetic structure of integrated differential-mode and common-mode inductors to suppress DC saturation,” *IEEJ Trans. Ind. Appl.* (in press)

[27] H. D. Nijiende, N. Fröhleke, and J. Böcker, “Derivation of integrated magnetic components using reluctance and mathematical modeling,” in *Proc. Power Electron. Specialists Conf.* (PESC), 2014, pp. 4855-4860.

[28] A. A. Aboulnaga and A. Emadi, “Simplified simulation and modeling technique for integrated magnetic components in power electronic converters,” in *Proc. Telecommunications Energy Conf.* (INTELEC), 2004, pp. 725-730.

[29] J. D. Kraus, “Time changing electric and magnetic field,” in *Electromagnetics*, 4th ed., New York: McGraw-Hill, 1991, pp. 432-435.

[30] B. D. H. Tellegen, “The gyrator, a new electric network element,” *Phillips Res. Rept.*, vol. 3, pp. 81-101, 1948.

[31] H. Sira-Ramírez, R. Ortega, and G. Escobar, “Lagrangian modeling of switch regulated DC-to-DC power converters,” in Proc. 35th Conf. Decision Control, 1996, vol. 4, pp. 4492-4496.

[32] H. Sira-Ramírez and M. D. de Nieto, “A Lagrangian approach to average modeling of pulsewidth-modulation controlled DC-to-DC power converters,” *IEEE Trans. Circuits Syst. I*, vol. 43, no. 5, pp. 427-430, May 1996.

[33] J. M. A. Scherpen, D. Jeltsema, and J. B. Klaassens, “Lagrangian modeling and control of switching networks with integrated coupled magnetics,” in *Proc. 39th Conf. Decision Control*, 2000, vol. 4, pp. 4054-4059.

[34] J. M. A. Scherpen, D. Jeltsema, and J. B. Klaasens, “Lagrangian modeling of switching electrical networks,” *Syst. Control Lett.*, vol. 48, pp. 365-374, April 2003.

[35] J. Clemente-Gallardo and J. M. A. Scherpen, “Relating Lagrangian and Hamiltonian formalisms of LC circuits,” *IEEE Trans. Circuits Syst. I*, vol. 50, no. 10, pp. 1359-1363. Oct. 2003.

[36] T. S. Lee, “Lagrangian modeling and passivity-based control of three-phase AC/DC voltage-source converters,” *IEEE Trans. Ind. Electron.*, vol. 51, no. 4, pp. 892-902, Aug. 2004.

[37] K. Umetani, “Improvement of saturation property of iron powder core by flux homogenizing structure,” *IEEJ Trans. Elect. Electron. Eng.*, vol. 8, issue 6, pp. 640-648, Nov. 2013.

[38] J. D. Kraus, *Electromagnetics*. 4th ed., New York: McGraw-Hill, 1991, pp.460-474.

[39] K. Kawamura, *Electromagnetism*. Tokyo, Japan: Iwanami, 1994, pp.218-223. (in Japanese)

[40] C. B. Zheng and Z. J. Wang, “A new Lagrangian density for all four maxwell’s equations”, *Intl. J. Eng. Sci.*, vol. 48, issue 12, pp.2110-2112, Dec. 2010.

[41] L. D. Landau and E. M. Lifshitz, “Damped oscillations” in *Mechanics*, Oxford, U. K.: Butterworth- Heinemann, 1976, pp.74-77.

[42] H. Goldstein, C. P. Poole, Jr., J. L. Safko, “Velocity dependent potential and the dissipation function,” in *Classical Mechanics*, 3rd ed., New Jersey: Pearson Education International, 2002, pp. 22-24.

[43] D. A. Wells, “Applications of Lagrange’s equations to electrical and electromechanical systems,” in *Schaum’s Outline of Theory and Problems of Lagrangian Dynamics*, New York: McGraw-Hill, 1976, pp.302-315.

[44] C. Lanczos, “Kinosthenic or ignorable variables and their elimination,” in *The Variational Principles of Mechanics*, 4th ed., New York: Dover, 1970, pp.125-130.

Chapter 2

LAGRANGIAN METHOD FOR DERIVING EQUIALENT CIRCUITS OF INTEGRATED MAGNETIC COMPONENTS

2. 1. Introduction

This chapter proposes Lagrangian method for deriving equivalent circuit of integrated magnetic components. Integrated magnetic components are promising techniques to miniaturize magnetic components such as transformers and inductors. In a well-designed component, the core can be miniaturized as reported in [1], [2], [3] and the total amount of copper can be reduced as reported in [4]. Owing to these benefits, a number of magnetic structures for integrated magnetic components have been studied and reported [1]–[25].

However, the integrated magnetic components often have complex magnetic circuits, particularly if leakage flux paths are considered. As a result, their electric functions can be difficult to comprehend, compared to a basic inductor or transformer with a single magnetic path. In a direct analysis of the power converters with integrated magnetic components [1], [2], [4], [5], [7], [14], [17], [19], [20], both the electric and magnetic circuits are handled simultaneously. Accordingly, such analysis tends to be complex compared to that only of electric circuits.

This approach calculates all the flux in the magnetic circuit, and thus it is useful for precise design of the magnetic core dimension. Conversely, the complex analysis procedure may hinder intuitive comprehension of the overall circuit behavior. Consequently, the industrial applications of the integrated magnetic components may be promoted by developing methods that can easily analyze circuit behaviors.

One promising strategy is to express the electric functions of an integrated magnetic component as a functionally equivalent electric circuit composed of inductors and transformers [3], [6], [11], [13], [20], [21], [23]. Hereafter, we refer to this circuit as the equivalent circuit.

To the best of the author's knowledge, three methods are available to derive equivalent circuits. These methods generally derive equivalent circuits that differ from others. Selecting a simpler equivalent circuit may therefore contribute to effortless circuit analysis

The inductance matrix method [13] is one such method. This first identifies the leakage inductance of all windings, and the mutual inductance [26] of all winding pairs. Each leakage inductance is then directly transformed into an inductor, and each of the mutual inductances into a transformer. Hence, the integrated magnetic component with n windings is generally expressed by an equivalent circuit with n inductors and $n(n-1)/2$ transformers.

The duality method has also been used [27] [28]. An advantage of this method is its straightforward derivation process. The method first transforms the network of the magnetic circuit model [29] of an integrated magnetic component. Specifically, the series-connections of the original network are transformed into parallel connections, and vice versa. Each reluctance is then replaced by an inductor, and all except one of the magnetomotive forces are replaced by an ideal transformer. The remaining magnetomotive force is eliminated. Consequently, if the integrated magnetic components contain n windings and m reluctance, the resultant equivalent circuit derived from the duality method will have $n-1$ transformers and m inductors.

Besides the above-mentioned methods, we can utilize Lagrangian dynamics to derive equivalent circuits as discussed in this chapter. Hereafter, we refer to this method as the Lagrangian method. This method transforms an integrated magnetic component into an equivalent circuit composed of as many basic transformers and inductors as the flux paths of the original component that can be magnetized independently. This method can thus be expected to yield a simple equivalent circuit, if the integrated magnetic component has a small number of independent flux paths.

The purposes of this chapter are 1) to derive and formulate the method, and 2) to verify the method using a case study. As for the former purpose, Section 2.2 first presents an example of the Lagrangian method; then, it formulates the method. The Lagrangian method provides two techniques to derive equivalent circuits. Section 2.2 discusses the two techniques in Subsection 2.1.A and Subsection 2.2.B, respectively.

As for the latter purpose, Sections 2.3–2.5 presents a case study using the integrated winding coupled inductor [4], [6], [21]. This integrated winding coupled inductor has three windings. Its magnetic circuit model, as shown in this chapter, has six reluctance, three magnetomotive forces, and five independent flux paths, including leakage flux paths. Consequently, among the three methods, the Lagrangian method is expected to yield the equivalent circuit with fewest magnetic components.

Section 2.3 compares the equivalent circuits using the three methods to show that the Lagrangian method yields an equivalent circuit differing from those by the conventional methods, i.e. the inductance matrix method and the duality method. This section also shows that the equivalent circuit from the Lagrangian method has fewest components, as expected. Section 2.4 then shows theoretically that the equivalent circuit by the Lagrangian method is consistent with the magnetic circuit model, as are those by the conventional methods. Section 2.5 experimentally confirms that the equivalent circuits discussed in Section 2.4 are also consistent with experimental behavior of the integrated winding coupled inductor. Finally, Section 2.6 presents the conclusions.

2. 2. Lagrangian Method

This section presents the Lagrangian method to translate the integrated magnetic component into an equivalent circuit.

Generally, two systems show the same behavior, if their Lagrangian lead to the same result when applied to Euler-Lagrange equation. We denote that these Lagrangian are equivalent each other. Therefore, if an equivalent Lagrangian for an integrated magnetic component belongs to an electric circuit of basic transformers and inductors, the circuit

shows the same electric functions as the component. As a result, the circuit is the equivalent circuit. To summarize, the Lagrangian method is based on finding an equivalent Lagrangian that belongs to an electric circuit.

The Lagrangian method gives two different techniques, each of which leads to a different equivalent circuit. Each of them are discussed separately in Subsections 2.1 and 2.2, respectively. These subsections first present an example using the integrated magnetic component employed in the trans-linked converter. The diagram of this component is shown in Fig. 1.5 in Chapter 1. Then, the subsections give generalized formulation of the method applicable to an arbitrary integrated magnetics. The variables used in the equations in this section are the same as that used in Section 1.3

A. Technique 1

We presents derivation of the equivalent circuit of the integrated magnetic component shown in Fig. 1.5 according to the technique 1. We begin our discussion from determining the Lagrangian of the integrated magnetic component. Extracting the magnetism related terms in the equation (1.42), we obtain the Lagrangian ℓ_L of the integrated magnetic component.

$$\ell_L = N\sum_{i=1}^{3}\phi_i\dot{q}_i - \frac{\phi_a^{\,2}}{2P} + \lambda_a\left(\sum_{i=1}^{3}\phi_i - \phi_a\right). \tag{2.1}$$

Because the Lagrangian multiplier λ_a is inherent characteristic of the integrated magnetic circuit, we have to eliminate it to translate the Lagrangian into the circuit of magnetic components composed of single magnetic paths. One technique is to utilize the fact that the Lagrangian multiplier is an ignorable variable [30]. The ignorable variable can be eliminated by substituting $\partial L'/\partial\lambda_a=0$ into (2.1). Eliminating q_1 by substitution yields the following equivalent Lagrangian:

$$\ell_L = N\dot{q}_1\phi_a + N(\dot{q}_2 - \dot{q}_1)\phi_2 + N(\dot{q}_3 - \dot{q}_1)\phi_3 - \frac{\phi_a^{\,2}}{2P}. \tag{2.2}$$

The Lagrangian expressed by (2.2) corresponds to the circuit illustrated in Fig. 2.1. Consequently, it is the equivalent circuit.

Generally, the Lagrangian of a magnetic core ℓ_M has a quadratic form of the flux ϕ; and the magnetic constraint terms have linear forms of ϕ. Therefore, a Lagrangian of a magnetic component (regardless to integrated or discrete) ℓ_L can be expressed in the following form (2.3) by eliminating all the magnetic constraint terms according to the method to eliminate ignorable variables. We denote the number of independent cumulative electric charge and fluxes by n and k, respectively.

$$\ell_L = \dot{\mathbf{q}}^T\mathbf{N}\boldsymbol{\varphi} - \boldsymbol{\varphi}^T\mathbf{A}\boldsymbol{\varphi}\ , \tag{2.3}$$

where $\mathbf{A}$ is a $k\times k$ symmetrical matrix, $\mathbf{N}$ is a $n\times k$ matrix, $\dot{\mathbf{q}}$ is a n-dimensional vector of the independent current, $\boldsymbol{\varphi}$ is a k-dimensional vector of the independent fluxes.

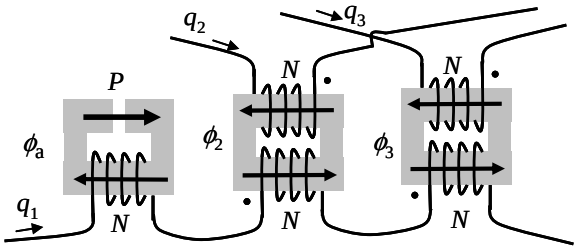

Fig. 2.1. Equivalent circuit derived by Technique 1. The original integrated magnetic component is that employed in the trans-linked three phase boost converter.

A symmetrical matrix can be transformed into a diagonal matrix using an appropriate orthogonal matrix. Therefore, we transform the symmetrical matrix **A** into a diagonal matrix **B** by an orthogonal matrix **P**. If we introduce the vector $\boldsymbol{\varphi}' = \mathbf{P}\boldsymbol{\varphi}$, (2.3) is transformed into another form:

$$\ell_L = \dot{\mathbf{q}}^T \mathbf{N}\mathbf{P}^{-1}\boldsymbol{\varphi}' - \boldsymbol{\varphi}'^T \mathbf{B}\boldsymbol{\varphi}'. \tag{2.4}$$

The Lagrangian expressed by (2.4) corresponds to a circuit that consists of k independent single magnetic paths and n independent current paths. The integer $p = k -$ rank(**B**) indicates the number of ideal transformers, because p fluxes vanish in the second right-hand term (2.4).

The matrix $\mathbf{NP}^{-1}$ indicates the number of turns of the windings in the equivalent circuit. The (a,b)-th entry of the matrix denotes the number of turns of the winding in a-th current path wound on the b-th flux path.

B. Technique 2

In Technique 2, the Lagrangian multiplier λ_a in (2.1) is eliminated using a cyclic coordinate. Consider the modified Lagrangian ℓ'_L defined as (2.5). This Lagrangian is obtained by substituting the product of the number of turns and current of a virtual winding for the multiplier λ_a.

$$\ell'_L = N\sum_{i=1}^{3}\phi_i\dot{q}_i - \frac{\phi_a^{\,2}}{2P} + N_a\dot{q}_a\left(\sum_{i=1}^{3}\phi_i - \phi_a\right), \tag{2.5}$$

where N_a is the number of turns of the virtual winding and q_a is its cumulative electric charge. We take the variable q_a independent of any other variables in Lagrangian or the dissipation function of a circuit containing ℓ'_L. Then, q_a is a cyclic coordinate because only its time derivative is contained in L'.

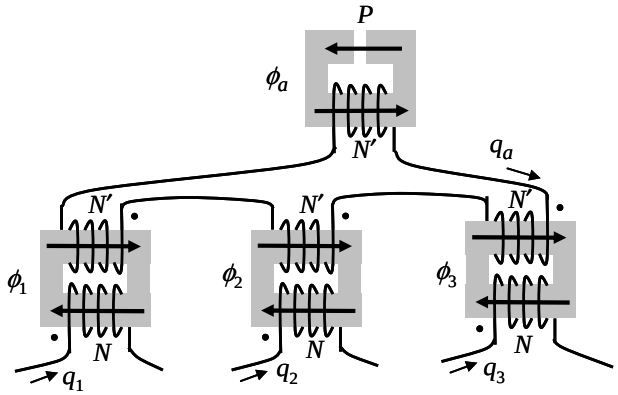

Fig. 2.2. Equivalent circuit derived by Technique 2. The original integrated magnetic component is that employed in the trans-linked three phase boost converter.

A Lagrangian with a cyclic coordinate is known to be reduced by the following method [30]. If we substitute ℓ'_L for L' and q_a for x in Euler-Lagrange equation (1.26) and perform time integration, we obtain:

$$\frac{\partial \ell'_L}{\partial \dot{q}_a} = C \,, \tag{2.6}$$

where C is a integration constant.

Then, we introduce another Lagrangian ℓ''_L defined as

$$\ell''_L = \ell'_L - C\dot{q}_a \,. \tag{2.7}$$

We substitute (2.6) into (2.7). The resultant Lagrangian ℓ''_L is known to be equivalent to the original Lagrangian ℓ'_L. Eliminating ϕ_1 by this substitution yields:

$$\ell''_L = N\dot{q}_1(\phi_a - \phi_2 - \phi_3 + C) + N\dot{q}_2\phi_2 + N\dot{q}_3\phi_3 - \frac{\phi_a^{\,2}}{2P} \,. \tag{2.8}$$

If we assume $C=0$, the right hand side of (2.8) equals to that of the equation (2.2). Thus, ℓ''_L is an equivalent Lagrangian of ℓ_L under condition of $C = 0$; and the same holds true for ℓ'_L. Fig. 2.2 illustrates the circuit that corresponds to the Lagrangian ℓ'_L. The circuit functions as an equivalent circuit for the integrated magnetic component, when the initial values are set so that $C=0$. Specifically, the initial values ϕ_{a0}, ϕ_{10}, ϕ_{20}, ϕ_{30} for the flux ϕ_a, ϕ_1, ϕ_2, ϕ_3 are required to satisfy the following relation.

$$\sum_{i=1}^{3} \phi_{i0} - \phi_{a0} = 0 \,. \tag{2.9}$$

In this derivation method, a Lagrangian multiplier for the magnetic constraint is replaced by the magnetomotive force by an additionally introduced virtual current path.

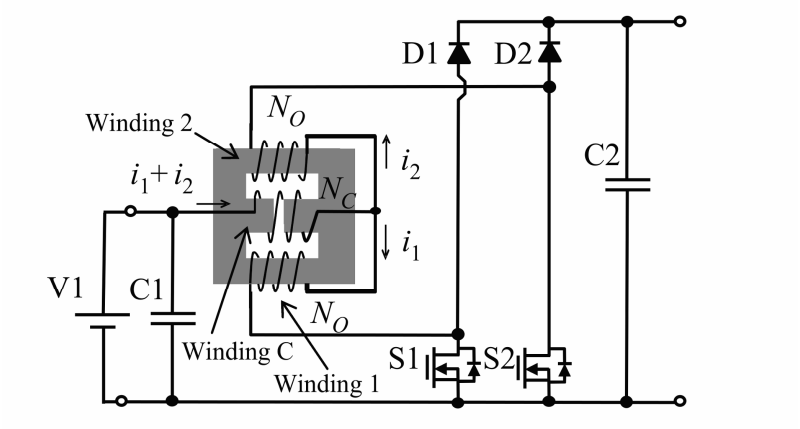

Fig. 2.3. Interleaved converter with the integrated winding coupled inductor.

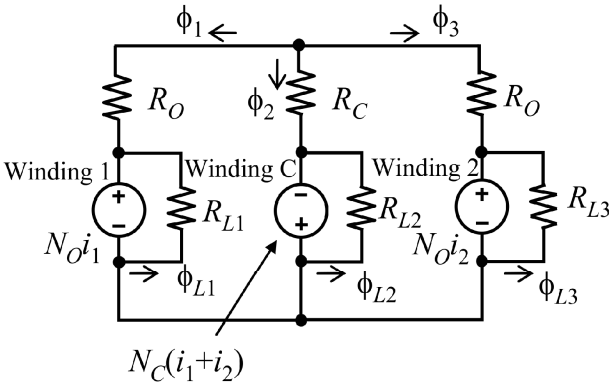

Fig. 2.4. Magnetic circuit model of the integrated winding coupled inductor.

When applying the method to an integrated magnetic component, we introduce additional independent current paths, as much as the constraints, in the equivalent circuit. These additional current paths yield the additional independent variables q in the system. Nevertheless, the derived equivalent system preserves the original degree of freedom because additional constraint conditions, as many as added variables, are introduced on the initial values.

Fig. 2.2 is the same equivalent circuit presented in [13].

2. 3. Comparison of Equivalent Circuits by Different Methods

The interleaved converter with the integrated winding coupled inductor [4] [21] is illustrated in Fig. 2.3. The magnetic core has three legs, each of which has a winding. Input current flows into winding C, and the current is then split into windings 1 and 2.

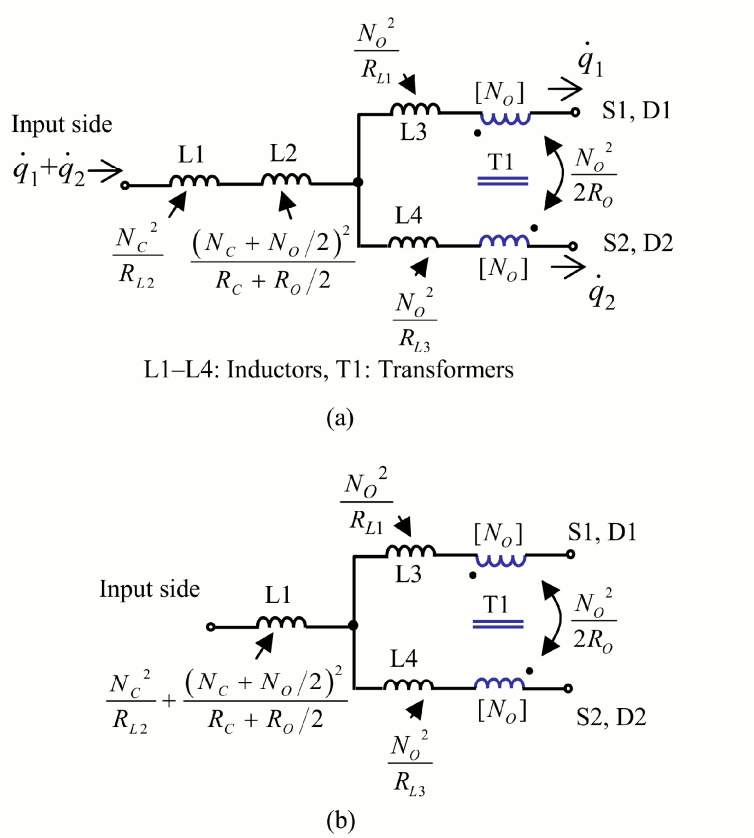

Fig. 2.5. Equivalent circuit by the Lagrangian method. (a) Direct translation from Lagrangian. (b) Simplified circuit with fewer inductors. Values in brackets are the number of turns. Values without brackets are the self-inductance for the inductors or the mutual inductance for the transformers.

In this chapter, we ignore non-linearity due to magnetic saturation or core loss. Similar to the conventional methods, the Lagrangian method also does not allow non-linearity so far because it assumes linear media of the electromagnetic field.

The magnetic circuit model [29] of the integrated magnetic component can be expressed as in Fig. 2.4. We denote the electric current of windings 1 and 2 as i_1 and i_2, respectively. The outer legs and the center leg have windings with the number of turns N_O and N_C, and the reluctances R_O and R_C, each of which are made by core and gaps. We assume that both outer legs have the same reluctance R_O and the number of turns N_O, according to the design concept of the magnetic structure. Leakage flux paths of the windings are implemented as the reluctance R_{L1}–R_{L3}.

A. Lagrangian Method

Based on Fig. 2, we derive an equivalent circuit according to the Lagrangian method presented in Subsection 2.2.A. The method is based on Lagrangian expressions for an

integrated magnetic component, which are directly configurable from their electric and magnetic network. We first translated Fig. 2.4 into Lagrangian. We then applied point transformation [31] to the result. Based on this, we obtained another Lagrangian belonging to an equivalent circuit. Finally, the equivalent circuit was obtained by translating the resultant Lagrangian into a physical circuit.

As discussed in Chapter 1, the current flowing through a winding is regarded as the time derivative of the cumulative charge q in the Lagrangian expression, which is the time integration of the current i from the initial time t_0 to the time t:

$$q_k = \int_{t_0}^{t} i dt \ . \tag{2.10}$$

We denote the cumulative charge for i_1 and i_2 as q_1 and q_2, respectively. Translation of Fig. 2.4 yields the Lagrangian L:

$$\begin{aligned} L = &-N_O \dot{q}_1 (\phi_1 + \phi_{L1}) + N_C (\dot{q}_1 + \dot{q}_2)(\phi_2 + \phi_{L2}) - N_O \dot{q}_2 (\phi_3 + \phi_{L3}) - \frac{1}{2} R_{L1} {\phi_{L1}}^2 \\ &- \frac{1}{2} R_{L2} {\phi_{L2}}^2 - \frac{1}{2} R_{L3} {\phi_{L3}}^2 - \frac{1}{2} R_O {\phi_1}^2 - \frac{1}{2} R_C {\phi_2}^2 - \frac{1}{2} R_O {\phi_3}^2 + \lambda (\phi_1 + \phi_2 + \phi_3), \end{aligned} \tag{2.11}$$

where λ is a Lagrangian multiplier, and the dot over a variable is its time derivative.

The term with λ is eliminated by substituting $\phi_3 = -\phi_1 - \phi_2$ into (2.11). Additionally, we replace ϕ_1 by introducing $\phi_A = \phi_1 + \phi_2/2$. The purpose of introducing ϕ_A is to express the magnetic energy terms, i.e. the 4th–9th right-hand terms of (2.11), in the diagonal form of the fluxes without using the Lagrangian multiplier. Consequently, we obtain:

$$\begin{aligned} L = &(N_O \dot{q}_2 - N_O \dot{q}_1)\phi_A - R_O {\phi_A}^2 + \left(N_C + \frac{N_O}{2} \right)(\dot{q}_1 + \dot{q}_2)\phi_2 - \left(\frac{R_C}{2} + \frac{R_O}{4} \right){\phi_2}^2 \\ &- N_O \dot{q}_1 \phi_{L1} - \frac{1}{2} R_{L1} {\phi_{L1}}^2 - N_O \dot{q}_2 \phi_{L3} - \frac{1}{2} R_{L3} {\phi_{L3}}^2 + N_C (\dot{q}_1 + \dot{q}_2)\phi_{L2} - \frac{1}{2} R_{L2} {\phi_{L2}}^2, \end{aligned} \tag{2.12}$$

Equation (2.12) corresponds to a circuit of transformers and inductors. Translating (2.12) yields the equivalent circuit shown in Fig. 2.5(a). Along with the circuit diagram, we also present the self and mutual inductance of the constituting elements.

The Lagrangian method preserves the number of independent fluxes. Note that ϕ_3 is dependent on ϕ_1 and ϕ_2 because the constraint $\phi_1 + \phi_2 + \phi_3 = 0$ is represented by the last right-hand term of (2.11). Hence, (2.11) contains five independent fluxes, namely ϕ_{L1}, ϕ_{L2}, ϕ_{L3}, ϕ_1, ϕ_2. Consequently, the resultant equivalent circuit is composed of five magnetic components, each of which consists of a single independent flux path.

Fortunately, in this case the equivalent circuit can be simplified further, because inductors L1 and L2 are connected in series. By replacing them by an inductor whose inductance is their sum, we obtain Fig. 2.5(b), which is composed of only four magnetic components. The result is similar to the equivalent circuit proposed in [4]. Nonetheless, our result is derived automatically under the predetermined procedure.

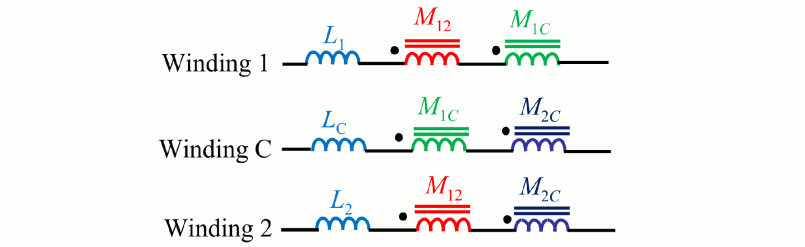

Fig. 2.6. Replacing each winding of the integrated winding coupled inductor by an inductor representing the leakage inductance and transformers representing the mutual inductance.

B. Inductance Matrix Method

In the inductance matrix method, the leakage and mutual inductance are calculated for each winding. The leakage inductance is transformed into an inductor with the same inductance, and the mutual inductance is transformed into a transformer with the same mutual inductance. Finally, the equivalent circuit is obtained by replacing each winding in the original component by a series-connection of the inductor and the transformers that represent the leakage and mutual inductance of the windings.

Now, we derive the equivalent circuit according to the inductance matrix method. To calculate the leakage and mutual inductance, we first solve the magnetic circuit model presented in Fig. 2.4. In the magnetic circuit, the flux follows Kirchhoff's current law, and the magnetomotive force follows Kirchhoff's voltage law. In calculation of the inductance, the method does not utilize the fact that the current of winding C is equal to the sum of windings 1 and 2. Therefore, we denote the current of the winding C as i_C. Hence, we have:

$$\begin{cases} R_{L1}\phi_{L1} = -N_O i_1, \\ R_{L2}\phi_{L2} = N_C i_C, \\ R_{L3}\phi_{L3} = -N_O i_2, \\ R_C\phi_2 - R_O\phi_1 = N_C i_C + N_O i_1, \\ R_C\phi_2 - R_O\phi_3 = N_C i_C + N_O i_2, \\ \phi_1 + \phi_2 + \phi_3 = 0. \end{cases} \tag{2.13}$$

Solving the above equations with respect to the fluxes, we obtain:

$$\phi_{L1} = -\frac{N_O}{R_{L1}} i_1, \quad \phi_{L2} = \frac{N_C}{R_{L2}} i_C, \quad \phi_{L3} = -\frac{N_O}{R_{L3}} i_2,$$

$$\phi_1 = -\frac{N_C}{R_O + 2R_C} i_C - \frac{(R_O + R_C)N_O}{R_O(R_O + 2R_C)} i_1 + \frac{R_C N_O}{R_O(R_O + 2R_C)} i_2,$$

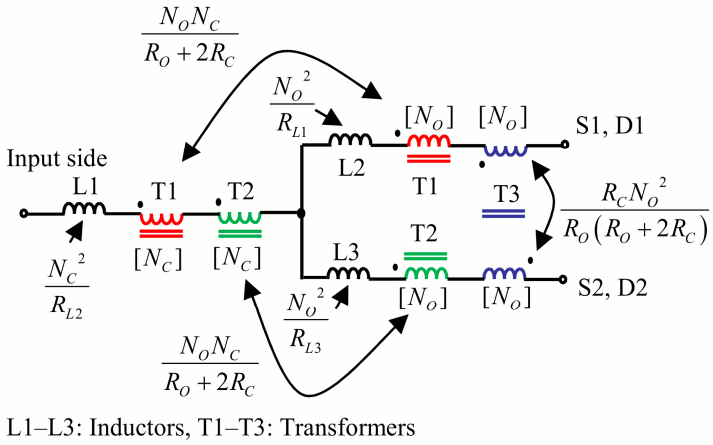

Fig. 2.7. Equivalent circuit by the inductance matrix method. Values in brackets are the number of turns. Values without brackets are the self-inductance for the inductors or the mutual inductance for the transformers.

$$\phi_2 = \frac{2N_C}{R_O + 2R_C} i_C + \frac{N_O}{R_O + 2R_C}(i_1 + i_2),$$

$$\phi_3 = -\frac{N_C}{R_O + 2R_C} i_C + \frac{R_C N_O}{R_O(R_O + 2R_C)} i_1 - \frac{(R_O + R_C)N_O}{R_O(R_O + 2R_C)} i_2. \tag{2.14}$$

We denote the total flux that interlinks with windings 1, C, and 2 as ϕ_{T1}, ϕ_{TC}, and ϕ_{T2}, respectively. Using the above equation, ϕ_{T1}, ϕ_{TC}, and ϕ_{T2} can be expressed as:

$$\phi_{T1} = -\frac{N_C}{R_O + 2R_C} i_C - \left\{\frac{R_O + R_C}{R_O(R_O + 2R_C)} + \frac{1}{R_{L1}}\right\} N_O i_1 + \frac{R_C N_O}{R_O(R_O + 2R_C)} i_2,$$

$$\phi_{TC} = \left(\frac{2}{R_O + 2R_C} + \frac{1}{R_{L2}}\right) N_C i_C + \frac{N_O}{R_O + 2R_C}(i_1 + i_2),$$

$$\phi_{T2} = -\frac{N_C}{R_O + 2R_C} i_C + \frac{R_C N_O}{R_O(R_O + 2R_C)} i_1 - \left\{\frac{R_O + R_C}{R_O(R_O + 2R_C)} + \frac{1}{R_{L3}}\right\} N_O i_2. \tag{2.15}$$

Next, we derive the inductance matrix. Electric functions of a magnetic component can be expressed as an inductance matrix. As for a magnetic component with three windings, the general definition of the matrix is expressed as:

$$\begin{pmatrix} V_1 \\ V_2 \\ V_3 \end{pmatrix} = \begin{pmatrix} -N_O \dfrac{d\phi_{T1}}{dt} \\ N_C \dfrac{d\phi_{TC}}{dt} \\ -N_O \dfrac{d\phi_{T2}}{dt} \end{pmatrix} = \begin{bmatrix} \Lambda_1 & M_{1C} & M_{12} \\ M_{1C} & \Lambda_C & M_{2C} \\ M_{12} & M_{2C} & \Lambda_2 \end{bmatrix} \begin{pmatrix} \dfrac{di_1}{dt} \\ \dfrac{di_C}{dt} \\ \dfrac{di_2}{dt} \end{pmatrix}, \tag{2.16}$$

where V_1, V_C, and V_2 are the induced voltage of windings 1, C, and 2, respectively; Λ_1, Λ_C, and Λ_2 are the self-inductance; and M_{1C}, M_{2C}, and M_{12} are the mutual-inductance. Substituting (6) into (7), the elements of the matrix are determined as follows:

$$\Lambda_1 = \left\{ \frac{R_O + R_C}{R_O(R_O + 2R_C)} + \frac{1}{R_{L1}} \right\} {N_O}^2,$$

$$\Lambda_C = \left(\frac{2}{R_O + 2R_C} + \frac{1}{R_{L2}} \right) {N_C}^2,$$

$$\Lambda_2 = \left\{ \frac{R_O + R_C}{R_O(R_O + 2R_C)} + \frac{1}{R_{L3}} \right\} {N_O}^2,$$

$$M_{1C} = M_{2C} = \frac{N_C N_O}{R_O + 2R_C},$$

$$M_{12} = -\frac{R_C {N_O}^2}{R_O(R_O + 2R_C)}. \tag{2.17}$$

We seek a circuit that represents the same inductance matrix, by replacing each winding by a series connection of an inductor and two transformers, as shown in Fig. 2.6. We assume that each transformer represents the magnetic coupling of a winding pair, and its mutual inductance is equal to the matrix element that corresponds to the coupling. Furthermore, it is assumed that the transformers have the same number of turns as the original winding.

Note that the self-inductance of the original winding equals the sum of self-inductance of the inductor and transformers. In other words, the self-inductance of the inductor corresponds to the leakage inductance [32] of the original winding. If the self-inductance of the inductors that replace windings 1, C, and 2 are denoted as L_1, L_C, and L_2, respectively, we obtain:

$$L_1 = \Lambda_1 - M_{1C} \frac{N_O}{N_C} - M_{12} \frac{N_O}{N_O} = \frac{{N_O}^2}{R_{L1}},$$

$$L_C = \Lambda_C - M_{1C} \frac{N_C}{N_O} - M_{2C} \frac{N_C}{N_O} = \frac{{N_C}^2}{R_{L2}},$$

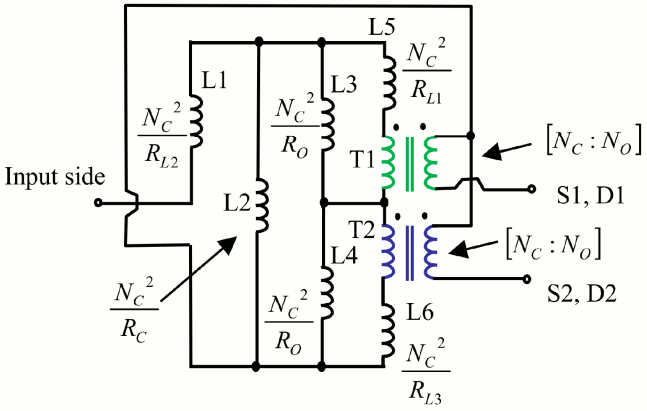

Fig. 2.8. Equivalent circuit by the duality method. Values in brackets are the ratios of the number of turns. Values without brackets are the self-inductance for the inductors.

$$L_2 = \Lambda_2 - M_{2C}\frac{N_O}{N_C} - M_{12}\frac{N_O}{N_O} = \frac{N_O^{\,2}}{R_{L3}}, \tag{2.18}$$

Finally, we obtained the circuit illustrated in Fig. 2.7. Obviously, this is the equivalent circuit of the integrated winding coupled inductor. The equivalent circuit has three inductors, because the method yields as many inductors as the windings. It also has three transformers, which are as many as the winding pairs.

C. Duality Method

The detailed process of this method is presented in [27], [28]. We followed this process to derive the equivalent circuit for Fig. 2.4.

The duality method does not require calculation of the inductance matrix or translation of the magnetic circuit into Lagrangian expression. Instead, it requires the following two steps.

The first step is to transform the magnetic circuit network. In this transformation, each series-connection of the network is replaced by a parallel-connection, and vice versa.

The second step is to replace each element of the magnetic circuit model by an electric component. In this step, each reluctance is replaced by an inductor, and all except one magnetomotive forces are replaced by an ideal transformer. The remaining magnetomotive force is eliminated to extract a pair of terminals. The primary windings of the ideal transformers and the pair of terminals correspond to the windings of the original integrated magnetic component.

Consequently, the equivalent circuit for Fig. 2.4 is obtained as Fig. 2.8. The equivalent circuit contains six inductors, which is as many as the reluctance in Fig. 2.4. It contains two transformers, which equals the magnetomotive force less one.

D. Comparison between the Equivalent Circuits

As seen above, the three methods yield their own equivalent circuits, all of which differ. Compared to Fig. 2.7 and Fig. 2.8, Fig. 2.5(b) contains fewer magnetic components. In this case, the Lagrangian method thus yields simpler equivalent circuit. Hence, in some cases the Lagrangian method can be a helpful method for discussing the overall electric functions of an integrated magnetic component. For example, the Lagrangian method may possibly be useful in some cases when we invent a novel magnetic structure.

The main drawback of the Lagrangian method is that the voltage induced in the windings of the integrated magnetic component does not appear in the equivalent circuit, because generally a winding is not directly replaced by transformers and inductors. On the other hand, the equivalent circuits produced by the inductance matrix and duality methods directly present the induced voltage of any windings. The reason is that a winding is replaced by a series of connected inductors and transformers in the inductance matrix method, and by the primary winding of an ideal transformer or a pair of terminals in the duality method. Therefore, if it is necessary to discuss the induced voltage to design the insulation of the windings, the inductance matrix or duality methods seem preferable.

2. 4. Analytical Equivalence of the Equivalent Circuits with the Magnetic Circuit Model

This section confirms that the equivalent circuit from the Lagrangian method has the same electric functions as the original magnetic circuit, similar to the equivalent circuits by the conventional inductance matrix and duality methods. For this purpose, we show that Fig. 2.5(b) is functionally equivalent to the original magnetic circuit, as well as Fig. 2.7. In order to discuss the functional equivalence, we employed the magnetic energy expressed as a function of current.

The electrical function of an integrated magnetic component can be fully determined if the magnetic energy $E(i_1,i_2,\ldots)$ is given as a function of the electric current. Here, we present a brief explanation of the reason.

We consider an arbitrary magnetic component with multiple current paths, and denote the voltage induced through the current path j as V_j. Because input energy equals the increase in magnetic energy, we have:

$$\sum_j V_j i_j = \sum_j \frac{\partial E}{\partial i_j}\frac{di_j}{dt}, \tag{2.19}$$

where i_j is the current of the current path j.

Because the magnetic energy is a quadratic form of the current, $\partial E/\partial i_j$ is a linear form of the current. By partially differentiating (2.19) with respect to the current, we obtain:

$$\begin{pmatrix} V_1 \\ V_2 \\ \vdots \end{pmatrix} = \begin{bmatrix} \dfrac{\partial E}{\partial i_1^{\,2}} & \dfrac{\partial E}{\partial i_1 \partial i_2} & \cdots \\ \dfrac{\partial E}{\partial i_1 \partial i_2} & \dfrac{\partial E}{\partial i_2^{\,2}} & \\ \vdots & & \ddots \end{bmatrix} \begin{pmatrix} \dfrac{di_1}{dt} \\ \dfrac{di_2}{dt} \\ \vdots \end{pmatrix}. \tag{2.20}$$

Equation (2.20) indicates that the energy expression $E(i_1,i_2,\ldots)$ is sufficient to determine the electrical input-output relation of the magnetic component. Hence, we only need to show that Fig. 2.5(b) and Fig. 2.7 belong to the same energy expression as that of the magnetic circuit model, in order to confirm the properness of the equivalent circuits.

First, we derive the energy expression for Fig. 2.4. The magnetic energy E_M of the whole magnetic circuit model is:

$$E_M = \frac{1}{2} R_O \phi_1^{\,2} + \frac{1}{2} R_C \phi_2^{\,2} + \frac{1}{2} R_O \phi_3^{\,2} + \sum_{i=1}^{3} \frac{1}{2} R_{Li} \phi_{Li}^{\,2}. \tag{2.21}$$

The energy expression of Fig. 2.4 is obtained by expressing the above equation as a function of i_1 and i_2. With a view to this purpose, the fluxes ϕ_1–ϕ_3 are expressed as functions of i_1 and i_2 in advance. Substituting $i_C=i_1+i_2$ into (2.14) yields:

$$\begin{aligned} \phi_1 &= -\frac{1}{2}\frac{N_O+2N_C}{R_O+2R_C}(i_1+i_2) - \frac{1}{2}\frac{N_O}{R_O}(i_1-i_2), \\ \phi_2 &= \frac{N_O+2N_C}{R_O+2R_C}(i_1+i_2), \\ \phi_3 &= -\frac{1}{2}\frac{N_O+2N_C}{R_O+2R_C}(i_1+i_2) + \frac{1}{2}\frac{N_O}{R_O}(i_1-i_2). \end{aligned} \tag{2.22}$$

Substituting (2.14) and (2.22) into (2.21) leads to:

$$\begin{aligned} E_M = {} & \frac{1}{4} R_O \left(\frac{N_O+2N_C}{R_O+2R_C} \right)^2 (i_1+i_2)^2 + \frac{1}{4}\frac{N_O^{\,2}}{R_O}(i_1-i_2)^2 \\ & + \frac{1}{2} R_C \left(\frac{N_O+2N_C}{R_O+2R_C} \right)^2 (i_1+i_2)^2 + \frac{1}{2}\frac{N_O^{\,2}}{R_{L1}} i_1^{\,2} + \frac{1}{2}\frac{N_C^{\,2}}{R_{L2}}(i_1+i_2)^2 + \frac{1}{2}\frac{N_O^{\,2}}{R_{L3}} i_2^{\,2}. \end{aligned} \tag{2.23}$$

This is then compared with the energy expression of Fig. 2.5(b) and Fig. 2.7. The energy expression E_{Lag} for Fig. 2.5(b) is:

$$E_{Lag} = \frac{1}{2}\left\{ \frac{N_C{}^2}{R_{L2}} + \frac{\left(N_C + \frac{N_O}{2}\right)^2}{R_C + \frac{R_O}{2}} \right\}(i_1 + i_2)^2 + \frac{1}{2}\frac{N_O{}^2}{2R_O}(i_1 - i_2)^2$$

$$+ \frac{1}{2}\frac{N_O{}^2}{R_{L1}} i_1{}^2 + \frac{1}{2}\frac{N_O{}^2}{R_{L3}} i_2{}^2. \qquad (2.24)$$

On the other hand, the energy expression E_{Matrix} for Fig. 2.7 is:

$$E_{Matrix} = \frac{1}{2}\frac{N_C{}^2}{R_{L2}}(i_1 + i_2)^2 + \frac{1}{2}\frac{1}{R_O + 2R_C}(N_C i_1 + N_C i_2 + N_O i_1)^2$$

$$+ \frac{1}{2}\frac{1}{R_O + 2R_C}(N_C i_1 + N_C i_2 + N_O i_2)^2 + \frac{1}{2}\frac{N_O{}^2}{R_{L1}} i_1{}^2 + \frac{1}{2}\frac{N_O{}^2}{R_{L3}} i_2{}^2$$

$$+ \frac{1}{2}\frac{R_C N_O{}^2}{R_O(R_O + 2R_C)}(i_1 - i_2)^2. \qquad (2.25)$$

Table. 2.1. Specifications of the Prototype Converter.

PARAMETER	Value
Input voltage V1	20–180 V
Output voltage (The voltage of C2)	200 V
Duty Ratio	0.1–0.9
Switching Frequency	50kHz
Semiconductor Devices (S1, S2, D1, D2)	MG50J1ZS40 (IGBT+Diode)
Decoupling Capacitors (C1, C2)	3300μF (Electrolytic Capacitor)
Winding Turn Number (N_C, N_O)	13 Turns
Reluctance R_C	14.4 A/μWb
Reluctance R_O	0.192 A/μWb
Reluctance R_{L1}	8.83 A/μWb
Reluctance R_{L2}	169 A/μWb
Reluctance R_{L3}	9.06 A/μWb

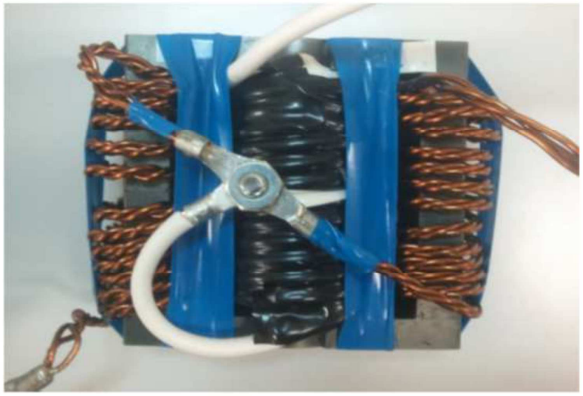

Fig. 2.9. Photograph of the integrated winding coupled inductor employed for the prototype converter.

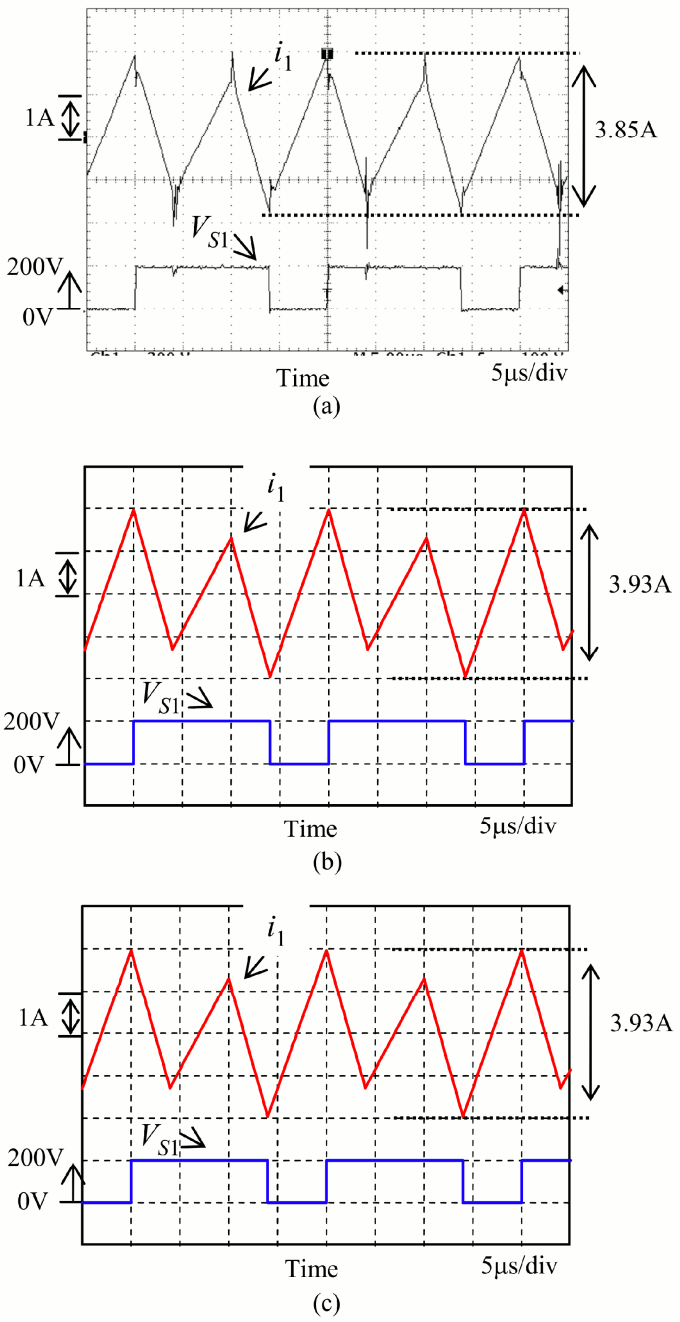

Fig. 2.10. Experimental and simulated waveforms of the current of the winding 1 (i_1) and the voltage across S1 (V_{S1}). (a) Experiment. (b) Simulation based on the Lagrangian method. (c) Simulation based on the inductance matrix method.

Equations (2.23)–(2.25) can be developed to obtain $E_M=E_{Lag}=E_{Matrix}$. Consequently, both Fig. 2.5(b) and Fig. 2.7 are shown to have the same electric functions as the magnetic

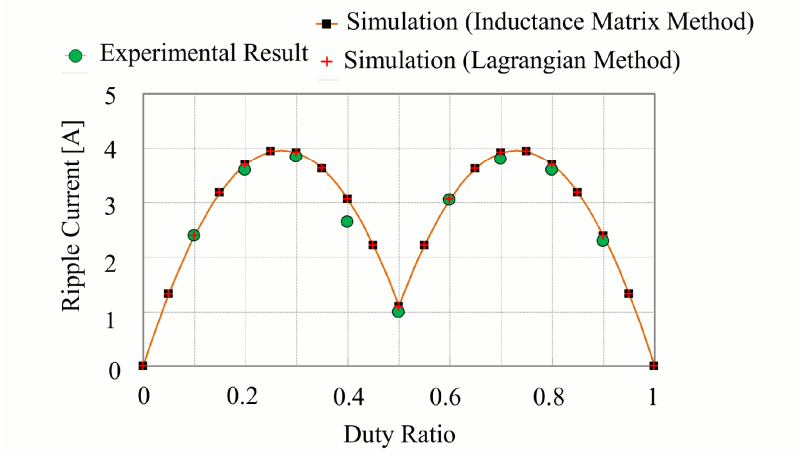

Fig. 2.11. Experimental and simulated ripple current in the current of the winding 1 (i_1)

circuit model.

2. 5. Consistency with Experimental Behavior

This section confirms consistency of the equivalent circuits with experimental behavior of the integrated magnetic component. Current waveforms of the converter shown in Fig. 2.3 were simulated utilizing the equivalent circuit shown in Fig. 2.5(b) and Fig. 2.7. The results were then compared with the experimental waveforms of a prototype converter with the integrated magnetic component. We employed SCAT K.460PR1 (Keisoku Giken Co., Ltd.) as the simulator.

The specifications of the prototype are given in Table 2.1, and a photograph of the magnetic component in Fig. 2.9. To simplify the waveform, the converter was operated under the continuous conduction mode. Hence, R_O is designed to be far smaller than the design concept presented in [4]. We equipped no gap on the outer legs. The reluctance of the magnetic circuit is estimated from results of inductance measurement of the magnetic component. Details of the estimation are presented in the appendix.

First, we compared the experimental and simulated waveform of the current i_1, when the duty ratio is set at 0.3. The result is shown in Fig. 2.10. Figure 2.10(a) is the experimental waveform, and Fig. 2.10(b) and Fig. 2.10 (c) are the simulated waveforms of the equivalent circuits by the Lagrangian method and the inductance matrix method, respectively. The two simulated waveforms are identical, indicating equivalency between the two equivalent circuits, as expected from the previous section. In addition, the simulation predicted the experimental waveform well, except for surge current during the switching of S1 and S2.

Next, we compared the simulated current ripple of i_1 with the experimental result over several duty ratios. The result is shown in Fig. 2.11. As expected from the previous section, the simulation of the two equivalent circuits resulted in the same current ripple. In

addition, the simulation successfully predicted dependency of the ripple current on duty ratio. Hence, the result also supported consistency of the equivalent circuit with the experiment. Certainly, the experiment showed that the ripple current was slightly smaller than predicted when the duty ratio was set at 0.4. The reason for this is not clear. However, the surge current during switching of S1 and S2 may have caused measurement deviation of the ripple current.

Consequently, we concluded that the experiment also supported the properness of the equivalent circuits.

2. 6. Conclusions

This chapter proposed a Lagrangian method to derive the equivalent circuit of an integrated magnetic component. This method is expected to derive a simpler circuit than the conventional inductance matrix and duality methods, when applied to an integrated magnetic component with few flux paths that can be magnetized independently. An example using the integrated winding coupled inductor verified that the Lagrangian method actually derives simplest equivalent circuit of the integrated winding coupled inductor compared to the conventional methods.

In addition, this chapter investigated equivalent circuits of the integrated winding coupled inductor in order to verify the properness of the equivalent circuit by the Lagrangian method. The equivalent circuits were derived using the Lagrangian, inductance matrix, and duality methods, respectively. Then, this chapter investigated the consistency of the equivalent circuit by the Lagrangian method with the magnetic circuit model, and the experimental behavior of the integrated winding coupled inductor. The results showed the equivalent circuit was functionally equivalent to the magnetic circuit model, and predicted the experimental behavior as well as the equivalent circuit produced by the inductance matrix method.

Consequently, these results support that the Lagrangian method provides proper equivalent circuits, and in some cases is useful for deriving simple equivalent circuits.

2. 7. Appendix

The reluctance of the prototype of the integrated winding coupled inductor was estimated based on measurement of the self-inductance of all windings, and the mutual inductance of all winding pairs. The self-inductance is the inductance of a winding when all the other windings are opened. The result of the measurements is presented in Table 2.2.

We can analytically express the inductance as functions of the reluctance. By equating the expression to the measured inductance, the reluctance can be determined.

The expression of the self and mutual inductance are already obtained in (2.17) by the inductance matrix method. However, this does not indicate that the inductance matrix method is more useful than the Lagrangian method, because we can also derive the same result by the latter. In order to prove this, we here employ the Lagrangian method to derive the expression.

We consider that the windings in Fig. 2.4 are disconnected each from the other. Then, Lagrangian L' of Fig. 2.4 can be described introducing q_C, which is the cumulative charge through the winding C:

$$L' = -N_O\dot{q}_1(\phi_1+\phi_{L1}) + N_C\dot{q}_C(\phi_2+\phi_{L2}) - N_O\dot{q}_2(\phi_3+\phi_{L3}) - \frac{1}{2}R_{L1}{\phi_{L1}}^2$$
$$-\frac{1}{2}R_{L2}{\phi_{L2}}^2 - \frac{1}{2}R_{L3}{\phi_{L3}}^2 - \frac{1}{2}R_O{\phi_1}^2 - \frac{1}{2}R_C{\phi_2}^2 - \frac{1}{2}R_O{\phi_3}^2 + \lambda(\phi_1+\phi_2+\phi_3). \quad (2.26)$$

We simplify (2.26) by eliminating λ and introducing $\phi_A=\phi_1+\phi_2/2$. Then, we have:

$$L' = -N_O\dot{q}_1\left(\phi_A - \frac{\phi_2}{2} + \phi_{L1}\right) + N_C\dot{q}_C(\phi_2+\phi_{L2}) - N_O\dot{q}_2\left(-\phi_A - \frac{\phi_2}{2} + \phi_{L3}\right)$$
$$-\frac{1}{2}R_{L1}{\phi_{L1}}^2 - \frac{1}{2}R_{L2}{\phi_{L2}}^2 - \frac{1}{2}R_{L3}{\phi_{L3}}^2 - R_O{\phi_A}^2 - \left(\frac{R_C}{2}+\frac{R_O}{4}\right){\phi_2}^2. \quad (2.27)$$

First, we determine the mutual inductance M_{1C} between the windings 1 and C. By substituting $q_2=0$, we can obtain the equivalent circuit of the magnetic component, when the winding 2 is opened:

$$L' = -N_O\dot{q}_1\left(\phi_A - \frac{\phi_2}{2} + \phi_{L1}\right) + N_C\dot{q}_C(\phi_2+\phi_{L2})$$
$$-\frac{1}{2}R_{L1}{\phi_{L1}}^2 - \frac{1}{2}R_{L2}{\phi_{L2}}^2 - \frac{1}{2}R_{L3}{\phi_{L3}}^2 - R_O{\phi_A}^2 - \left(\frac{R_C}{2}+\frac{R_O}{4}\right){\phi_2}^2. \quad (2.28)$$

Now, we consider Lagrangian L_{temp} of an arbitrary circuit with the magnetic component represented by (2.28). In other words, L_{temp} contains the above Lagrangian L'. Because L_{temp} does not contain ϕ_{L3} except L', Euler-Lagrange equation (1.26) of L_{temp} with respect to ϕ_{L3} gives $\phi_{L3}=0$. Therefore, we can eliminate ϕ_{L3} from (2.28), obtaining:

$$L' = -N_O\dot{q}_1\phi_A - R_O{\phi_A}^2 - N_O\dot{q}_1\phi_{L1} - \frac{1}{2}R_{L1}{\phi_{L1}}^2 + N_C\dot{q}_C\phi_{L2} - \frac{1}{2}R_{L2}{\phi_{L2}}^2$$
$$+\left(\frac{N_O}{2}\dot{q}_1 + N_C\dot{q}_C\right)\phi_2 - \left(\frac{R_C}{2}+\frac{R_O}{4}\right){\phi_2}^2. \quad (2.29)$$

The above Lagrangian can be translated into Fig. 2.12(a). Therefore, the mutual inductance M_{1C} is:

$$M_{1C} = \frac{N_O N_C}{R_O + 2R_C}. \quad (2.30)$$

Table. 2.2. Measurement Result of Self- and Mutual Inductance

PARAMETER	Value
Self-inductance of the winding 1 (Λ_1)	462 μH
Self-inductance of the winding C (Λ_C)	12.7 μH
Self-inductance of the winding 2 (Λ_2)	461.5 μH
Mutual-inductance between the windings 1 and C (M_{1C})	5.85 μH
Mutual-inductance between the windings 1 and 2 (M_{12})	437 μH
Mutual-inductance between the windings 2 and C (M_{2C})	5.85 μH

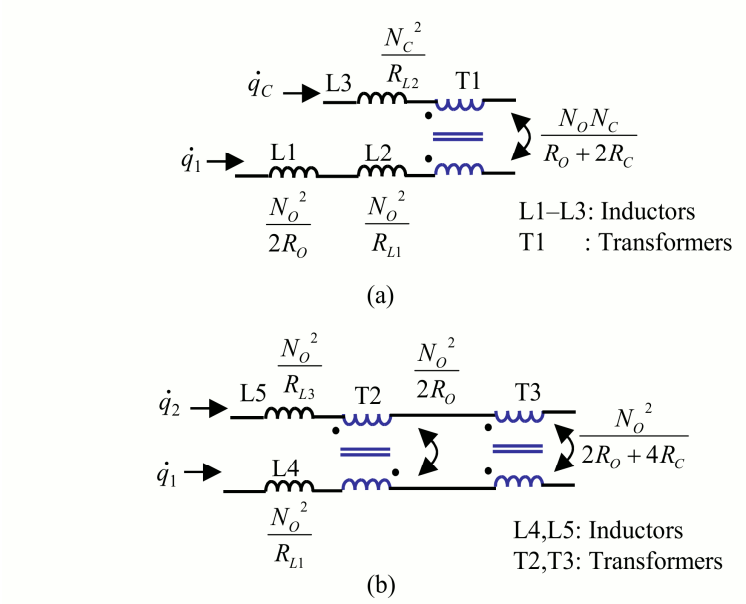

Fig. 2.12. Translation from Lagrangian expression into circuit diagram. (a) Equation (19). (b) Equation (25).

Next, the self-inductance Λ_1 of winding 1 is obtained by further opening winding C. Substituting q_C=0 into (2.29) yields:

$$L' = -N_O \dot{q}_1 \phi_{L1} - \frac{1}{2} R_{L1} \phi_{L1}^{\ 2} - N_O \dot{q}_1 \phi_A - R_O \phi_A^{\ 2} + \frac{N_O}{2} \dot{q}_1 \phi_2 - \left(\frac{R_C}{2} + \frac{R_O}{4} \right) \phi_2^{\ 2} . \tag{2.31}$$

We eliminated the term with ϕ_{L2} in (2.31), because Euler-Lagrange equation with respect to ϕ_{L2} now yields ϕ_{L2}= 0.

Equation (2.31) corresponds to series-connected inductors whose inductances are N_O^2/R_{L1}, $N_O^2/2R_O$, and $N_O^2/(2R_O+4R_C)$, respectively. Therefore, we have:

$$\Lambda_1 = \frac{N_O^{\ 2}}{R_{L1}} + \frac{N_O^{\ 2}}{2R_O} + \frac{N_O^{\ 2}}{2R_O + 4R_C} . \tag{2.32}$$

Similarly, the self-inductance Λ_C of winding C is obtained by substituting q_1=0 into (2.29). Then, ϕ_{L1}=0 and ϕ_A=0 can be substituted, according to the similar reason described above. As a result, we have:

$$L' = N_C \dot{q}_C \phi_{L2} - \frac{1}{2} R_{L2} {\phi_{L2}}^2 + N_C \dot{q}_C \phi_2 - \left(\frac{R_C}{2} + \frac{R_O}{4} \right) {\phi_2}^2 . \tag{2.33}$$

Equation (2.33) corresponds to series connected inductors whose inductances are N_C^2/R_{L2} and $2N_C^2/(R_O+2R_C)$. Hence, we have:

$$\Lambda_C = \frac{{N_C}^2}{R_{L2}} + \frac{2{N_C}^2}{R_O + 2R_C} . \tag{2.34}$$

Then, we determine the mutual inductance M_{12} between windings 1 and 2. Now, only winding C is opened. Thus, substitute q_C=0 into (2.27) to obtain:

$$\begin{aligned} L' = {} & -N_O \dot{q}_1 \phi_{L1} - \frac{1}{2} R_{L1} {\phi_{L1}}^2 - N_O \dot{q}_2 \phi_{L3} - \frac{1}{2} R_{L3} {\phi_{L3}}^2 + \left(N_O \dot{q}_2 - N_O \dot{q}_1 \right) \phi_A - R_O {\phi_A}^2 \\ & + \left(N_O \dot{q}_1 + N_O \dot{q}_2 \right) \frac{\phi_2}{2} - \left(\frac{R_C}{2} + \frac{R_O}{4} \right) {\phi_2}^2 . \end{aligned} \tag{2.35}$$

Note that we eliminated the term with ϕ_{L2}, similarly as in (2.31). Equation (2.35) can be translated into Fig. 12(b). Therefore, the mutual inductance M_{12} is:

$$M_{12} = \frac{R_C {N_O}^2}{R_O \left(R_O + 2R_C \right)} . \tag{2.36}$$

According to similar discussion to obtain (2.30) and (2.32), we obtain the self-inductance Λ_2 of winding 2 and the mutual inductance M_{2C} between windings 2 and C:

$$\Lambda_2 = \frac{{N_O}^2}{R_{L3}} + \frac{{N_O}^2}{2R_O} + \frac{{N_O}^2}{2R_O + 4R_C} . \tag{2.37}$$

$$M_{2C} = \frac{N_O N_C}{R_O + 2R_C} . \tag{2.38}$$

Finally, the reluctance can determined by equating Table 2.2 with (2.30), (2.32), (2.34), (2.36)–(2.38), obtaining the values of reluctance shown in Table 2.1.

REFERENCES

[1] P. Zumel, O. Garcia, J. A. Cobos, and J. Uceda, "Magnetic integration for interleaved converters," in Proc. Appl. Power Electron. Conf. and Expo., 2003, vol. 2, pp. 1143-1149.

[2] S. Chandrasekaran and L. U. Gokdere, "Integrated magnetics for interleaved DC-DC boost converter for fuel cell powered vehicles," in Proc. Power Electronics Specialists Conf., 2004, pp. 356-361.

[3] W. Li, P. Li, H. Yang, and X. He, "Three-level forward-flyback phase-shift ZVS converter with integrated series-connected coupled inductors," IEEE Trans. Power Electron., vol. 27, no. 6, pp. 2846-2856, Jun. 2012.

[4] Wei Wen, and Y.-S. Lee, "A two-channel interleaved boost converter with reduced core loss and copper loss," in Proc. Power Electronics Specialists Conf., 2004, pp. 1003-1009.

[5] D. K.-W. Cheng, Leung-Pong Wong, and Y.-S. Lee, "Design, modeling, and analysis of integrated magnetics for power converters," in Proc. Power Electronics Specialists Conf., 2000, vol. 1, pp. 320-325.

[6] Leung-Pong Wong, Y. S. Lee, D. K. W. Cheng, and M. H. L. Chow, "Two-phase forward converter using an integrated magnetic component," IEEE Trans. Aerosp. Electron. Syst., vol. 40, no. 4, pp. 1294-1310, Oct. 2004.

[7] L. Yan, and B. Lehman, "An integrated magnetic isolated two-inductor boost converter: analysis, design and experimentation," IEEE Trans. Power Electron., vol. 20, no. 2, pp. 332-342, Mar. 2005.

[8] E. Laboure, A. Cuniere, T. A. Meynard, F. Forest, and E. Sarraute, "A theoretical approach to intercell transformers, application to interleaved converters," IEEE Trans. Power Electron., vol. 23, no. 1, pp. 464-474, Jan. 2008

[9] L. P. Wong, Y. S. Lee, M. H. L. Chow, and D. K. W. Cheng, "A four-phase forward converter using an integrated transformer," IEEE Trans. Ind. Electron., vol. 55, no. 2, pp.817-831, Feb. 2008.

[10] J. Sun and V. Mehrotra, "Orthogonal winding structures and design for planar integrated magnetics," IEEE Trans. Ind. Electron., vol. 55, no. 3, pp. 1463-1469, Mar. 2008.

[11] T. Kawashima, S. Funabiki, and M. Yamamoto, "Recovery-less boost converter for electric vehicle," in Proc. European Conf. Power Electron. and Applicat., 2009, pp. 1-10.

[12] J. Salmon, J. Ewanchuk, and A. M. Knight, "PWM inverters using split-wound coupled inductors," IEEE Trans. Ind. Appl., vol. 45, no. 6, pp. 2001-2008, Nov./Dec. 2009.

[13] M. Nakahama, M. Yamamoto, and Y. Satake, "Trans-linked multi-phase boost converter for electric vehicle," in Proc. Energy Conversion Congr. and Expo., 2010, Atlanta, pp. 2458-2463.

[14] H. N. Nagaraja, D. Kastha, and A. Patra, “Design principles of a symmetrically coupled inductor structure for multiphase synchronous buck converters,” IEEE Trans. Ind. Electron., vol. 58, no. 3, pp. 988-997, Mar. 2011.

[15] S. Roy and L. Umanand, “Integrated magnetics-based multisource quality AC power supply,” IEEE Trans. Ind. Electron., vol. 58, no. 4, pp. 1350-1358, April 2011.

[16] F. Yang, X. Ruan, Y. Yang, and Z. Ye, “Interleaved critical current mode boost PFC converter with coupled inductor,” IEEE Trans. Power Electron., vol. 26, no. 9, pp. 2404-2413, Sept. 2011.

[17] Z. Ouyang, Z. Zhang, O. C. Thomson, and M. A. E. Andersen, “Planar-integrated magnetics (PIM) module in hybrid bidirectional DC-DC converter for fuel cell application,” IEEE Trans. Power Electron., vol. 26, no. 11, pp. 3254-3264, Nov. 2011.

[18] S. Utz and J. Pforr, “Operation of multi-phase with coupled inductors at reduced numbers of phases,” in Proc. 14th European Conf. Power Electron. Applicat. (EPE), 2011, pp. 1-10.

[19] N. Zhu, J. Kang, D. Xu, B. Wu, and Y. Xiao, “An integrated AC choke design for common-mode current suppression in neural-connected power converter systems,” IEEE Trans. Power Electron., vol. 27, no. 3, pp. 1228-1236, Mar. 2012.

[20] D. O. Boillat and J. W. Kolar, “Modeling and experimental analysis of a coupled inductor employed in a high performance AC power source,” in Proc. Intl. Conf. Renewable Energy Research Applicat. (ICRERA), 2012, pp. 1-18.

[21] J. Imaoka, M. Yamamoto, K. Umetani, S. Arimura, and T. Hirano, “Characteristics analysis and performance evaluation for interleaved boost converter with integrated winding coupled inductor,” in Proc. Energy Conversion Congr. Expo., 2013, pp. 3711-3718.

[22] K. J. Hartnett, J. G. Hayes, M. G. Egan, and M. S. Rylko, “CCTT-core split-winding integrated magnetic for high-power DC-DC converters,” IEEE Trans. Power Electron., vol. 28, no. 11, pp. 4970-4984, Nov. 2013.

[23] C. Deng, D. Xu, P. Chen, C. Hu, W. Zhang, Z. Wen, and X. Wu, “Integration of both EMI filter and boost inductor for 1kW PFC converter,” IEEE Trans. Power Electron., vol. PP, issue 99, pp. 1, 2014

[24] K. Umetani, F. Iwamoto, and K. Yagyu , “A unidirectional boost chopper with snubber energy regeneration using a coupled inductor,” IEEJ Trans. Elect. Electron. Eng., vol 9, no. 3, pp. 315-323, May 2014.

[25] K. Umetani, T. Tera, K. Shirakawa, “Novel magnetic structure of integrated differential-mode and common-mode inductors to suppress DC saturation,” IEEJ Trans. Ind. Appl. (in press)

[26] J. D. Kraus, “Time changing electric and magnetic field,” in Electromagnetics, 4th ed., New York: McGraw-Hill, 1991, pp. 432-435.

[27] S. A. El-Hamamsy and E. I. Chang, “Magnetics modeling for computer-aided design of power electroncs circuits,” in Proc. Power Electron. Specialist Conf. (PESC), 1989, vol. 2, pp. 635-645.

[28] G. W. Ludwig and S. A. El-Hamamsy, “Coupled inductor and reluctance models of magnetic components,” IEEE Trans. Power Electron., vol. 6, no. 2, pp. 240-250, April 1991.

[29] S. V. Marshall, and G. G. Skitek, “Magnetic circuits,” in Electromagnetic concepts and applications, 3rd ed., New Jersey: Prentice Hall, 1990, pp. 276-283.

[30] C. Lanczos, “Kinosthenic or ignorable variables and their elimination,” in The Variational Principles of Mechanics, 4th ed., New York: Dover, 1970, pp.125-130.

[31] L. D. Landau and E. M. Lifshitz, “Canonical tranformations” in Mechanics, Oxford, U. K.: Butterworth- Heinemann, 1976, pp.143-146.

[32] A. Van den Bossche, and V. C. Valchev, “Fundamentals of magnetic theory,” in Inductors and transformers for power electronics, Florida: CRC Press, 2005, pp. 17-29.

Chapter 3

LAGRANGIAN METHOD FOR DERIVING ELECTRICALLY DUAL POWER CONVERTERS APPLICABLE TO NON-PLANAR CIRCUIT TOPOLOGIES

3. 1. Introduction

The duality principle [1] is widely recognized as one of the most basic features of power converters. Power converters can be primarily classified as voltage-source converters, which convert electrical energy from a voltage source, and current-source converters, which convert energy from a current source. In general, voltage-source converters have dynamically equivalent current-source counterparts and vice versa. This correspondence relationship is called as the duality principle.

The duality principle is often utilized in power electronics research. One of its most common uses is in the derivation of novel circuits [2]–[4]. In other words, novel circuits may be discovered by deriving dual converters from their already known counterparts. In other cases, the principle can be utilized for analyzing circuit behavior [5]. For this purpose, the circuit behavior of the dual are first analyzed instead of focusing on the target circuit, and then the behavior of the target circuit is inferred from the result.

These methods of utilizing the duality principle require duality transformation, namely, the derivation of the duals. If the original circuits have a simple topology, their duals can be guessed in many cases. However, complicated circuits generally do not allow an intuitive approach. Hence, several analytical methods of duality transformation have been studied and proposed.

The basic method of duality transformation is based on the interchange between the voltage and the current of every component in the original circuit [1]. The interchange can be performed by means of topological transformation, through which series connections of the original circuit are replaced by parallel connections and parallel connections by series connections.

However, topological transformation is applicable only to planar circuits [1], which do not contain any pair of wires crossing each other without connection. Meanwhile, many non-planar circuits are known to have their own duals, although the duals are not related to the original circuits perfectly by topological transformation. Thus, the basic method of the duality transformation is not directly applicable to deriving duals for non-planar circuits.

To address the problem, some techniques [6]–[9] that apply topological transformation partially to avoid non-planarity have been proposed. However, they seem to raise another problem in that a dual derived by a technique cannot necessarily be derived by another

[†] Reprinted, with permission, from K. Umetani, Lagrangian method for deriving electrically dual power converters applicable to non-planar circuit topologies, IEEJ Transactions on Electrical and Electronic Engineering, Jul. 2016.

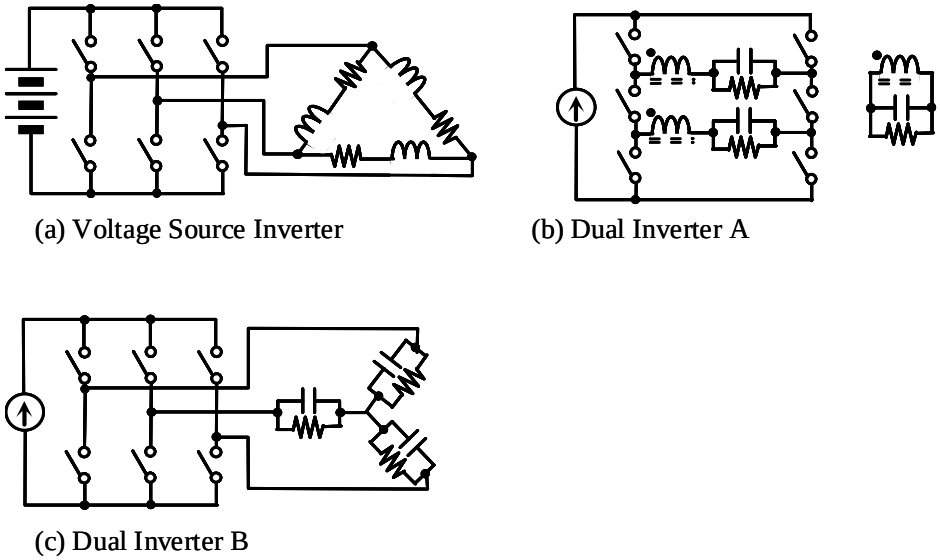

Fig. 3.1. Three phased voltage source inverter and its duals

technique, as presented below. Accordingly, the duality transformation of non-planar circuits still seems to require intuitive insight in selecting an appropriate technique in order to derive a desired dual. Therefore, the application of the duality principle can probably be promoted by proposing a more universal method of duality transformation that derives all possible duals systematically.

The following discussion of the aforementioned problem uses specific examples of non-planar circuits. Figure 3.1(a) illustrates a typical three-phase voltage-source inverter. Because this circuit is widely utilized in the industry, its duality has been actively researched [6]–[11]. We apply the previously reported methods to this circuit to show that none of them can derive all duals.

In one method [6][7], the original circuit is disassembled into a set of planar circuits by adding ideal transformers. Then, the resulting planar circuits are individually converted by topological transformation, and finally, they are assembled into a dual. Consequently, the derived dual contains the additional transformers introduced in the disassembly process. According to the method, we obtain the dual illustrated in Fig. 3.1(b) from the original inverter shown in Fig. 3.1(a). The method is beneficial as a systematic procedure of transformation. Nonetheless, there is still a dual that cannot be derived by the method. In fact, the circuit illustrated in Fig. 3.1(c) is also known to be a dual [10][11]. However, the circuit cannot be derived by the method, because it contains no transformer.

Contrarily, two methods have been proposed that derive Fig. 3.1(c). One utilizes the fact that every instantaneous current path of the original inverter forms a planar circuit [8]. The method derives the dual by applying topological transformation to the instantaneous current patterns of every operation mode, and then, it seeks a circuit that provides the transformed current patterns as its operation mode. The other method replaces each leg of the original inverter with a voltage-controllable voltage source and then applies a topological transformation [9]. These methods are successfully applied to the three-phase inverter. However, their universal applicability remains unclear, because

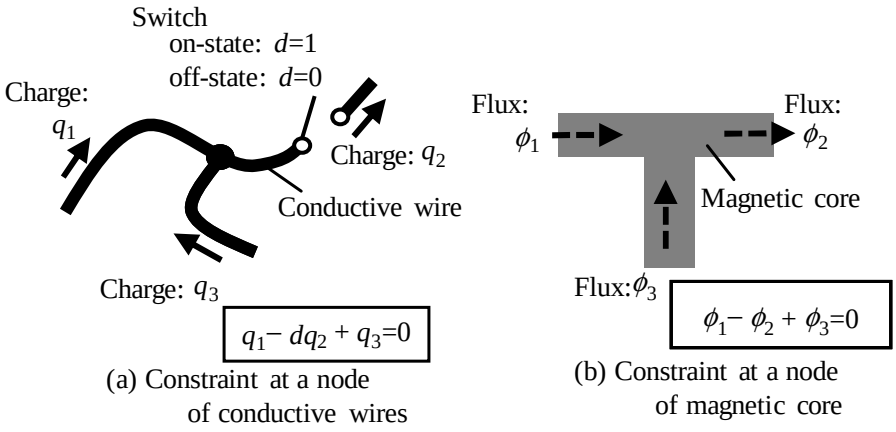

Fig. 3.2. Holonomic constraints of electric and magnetic node

it is not ensured that they always yield planar networks for any non-planar circuits. Furthermore, they are also unable to derive all duals, because they add no ideal transformer, and consequently, they do not lead to Fig. 3.1(b).

The abovementioned difficulty is closely related to the method of avoiding non-planarity in order to apply the topological transformation. Therefore, the problem may be addressed by inventing another method of duality transformation that does not utilize topological transformation. The aim of this chapter is to propose a candidate by discussing another approach to duality transformation.

Instead of topological transformation, the proposed method is based on Lagrangian dynamics. According to Lagrangian dynamics, every power converter has its own Lagrangian [12]–[14] expression. The dynamics provides systematic methods to transform a Lagrangian into another dynamically equivalent Lagrangian. The proposed method first expresses the original circuit as Lagrangian. Then, the Lagrangian is transformed using Lagrangian dynamics into another equivalent Lagrangian that belongs to the dual. Finally, the transformed Lagrangian is translated into a physical circuit topology to obtain the dual.

The next section theoretically discusses formulation of the proposed method. Section 3.3 explores two examples of duality transformation. These examples derive already-known duals to verify the proposed method. In particular, one example systematically derives both Fig. 3.1(b) and Fig. 3.1(c) from Fig. 3.1(a), suggesting that the proposed method is more universal for deriving various duals of non-planar circuits.

3. 2. Duality Transformation by Lagrangian Dynamics

A. Lagrangian Modeling

Many previous papers have discussed Lagrangian modeling for power converters. The typical modeling method [12][13] regards energy in inductors as kinetic energy and energy in capacitors as potential energy. Thus, the method models a circuit of inductors and capacitors by the Lagrangian

$$L = \sum_t \frac{1}{2} \Lambda_i \dot{q}_i^{\,2} - \sum_j \frac{1}{2C_j} q_j^{\,2} + \sum_k E_k q_k \ , \tag{3.1}$$

where i, j, and k are the indexes of the inductors, capacitors, and voltage sources, respectively; Λ_i is the inductance of the inductor i, and q_i is the electric charge that flows through it; C_j is the capacitance of the capacitor j, and q_j is the charge stored in it; E_k is the voltage of the voltage source k, and q_k is the charge that flows from it. The dot above a variable indicates its time derivative. Hence, charge q is the physical charge stored in a capacitor in the second right-hand term of (3.1), and it is also the time integrated current [14] as defined by (3.2) in the first and third right-hand terms.

$$q = \int_{t_0}^{t} I dt \ , \tag{3.2}$$

where t is the time, t_0 is the initial time, and I is the current that flows through the component under consideration.

This modeling is limited to power converters composed only of inductors and capacitors. Thus, it cannot handle converters with transformers or magnetic circuits. To address this problem, a novel Lagrangian formulation was proposed recently [14]. The method models the windings and the magnetic paths separately. The first right-hand term of (3.1) is split into the Lagrangian of the windings (the first right-hand term of (3.5)) and that of the magnetic paths (the second right-hand term of (3.5)).

In addition, the definition of charge q is unified to (3.2). This enables the electrical networks to be implemented as a set of holonomic constraints, each defined at a node representing that the sum of the charge flowing into the node should remain zero, as shown in Fig. 3.2(a).

A switch on the current path is modeled by regarding a node connected to the current path as a holonomic constraint that can be switched according to the state variable of the switch. For example, the constraint of the node shown in Fig. 3.2(a) is expressed as $q_1 - dq_2 + q_3 = 0$, where d is a function of the switching state that takes $d = 1$ in the on-state and $d = 0$ in the off-state. Therefore, the constraint at the electrical node r can be generally expressed as

$$f_r(q;s) = z_{r1}(s)q_1 + z_{r2}(s)q_2 + \cdots = 0 \ , \tag{3.3}$$

where $f_r(q;s)$ is a linear function of the charge q_1, q_2, … ; s is the state variable of switches; and z_{r1}, z_{r2}, … are functions of s or constant integers that take any one of +1, 0, or −1.

Similarly, the magnetic networks are implemented as a set of holonomic constraints representing that the total flux flowing into a magnetic node should remain zero, as shown in Fig. 3.2(b). For example, the constraint at the node shown in Fig. 3.2(b) is expressed as $\phi_1 - \phi_2 + \phi_3 = 0$. Thus, the constraint at the magnetic node u can be generally be expressed in the following form:

$$g_u(\phi) = \eta_{u1}(s)\phi_1 + \eta_{u2}(s)\phi_2 + \cdots = 0 \ , \tag{3.4}$$

where $g_u(\phi)$ is a linear function of the flux ϕ_1, ϕ_2, …; and η_{u1}, η_{u2}, … are constant integers that take any one of +1, 0, or −1.

Consequently, the general expression of the Lagrangian has the form

$$L = \sum_n N_n \dot{q}_n \phi_n - \sum_m \frac{1}{2P_m} \phi_m^{\,2} - \sum_j \frac{1}{2C_j} \left(Q_j - q_j\right)^2 + \sum_k E_k q_k + \sum_r \lambda_{Er} f_r(q;s) + \sum_u \lambda_{Mu} g_u(\phi), \tag{3.5}$$

where n and m are the indexes of windings and branches of magnetic paths, respectively; N_n is the number of turns of the winding n, q_n is the charge that flows through it, and ϕ_n is the flux that links with it; P_m is the permeance of the branch m of a magnetic path, and ϕ_m is its flux; Q_j is the initial charge of the capacitor j, and q_j is now the charge that flows from its positive node; λ_{Er} is the Lagrangian multiplier for the electrical node r; and λ_{Mu} is the Lagrangian multiplier for the magnetic node u. The number of turns N is defined as the positive or negative number whose absolute value equals the physical number of turns of a winding. The positive value of N means that the winding is wound so that the positive value of its flux ϕ and the positive value of its current $\dot{q}$ satisfies Ampere's right-hand screw rule. Otherwise, N is negative.

The Lagrangian model presented in (3.5) still does not contain energy dissipating components. Therefore, it cannot express the output load and resistors in the circuit. To model these components, we introduce Reighley's dissipation function [15] D as

$$D = \sum_w \frac{1}{2} R_{Ew} \dot{q}_w^{\,2} + \sum_m \frac{1}{2} R_{Mm} \dot{\phi}_m^{\,2}, \tag{3.6}$$

where w is the index of the branches of current paths; R_{Ew} is the energy dissipation coefficient at the branch w, and q_w is the charge that flows through it; and R_{Mm} is the energy dissipation coefficient at the branch m.

Then, the circuit behavior of the model is obtained according to the Euler–Lagrange equation [14] defined as

$$\frac{d}{dt}\left(\frac{\partial L}{\partial \dot{x}}\right) - \frac{\partial L}{\partial x} = -\frac{\partial D}{\partial \dot{x}}, \tag{3.7}$$

where x is any one of the independent variables contained in L or D. With regard to the modeling of the power conversion circuit discussed in this paper, x is any one of charge, flux, or a Lagrangian multiplier.

The first right-hand term of (3.6) indicates the energy dissipation caused by a change of the electric charge, namely the current. Indeed, we can regard R_E as the resistance. On the other hand, the second right-hand term indicates dissipation by the change of the flux. Although these terms represent different types of dissipation, a resistor with resistance R can also be modeled using R_M, for the reason discussed below.

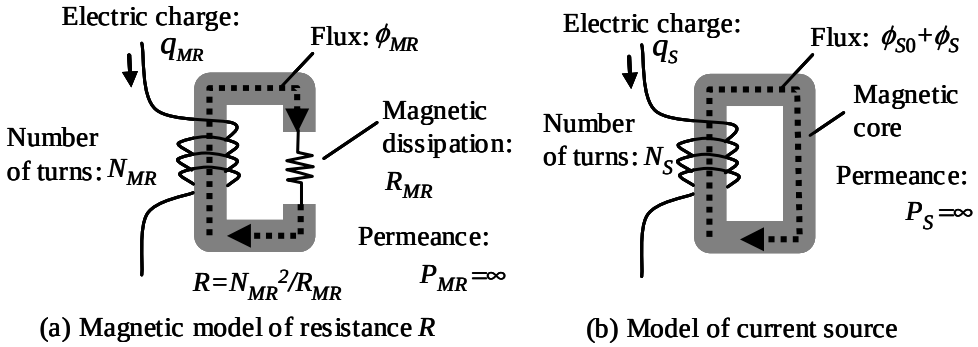

Fig. 3.3. Analytical models of current source and resistance

Consider an imaginary magnetic device illustrated in Fig. 3.3(a). The device has a winding with the number of turns N_{MR} wound on a closed magnetic core with infinite permeance P_{MR} and finite dissipation coefficient R_{MR}. The initial value of the flux ϕ_{MR} is set to zero. Then, the Lagrangian L_{MR} and the dissipation function D_{MR} of the device are obtained as

$$L_{MR} = N_{MR}\dot{q}_{MR}\phi_{MR} - \frac{\phi_{MR}^{\ 2}}{2P_{MR}} \approx N_{MR}\dot{q}_{MR}\phi_{MR}, \tag{3.8}$$

$$D_{MR} = \frac{R_{MR}\dot{\phi}_{MR}^{\ 2}}{2}, \tag{3.9}$$

where q_{MR} is the electric charge that flows through the winding. We can derive the approximation in (3.8) by neglecting $\phi_{MR}^2/2P_{MR}$. The flux ϕ_{MR} is a finite value, because the voltage across the winding, i.e., $N_{MR}\dot{\phi}_{MR}$, is finite and the initial value of ϕ_{MR} is zero. Therefore, $\phi_{MR}^2/2P_{MR}$ is infinitely small and we can approximate the term as zero.

We further consider a circuit with Lagrangian L_A and the dissipation function D_A. We assume that the circuit contains the magnetic device of Fig. 3.3(a). We also consider Lagrangian L'_A and the dissipation function D'_A in which the contribution of the magnetic device is omitted from L_A and D_A. Hence, $L_A = L'_A + L_{MR}$ and $D_A = D'_A + D_{MR}$.

Because the flux ϕ_{MR} is not contained in L'_A and D'_A, we obtain the following equation as a result of applying L_A and D_A to the Euler–Lagrange equation with respect to ϕ_{MR}.

$$N_{MR}\dot{q}_{MR} = R_{MR}\dot{\phi}_{MR}. \tag{3.10}$$

The result shows that the voltage across the windings of the magnetic device is proportional to the current of the winding. Consequently, the magnetic device of Fig. 3.3(a) is equivalent to a resistor with resistance N_{MR}^2/R_{MR}.

As discussed above, resistors can be implemented by electric dissipation expressed by the first right-hand term of (3.6) or by magnetic dissipation expressed by the second right-hand term. In this paper, we allow both expressions.

Equations (3.5) and (3.6) model only a voltage-source converter, because they do not contain a Lagrangian expression for a current source. However, the dual of a voltage-source converter generally contains a current source. Hence, we should extend the Lagrangian expression to model circuits with current sources by adding the Lagrangian of a current source to (3.5). The Lagrangian of a current source is obtained as follows.

It is known that the Lagrangian of a voltage source can be obtained by regarding a voltage source as a capacitor with infinite capacitance[14]. Similarly, the Lagrangian of a current source can be obtained by regarding a current source as an inductor with infinite inductance.

We consider another imaginary magnetic device illustrated in Fig. 3.3(b). The device has a winding with the number of turns N_S and a magnetic path with infinite permeance P_S. Now, we assume that the initial value ϕ_{S0} of the flux in the magnetic core is not zero. If we denote the time-dependent variation of the flux as ϕ_S, the total flux is, therefore, the sum of ϕ_{S0} and ϕ_S. We further denote the initial current of the winding as I. According to Ampere's law, we obtain $\phi_{S0} = N_S I P_S$. Hence, ϕ_{S0} is infinitely large. Then, the Lagrangian L_S of the device is obtained by calculating the first and second terms of the right-hand side of (3.5):

$$L_S = N_S \dot{q}_S \left(\phi_{S0} + \phi_S\right) - \frac{\left(\phi_{S0} + \phi_S\right)^2}{2P_S}. \tag{3.11}$$

Because ϕ_{S0} is infinitely large, we can approximate the above equation by neglecting the second-order of ϕ_S, obtaining (3.12). Note that the Lagrangian is invariant by adding a constant or time derivative of an arbitrary function [16].

$$L_S \approx N_S \dot{q}_S \phi_S - \frac{\phi_{S0}}{P_S}\phi_S = N_S \dot{q}_S \phi_S - N_S I \phi_S. \tag{3.12}$$

If we apply (3.12) to (3.7) with respect to ϕ_S, we obtain $\dot{q}_S = I = const.$. Hence, the Lagrangian L_S certainly expresses the current source. Note that N_S does not affect the behavior of the current source, and therefore, we can assign any arbitrary value to N_S.

Consequently, circuits with current sources have the Lagrangian form of (3.13), which is obtained by merging (3.12) with (3.5).

$$\begin{aligned} L = &\sum_n N_n \dot{q}_n \phi_n - \sum_m \frac{{\phi_m}^2}{2P_m} - \sum_j \frac{\left(Q_j - q_j\right)^2}{2C_j} + \sum_k E_k q_k \\ &- \sum_i N_i I_i \phi_i + \sum_r \lambda_{Er} f_r(q;s) + \sum_u \lambda_{Mu} g_u(\phi), \end{aligned} \tag{3.13}$$

where i is the index of the current sources, N_i is an arbitrary number assigned to the current source i, I_i is its current, and ϕ_i is its imaginary flux. We included the first right-hand term of (3.12) in the first right-hand term of the above equation.

B. Duality Transformation of the Lagrangian Model

The conventional method of duality transformation is based on the interchange between the current and the voltage of every component in the circuit. However, duality transformation interchanges not only the current and the voltage, but also the electric charge and the flux linkage, as noted by S. D. Freeland [1]. Hence, it seems to be also natural to base duality transformation on interchange between the charge and the flux.

There is a useful merit of changing the basis to the interchange between charge and flux from the interchange between current and voltage. The interchange between current and voltage requires a change of the circuit network topology, because Kirchhoff's law imposes different constraints on current and voltage, and the interchange without changing the network generally breaks the law. For this reason, this approach entails a topological transformation.

On the other hand, charge and flux have the same kind of constraints. In particular, the sum of the charge that flows into a node of an electric circuit is required to be zero, and the same stands for the sum of the flux into a node of a magnetic circuit. As a result, the flux and the charge can be interchanged only by regarding an electric network as a magnetic network and a magnetic network as an electric network in principle. Accordingly, this approach does not need a topological transformation. Indeed, the mere interchange of networks results in magnetic circuits with switches, which cannot be realized by a physical circuit. This requires another transformation that moves the switches from magnetic circuits onto electric circuits.

Now, we consider the interchange between the charge and the flux in the Lagrangian dynamics in order to formulate the duality transformation. The charge and the flux are both independent variables in the Lagrangian and dissipation functions. Therefore, renaming the flux as the charge and vice versa suffices to perform the interchange, and the result yields a Lagrangian representing a dynamically equivalent system.

For convenience, we assume that the initial charge in the capacitors is zero. If we rename the charge and the flux in the general forms of Lagrangian and the dissipation function shown in (3.13) and (3.6), we obtain

$$L = \sum_n N_n \dot{\phi}_n q_n - \sum_m \frac{{q_m}^2}{2P_m} - \sum_j \frac{{\phi_j}^2}{2C_j} + \sum_k E_k \phi_k - \sum_i N_i I_i q_i + \sum_r \lambda_{Er} f_r(\phi; s) + \sum_u \lambda_{Mu} g_u(q), \tag{3.14}$$

$$D = \sum_w \frac{1}{2} R_{Ew} \dot{\phi}_w^{\,2} + \sum_m \frac{1}{2} R_{Mm} \dot{q}_m^{\,2}. \tag{3.15}$$

The second, third, fourth, fifth, and seventh right-hand terms of (3.14) have the same form as (3.13). Additionally, (3.15) has already the same form as (3.6). Furthermore, among the elements $f(\phi;s)$ that constitute the sixth right-hand term of (3.14), those that are independent of s can be regarded as the seventh right-hand term of (3.13). Therefore, we can translate (3.14) and (3.15) into a physical circuit, if we successfully convert the

first right-hand term and the switch-dependent elements of the sixth right-hand term of (3.14) into the form of (3.13). Below, we discuss the method for such a conversion.

We add the first right-hand term of (3.14) to the sum of the subset of elements in the sixth right-hand term of (3.14) and denote it as L_F. We assume that L_F includes at least all the switch-dependent elements of the sixth right-hand term. Then, we can express L_F in a matrix form, using the fact that $f(\phi;s)$ is a linear form of ϕ:

$$L_F = \sum_n N_n \dot{\phi}_n q_n + \sum_{r'} \lambda_{Er'} f_{r'}(\phi; s) = \dot{\boldsymbol{\varphi}}^T \mathbf{N}\mathbf{q} + \boldsymbol{\lambda}_E^T \mathbf{Z}\boldsymbol{\varphi}, \tag{3.16}$$

where r' is the index of constraints that are included in the subset, $\boldsymbol{\varphi}$ is the vector of the flux variables defined as $\boldsymbol{\varphi}^T = (\phi_1, \phi_2, \ldots)$, $\mathbf{N}$ is a matrix composed of the numbers of turns, $\mathbf{q}$ is the charge variables defined as $\mathbf{q}^T=(q_1, q_2, \ldots)$, $\boldsymbol{\lambda}_E$ is the vector of Lagrangian multipliers defined as $\boldsymbol{\lambda}_E{}^T=(\lambda_{E1}, \lambda_{E2}, \ldots)$, and $\mathbf{Z}$ is a matrix whose elements are functions of the state variable s or constant integers that take any one of +1, 0, or −1.

We replace each Lagrangian multiplier $\lambda_{Er'}$ by the time-derivative of an additionally introduced imaginary charge $q_{\lambda r'}$ multiplied by an additionally introduced imaginary number of turns $N_{\lambda r'}$. $N_{\lambda r'}$ is a constant value and we can assign any arbitrary integer to $N_{\lambda r'}$. We assume that the initial value of $q_{\lambda r'}$ is zero for convenience. Because the initial values of fluxes are given so that the initial value of $f(\phi;s)$ equals zero, the result of replacement is equivalent to the original, as shown in the appendix. This technique is based on a well-known method [17] for eliminating a cyclic coordinate from the Lagrangian. Then, we obtain

$$L_F = \dot{\boldsymbol{\varphi}}^T \mathbf{N}\mathbf{q} + \dot{\mathbf{f}}_\lambda^T \mathbf{Z}\boldsymbol{\varphi}, \tag{3.17}$$

where $\mathbf{f}_\lambda$ is the vector defined as $\mathbf{f}_\lambda{}^T=(N_{\lambda 1}q_{\lambda 1}, N_{\lambda 2}q_{\lambda 2}, \ldots)$.

Because the Lagrangian is invariant by adding the time derivative of an arbitrary function, we can develop (3.17) as

$$L_F = \dot{\boldsymbol{\varphi}}^T \mathbf{N}\mathbf{q} + \frac{d}{dt}\left(\mathbf{f}_\lambda^T \mathbf{Z}\boldsymbol{\varphi}\right) - \dot{\boldsymbol{\varphi}}^T \mathbf{Z}^T \mathbf{f}_\lambda = \dot{\boldsymbol{\varphi}}^T \left(\mathbf{N}\mathbf{q} - \mathbf{Z}^T \mathbf{f}_\lambda\right). \tag{3.18}$$

We further introduce additional imaginary number of turns N'_λ, additional imaginary charges q'_λ, and additional Lagrangian multipliers λ'_E. Again, we can assign any arbitrary constant integers to N'_λ and we assume that the initial value of q'_λ equals zero. We introduce the constraint that $\mathbf{f}'_\lambda = \mathbf{N}\mathbf{q} - \mathbf{Z}^T\mathbf{f}_\lambda$, where $\mathbf{f}'_\lambda$ is a vector defined as $\mathbf{f}'_\lambda{}^T = (N'_{\lambda 1}q'_{\lambda 1}, N'_{\lambda 2}q'_{\lambda 2}, \ldots)$. Then, we can express the Lagrangian L_F by the equivalent expression

$$\begin{aligned} L_F &= \dot{\boldsymbol{\varphi}}^T \mathbf{f}'_\lambda + \boldsymbol{\lambda}'^T_E \left(\mathbf{f}'_\lambda - \mathbf{N}\mathbf{q} + \mathbf{Z}^T \mathbf{f}_\lambda\right) \\ &= \frac{d}{dt}\left(\boldsymbol{\varphi}^T \mathbf{f}'_\lambda\right) - \boldsymbol{\varphi}^T \dot{\mathbf{f}}'_\lambda + \boldsymbol{\lambda}'^T_E \left(\mathbf{f}'_\lambda - \mathbf{N}\mathbf{q} + \mathbf{Z}^T \mathbf{f}_\lambda\right) \\ &= -\boldsymbol{\varphi}^T \dot{\mathbf{f}}'_\lambda + \boldsymbol{\lambda}'^T_E \left(\mathbf{f}'_\lambda - \mathbf{N}\mathbf{q} + \mathbf{Z}^T \mathbf{f}_\lambda\right), \end{aligned} \tag{3.19}$$

where $\boldsymbol{\lambda}'_E$ is a vector defined as $\boldsymbol{\lambda}'^T_E=(\lambda'_{E1}, \lambda'_{E2}, \ldots)$.

For convenience, we rewrite (3.19) in the summation form. Then, we have

$$L_F = -\sum_{\alpha} N'_{\lambda\alpha}\dot{q}'_{\lambda\alpha}\phi_\alpha + \sum_{\alpha}\lambda'_{E\alpha}\left(N'_{\lambda\alpha}q'_{\lambda\alpha} - \sum_{\beta} n_{\alpha\beta}q_\beta + \sum_{r'} z_{r'\alpha}N_{\lambda r'}q_{\lambda r'}\right), \tag{3.20}$$

where α is the index of the flux variables in (3.14) (i.e., the charge variables in the original Lagrangian (3.13)), β is the index of the charge variables in (3.14) (i.e., the flux variables in the original Lagrangian (3.13)), $n_{\alpha\beta}$ is the element of **N**, and $z_{r'\alpha}$ is the element of **Z**.

First, we consider a fortunate case in which all $n_{\alpha\beta}$ are any one of $+A$, 0, or $-A$, where A is an arbitrary positive integer. Then, (3.20) results in the same form as the first and sixth right-hand terms of (3.13) because we can set $N'_{\lambda\alpha}$ and $N_{\lambda r'}$ to $-A$ or A. For example, if we set all $N'_{\lambda\alpha}$ and $N_{\lambda r'}$ to A, we have

$$\begin{aligned} L_F &= -\sum_{\alpha} N'_{\lambda\alpha}\dot{q}'_{\lambda\alpha}\phi_\alpha + \sum_{\alpha}\lambda'_{E\alpha}A\left(q'_{\lambda\alpha} - \sum_{\beta}\zeta_{\alpha\beta}q_\beta + \sum_{r'} z_{r'\alpha}q_{\lambda r'}\right) \\ &= -\sum_{\alpha} N'_{\lambda\alpha}\dot{q}'_{\lambda\alpha}\phi_\alpha + \sum_{\alpha}\lambda''_{E\alpha}\left(q'_{\lambda\alpha} - \sum_{\beta}\zeta_{\alpha\beta}q_\beta + \sum_{r'} z_{r'\alpha}q_{\lambda r'}\right), \end{aligned} \tag{3.21}$$

where $\zeta_{\alpha\beta}= n_{\alpha\beta}/A$, and $\lambda''_{E\alpha}$ are Lagrangian multipliers defined as $\lambda''_{E\alpha}= \lambda'_{E\alpha}A$.

Note that $\zeta_{\alpha\beta}$ and $z_{r'\alpha}$ take any one of +1, 0, or −1. Therefore, (3.21) indicates that the first and sixth right-hand terms of (3.14) are successfully transformed into the form of (3.13).

The above discussion is based on a specific case. However, even in the other cases, we can transform L_F into the form of (3.13).

Second, we consider a case in which all $n_{\alpha\beta}$ are any one of $+A$, 0, or $-A$ except one element $n_{\alpha'\beta'}$. In this case, we further introduce an additional imaginary charge q'_κ and an additional Lagrangian multiplier λ_κ. Then, we have

$$\begin{aligned} L_F &= -\sum_{\alpha} N'_{\lambda\alpha}\dot{q}'_{\lambda\alpha}\phi_\alpha + \sum_{\alpha\neq\alpha'}\lambda''_{E\alpha}\left(q'_{\lambda\alpha} - \sum_{\beta}\zeta_{\alpha\beta}q_\beta + \sum_{r'} z_{r'\alpha}q_{\lambda r'}\right) \\ &\quad + \lambda''_{E\alpha'}\left(q'_{\lambda\alpha'} - \sum_{\beta\neq\beta'}\zeta_{\alpha'\beta}q_\beta + \sum_{r'} z_{r'\alpha'}q_{\lambda r'}\right) - \lambda''_{E\alpha'}\frac{n_{\alpha'\beta'}}{A}q_{\beta'} \\ &= -\sum_{\alpha} N'_{\lambda\alpha}\dot{q}'_{\lambda\alpha}\phi_\alpha + \sum_{\alpha\neq\alpha'}\lambda''_{E\alpha}\left(q'_{\lambda\alpha} - \sum_{\beta}\zeta_{\alpha\beta}q_\beta + \sum_{r'} z_{r'\alpha}q_{\lambda r'}\right) \\ &\quad + \lambda''_{E\alpha'}\left(q'_{\lambda\alpha'} - \sum_{\beta\neq\beta'}\zeta_{\alpha'\beta}q_\beta + \sum_{r'} z_{r'\alpha'}q_{\lambda r'} - q'_\kappa\right) + \lambda_\kappa\left(n_{\alpha'\beta'}q_{\beta'} - Aq'_\kappa\right). \end{aligned} \tag{3.22}$$

We replace the Lagrangian multiplier λ_κ by the time-derivative of an additional imaginary flux ϕ_κ. The result of replacement is equivalent to the original, as shown in the appendix. (We regard the flux ϕ as the charge q, and q_λ as ϕ_κ in the appendix.) As a result, we obtain

$$
\begin{aligned}
L_F &= -\sum_\alpha N'_{\lambda\alpha}\dot{q}'_{\lambda\alpha}\phi_\alpha + \sum_{\alpha\neq\alpha'}\lambda''_{E\alpha}\left(q'_{\lambda\alpha} - \sum_\beta \zeta_{\alpha\beta}q_\beta + \sum_{r'} z_{r'\alpha}q_{\lambda r'}\right) \\
&\quad + \lambda''_{E\alpha'}\left(q'_{\lambda\alpha'} - \sum_{\beta\neq\beta'}\zeta_{\alpha'\beta}q_\beta + \sum_{r'} z_{r'\alpha'}q_{\lambda r'} - q'_\kappa\right) + \dot{\phi}_\kappa\left(n_{\alpha'\beta'}q_{\beta'} - Aq'_\kappa\right) \\
&= -\sum_\alpha N'_{\lambda\alpha}\dot{q}'_{\lambda\alpha}\phi_\alpha + \sum_{\alpha\neq\alpha'}\lambda''_{E\alpha}\left(q'_{\lambda\alpha} - \sum_\beta \zeta_{\alpha\beta}q_\beta + \sum_{r'} z_{r'\alpha}q_{\lambda r'}\right) \\
&\quad + \lambda''_{E\alpha'}\left(q'_{\lambda\alpha'} - \sum_{\beta\neq\beta'}\zeta_{\alpha'\beta}q_\beta + \sum_{r'} z_{r'\alpha'}q_{\lambda r'} - q'_\kappa\right) \\
&\quad + \frac{d}{dt}\left\{\phi_\kappa\left(n_{\alpha'\beta'}q_{\beta'} - Aq'_\kappa\right)\right\} - n_{\alpha'\beta'}\dot{q}_{\beta'}\phi_\kappa + A\dot{q}'_\kappa\phi_\kappa \\
&= -\sum_\alpha N'_{\lambda\alpha}\dot{q}'_{\lambda\alpha}\phi_\alpha + \sum_{\alpha\neq\alpha'}\lambda''_{E\alpha}\left(q'_{\lambda\alpha} - \sum_\beta \zeta_{\alpha\beta}q_\beta + \sum_{r'} z_{r'\alpha}q_{\lambda r'}\right) \\
&\quad + \lambda''_{E\alpha'}\left(q'_{\lambda\alpha'} - \sum_{\beta\neq\beta'}\zeta_{\alpha'\beta}q_\beta + \sum_{r'} z_{r'\alpha'}q_{\lambda r'} - q'_\kappa\right) - n_{\alpha'\beta'}\dot{q}_{\beta'}\phi_\kappa + A\dot{q}'_\kappa\phi_\kappa .
\end{aligned}
\tag{3.23}
$$

Equation (3.23) has the same form as the first and sixth right-hand terms of (3.13). Even if there is more than one element not following the relation that requires $n_{\alpha\beta}$ to be any one of $+A$, 0, or $-A$, we can transform L_F into the form of (3.13) in a similar manner to (3.22) and (3.23). Therefore, we can generally transform L_F into the form of (3.13). Consequently, (3.14) and (3.15) can be generally converted into the form of (3.13) and (3.6) according to the abovementioned procedure.

It is worth noting that (3.14) and (3.15) can be converted into multiple equivalent expressions in the form of (3.13) and (3.6) because one resultant expression can yield other equivalent expressions in the form of (3.13) and (3.6). This indicates that we can obtain multiple duals by translating these equivalent Lagrangian expressions into circuit topologies.

For example, we can replace the Lagrangian multiplier for an arbitrary electric node with the time-derivative of an additionally introduced imaginary charge multiplied by an additionally introduced imaginary number of turns. This replacement yields another equivalent Lagrangian in the form of (3.13) as shown below.

Let L_{mult} be a Lagrangian multiplier term of an electrical node. According to (3.3), L_{mult} have the following general form:

$$L_{mult} = \lambda\left(z_1(s)q_1 + z_2(s)q_2 + \cdots\right), \tag{3.24}$$

where λ is a Lagrangian multiplier.

Introducing an additionally imaginary flux ϕ and an additionally imaginary number of turns N, we can obtain another equivalent expression for L_{mult}:

$$\begin{aligned} L_{mult} &= N\dot{\phi}\left(z_1(s)q_1 + z_2(s)q_2 \cdots\right) \\ &= -Nz_1(s)\dot{q}_1\phi - Nz_2(s)\dot{q}_2\phi \cdots + \frac{d}{dt}\left\{Nz_1(s)q_1\phi + Nz_2(s)q_2\phi \cdots\right\} \\ &= -Nz_1(s)\dot{q}_1\phi - Nz_2(s)\dot{q}_2\phi \cdots . \end{aligned} \tag{3.25}$$

The terms independent of s in the right-most side of (3.25) already have the form of the first right-hand term in (3.13). However, even if there are terms dependent on s, we can convert L_{mult} into the form of (3.13). For example, let $Nz_i(s)\dot{q}_i\phi$ be the only term dependent on s. Further introducing an additional charge q_ω and an additional Lagrangian multiplier λ_ω, we obtain an equivalent expression

$$L_{mult} = -Nz_1\dot{q}_1\phi - Nz_2\dot{q}_2\phi - \cdots - N\dot{q}_\omega\phi - Nz_{i+1}\dot{q}_{i+1}\phi \cdots + \lambda_\omega\left(q_\omega - z_i(s)q_i\right). \tag{3.26}$$

Even if there is more than one term dependent on s, we can transform L_{mult} into the form of (3.13) in a similar manner to (3.26). Consequently, we can generally obtain another equivalent Lagrangian in the form of (3.13) by replacing the Lagrangian multiplier term of an electrical node.

In addition, we can obtain another simpler equivalent Lagrangian in the form of (3.13), if a resultant Lagrangian expression is reducible. For example, if the i-th element ϕ_i of the flux vector $\boldsymbol{\varphi}$ in (3.19) is not contained anywhere in the resultant Lagrangian and the resultant dissipation function except the terms originating from L_F, we obtain that $N'_{\lambda i}q'_{\lambda i}$ = const. as a result of the Euler–Lagrange equation of the resultant Lagrangian and dissipation function with respect to ϕ_i. This indicates that $q'_{\lambda i} = 0$ because the initial value of $q'_{\lambda i}$ is zero. Hence, we can eliminate $q'_{\lambda i}$ and ϕ_i by substituting $q'_{\lambda i} = 0$ into the resultant Lagrangian.

In addition, we can eliminate the Lagrangian multiplier terms for magnetic nodes in the resultant Lagrangian. The terms are originally the switch-independent constraints among $f(\phi,s)$ in (3.14). Additionally, they represent the magnetic network of a magnetic circuit. Therefore, direct translation of the resultant Lagrangian yields a dual with integrated magnetic components. In this case, we can reduce the Lagrangian into another that corresponds to a dual without integrated magnetic components by utilizing the technique proposed in the previous work [14].

C. Composing a Dual Circuit Topology

The previous subsection obtained the Lagrangian and dissipation functions of a dual by interchanging the charge and the flux. As we have seen, these Lagrangian and

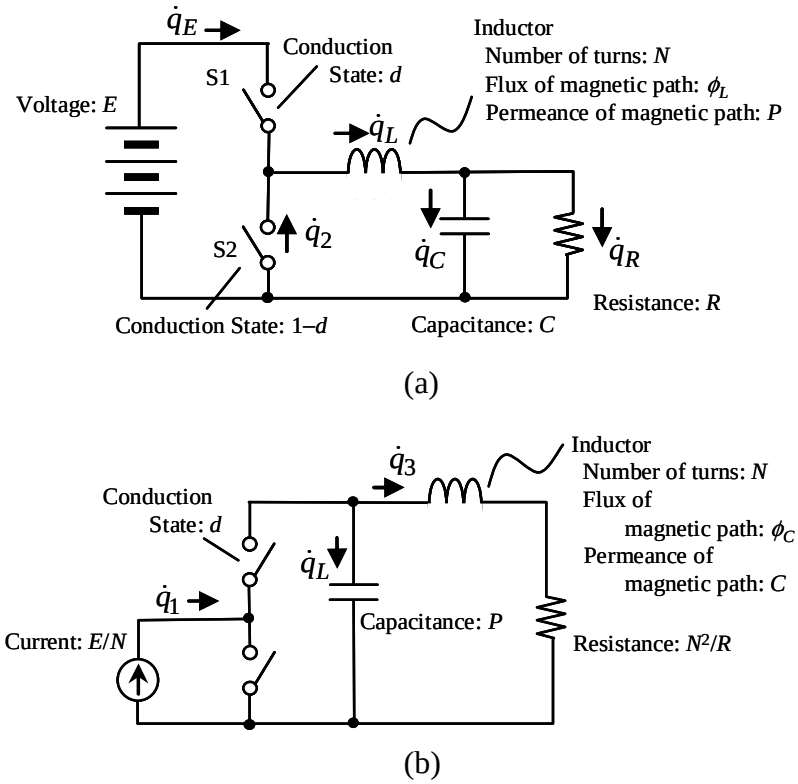

Fig. 3.4. Analytical models of voltage-source buck chopper and its dual. (a) Voltage source buck chopper. (b) Dual chopper.

dissipation functions can be obtained in the form of (3.13) and (3.6). In this subsection, we discuss the method to compose the physical circuit topology of the dual from these resultant Lagrangian and dissipation functions.

As discussed in the previous work [14], each term of (3.13) and (3.6) has a correspondence relation with a component of a physical circuit topology. Therefore, we can configure the topology utilizing this relationship. The following are the steps to configure the topology:

1. Configure electric and magnetic networks from constraints at the nodes. These constraints are represented by the sixth and seventh right-hand terms of (3.13). Place switches on the electric network so that this network is consistent with the constraints.
2. Place windings on the electric network so that they interlink with the magnetic network as represented by the first right-hand term of (3.13).
3. Place permeance on the magnetic network as represented by the second right-hand term of (3.13).
4. Place infinitely large permeance with infinitely large initial flux on the magnetic network as represented by the fifth right-hand term of (3.13). Find structures shown in Fig. 3.3(b), and replace them with current sources.
5. Place capacitors and voltage sources on the electric network as represented by the third and fourth right-hand terms of (3.13), respectively.

6. Place resistors on the electric network as represented by the first right-hand term of (3.6).
7. Place magnetic dissipation on the magnetic network as represented by the second right-hand term of (3.6). Find the structures shown in Fig. 3.3(a), and replace them with resistors.

(If there is a magnetic path without any permeance or magnetic dissipation, we consider the path to have infinitely large permeance.)

3. 3. Examples of Duality Transformation

A. Buck Chopper

Figure 4.4(a) illustrates a voltage-source buck chopper. Because its circuit topology is planar, we easily obtain the dual chopper illustrated in Fig. 4.4(b) according to the conventional method [1]. The purpose of this subsection is to confirm that the same dual results from the proposed method.

First, we translate Fig. 4.4(a) into Lagrangian L and the dissipation function D according to the method of Lagrangian modeling [14].

$$L = N\dot{q}_L\phi_L - \frac{{\phi_L}^2}{2P} - \frac{{q_C}^2}{2C} + Eq_E + \lambda_1(q_E - dq_L) + \lambda_2\{q_2 - (1-d)q_L\} + \lambda_3(q_L - q_C - q_R), \tag{3.27}$$

$$D = \frac{1}{2}R{\dot{q}_R}^2, \tag{3.28}$$

where d is the variable that indicates the on-state and the off-sate of switch S1. If S1 is in the on-state, then $d = 1$. If S1 is in the off-state, then $d = 0$. We assume that the initial value of all charge is zero.

The charge q_2 appears only in the sixth right-hand term of (3.27). Because (3.7) with respect to q_2 results in $\lambda_2 = 0$, the term with λ_2 does not affect the circuit behavior. Hence, we eliminate the term in the following discussion.

Now, we rename the charge as the flux and the flux as the charge in (3.27) and (3.28), obtaining the Lagrangian L' and the dissipation function D' as

$$L' = N\dot{\phi}_L q_L - \frac{{q_L}^2}{2P} - \frac{{\phi_C}^2}{2C} + E\phi_E + \lambda_1(\phi_E - d\phi_L) + \lambda_3(\phi_L - \phi_C - \phi_R). \tag{3.29}$$

$$D' = \frac{1}{2}R{\dot{\phi}_R}^2. \tag{3.30}$$

Next, we introduce additional electric charges q_1 and q_3 and replace the Lagrangian multipliers λ_1 and λ_3 with $-N\dot{q}_1$ and $-N\dot{q}_3$ in the same manner as (3.17) and (3.18). (Because the number of turns that appears in the Lagrangian (3.27) is only N, we can set

$N\lambda_1$, $N\lambda_2$, … and $N'\lambda_1$, $N'\lambda_2$, … to N or $-N$.) We denote the sum of the first, fifth, and sixth right-hand terms of (3.29) as L_{tmp}. Then, we have

$$\begin{aligned} L_{tmp} &= N\dot{\phi}_L q_L - N\dot{q}_1(\phi_E - d\phi_L) - N\dot{q}_3(\phi_L - \phi_C - \phi_R) \\ &= N\dot{\phi}_E q_1 - N\dot{\phi}_C q_3 - N\dot{\phi}_R q_3 + N\dot{\phi}_L(q_L - dq_1 + q_3). \end{aligned} \tag{3.31}$$

Then, we introduce additional charge variables q'_E, q'_C, q'_R, and q'_L and additional Lagrangian multipliers λ'_E, λ'_C, λ'_R, and λ'_L. We develop (3.31) in the similar manner as (3.19)–(3.21), obtaining

$$\begin{aligned} L_{tmp} &= N\dot{\phi}_E q'_E + \lambda'_E(q'_E - q_1) - N\dot{\phi}_C q'_C + \lambda'_C(q'_C - q_3) \\ &\quad - N\dot{\phi}_R q'_R + \lambda'_R(q'_R - q_3) + N\dot{\phi}_L q'_L + \lambda'_L(q'_L - q_L + dq_1 - q_3) \\ &= -N\dot{q}'_E\phi_E + \lambda'_E(q'_E - q_1) + N\dot{q}'_C\phi_C + \lambda'_C(q'_C - q_3) \\ &\quad + N\dot{q}'_R\phi_R + \lambda'_R(q'_R - q_3) - N\dot{q}'_L\phi_L + \lambda'_L(q'_L - q_L + dq_1 - q_3). \end{aligned} \tag{3.32}$$

The Lagrangian multipliers λ'_E, λ'_C, and λ'_R represent obvious relations that $q'_E = q_1$ and $q'_C = q'_R = q_3$. Therefore, we eliminate λ'_E, λ'_C, and λ'_R by substituting the relations into (3.32):

$$L_{tmp} = -N\dot{q}_1\phi_E + N\dot{q}_3\phi_C + N\dot{q}_3\phi_R - N\dot{q}'_L\phi_L + \lambda'_L(q'_L - q_L + dq_1 - q_3). \tag{3.33}$$

Replacing the first, fifth, and sixth terms of (3.29) by (3.33), we have

$$\begin{aligned} L' &= -N\dot{q}_1\phi_E + E\phi_E - \frac{{q_L}^2}{2P} + N\dot{q}_3\phi_C - \frac{{\phi_C}^2}{2C} + N\dot{q}_3\phi_R \\ &\quad - N\dot{q}'_L\phi_L + \lambda'_L(q'_L - q_L + dq_1 - q_3). \end{aligned} \tag{3.34}$$

Note that ϕ_L appears only in the seventh right-hand term of L'. Hence, the Euler–Lagrange equation (3.7) of L' and D' with respect to ϕ_L yields $Nq'_L = \text{const}$. This indicates that $q'_L = 0$ because the initial value of q'_L is zero. Finally, we can simplify L' by substituting $q'_L = 0$ into (3.34), obtaining

$$L' = -N\dot{q}_1\phi_E + E\phi_E - \frac{{q_L}^2}{2P} + N\dot{q}_3\phi_C - \frac{{\phi_C}^2}{2C} + N\dot{q}_3\phi_R - \lambda'_L(q_L - dq_1 + q_3). \tag{3.35}$$

Equations (3.35) and (3.30) represent the physical circuit illustrated in Fig. 3.4(b). The result shows that the proposed method also derives Fig. 3.4(b) as the dual corresponding to Fig. 3.4(a).

B. Three Phase Inverter

This subsection derives the duals shown in Fig. 3.1(b) and Fig. 3.1(c) from the original circuit shown in Fig. 3.1(a). We translate Fig. 3.1(a) into the Lagrangian L and dissipation function D, obtaining (3.36) and (3.37). We define the circuit parameters, charge, and fluxes as illustrated in Fig. 3.5(a).

$$\begin{aligned} L = {} & N\dot{q}_1\phi_1 + N\dot{q}_2\phi_2 + N\dot{q}_3\phi_3 + Eq_E - \frac{\phi_1^{\,2}}{2P} - \frac{\phi_2^{\,2}}{2P} - \frac{\phi_3^{\,2}}{2P} \\ & + \lambda_1\{q_E - d_1(q_1 - q_3) - d_2(q_2 - q_1) - d_3(q_3 - q_2)\} \\ & + \lambda_2\{q_E - (1-d_1)(q_1 - q_3) - (1-d_2)(q_2 - q_1) - (1-d_3)(q_3 - q_2)\}, \end{aligned} \tag{3.36}$$

$$D = \frac{1}{2}R\left(\dot{q}_1^{\,2} + \dot{q}_2^{\,2} + \dot{q}_3^{\,2}\right), \tag{3.37}$$

where d_1, d_2, and d_3 are the variables that indicate the on-state and off-state of switches S1, S2, and S3, respectively. If the switches are in the on-state, the variable equals 1. If the switches are in the off-state, the variable equals zero.

The constraint represented by the term with λ_2 is the same as that with λ_1. Hence, we can eliminate the term with λ_2. Then, we rename the charge as the flux and the flux as the charge in (3.36) and (3.37), obtaining

$$\begin{aligned} L' = {} & N\dot{\phi}_1 q_1 + N\dot{\phi}_2 q_2 + N\dot{\phi}_3 q_3 + E\phi_E - \frac{q_1^{\,2}}{2P} - \frac{q_2^{\,2}}{2P} - \frac{q_3^{\,2}}{2P} \\ & + \lambda_1\{\phi_E - (d_1 - d_2)\phi_1 - (d_2 - d_3)\phi_2 - (d_3 - d_1)\phi_3\}, \end{aligned} \tag{3.38}$$

$$D' = \frac{1}{2}R\left(\dot{\phi}_1^{\,2} + \dot{\phi}_2^{\,2} + \dot{\phi}_3^{\,2}\right). \tag{3.39}$$

Next, we introduce additional charge q_λ and replace the Lagrangian multiplier λ_1 by $-N\dot{q}_\lambda$. (Because the number of turns that appears in the Lagrangian (3.38) is only N, we can set $N_{\lambda 1}$, $N_{\lambda 2}$, … and $N'_{\lambda 1}$, $N'_{\lambda 2}$, … to N or $-N$.) Again, we assume that the initial value of q_λ is zero. We denote the sum of the first, second, third, and eighth right-hand terms of (3.38) as L_{tmp2}. Then, we develop L_{tmp2} in the same manner as (3.17) and (3.18):

$$\begin{aligned} L_{tmp2} = {} & N\dot{\phi}_1 q_1 + N\dot{\phi}_2 q_2 + N\dot{\phi}_3 q_3 \\ & - N\dot{q}_\lambda\{\phi_E - (d_1 - d_2)\phi_1 - (d_2 - d_3)\phi_2 - (d_3 - d_1)\phi_3\} \\ = {} & Nq_\lambda\dot{\phi}_E - N\dot{\phi}_1\{(d_1 - d_2)q_\lambda - q_1\} - N\dot{\phi}_2\{(d_2 - d_3)q_\lambda - q_2\} \end{aligned}$$

$$-N\dot{\phi}_3\{(d_3-d_1)q_\lambda - q_3\}. \tag{3.40}$$

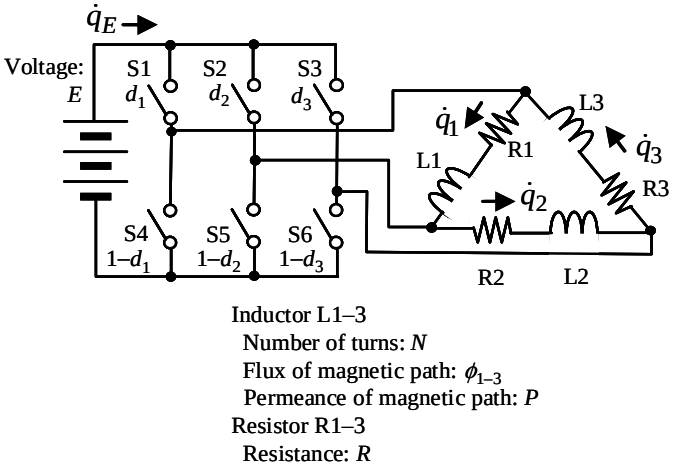

(a) Voltage source inverter

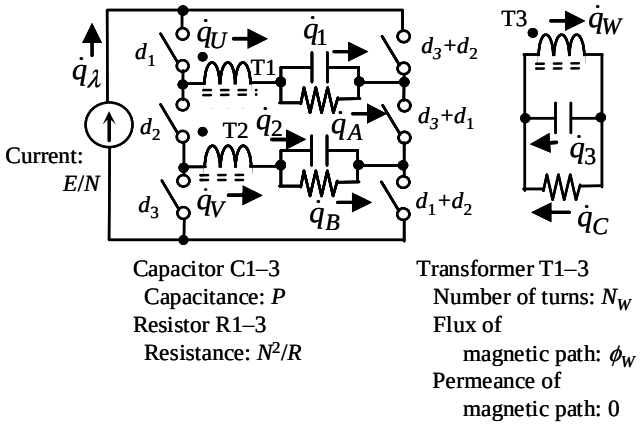

(b) Dual inverter A

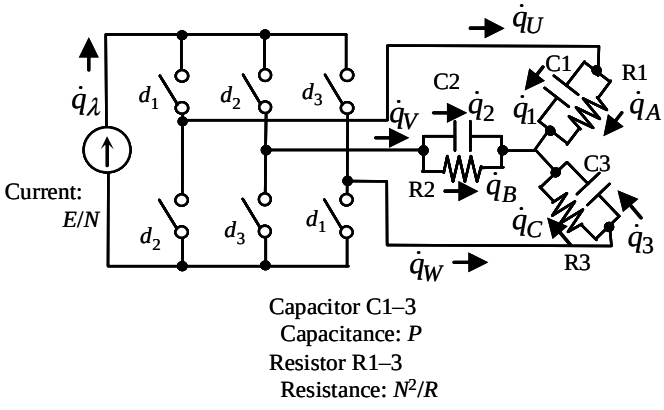

(c) Dual inverter B

Fig. 3.5. Analytical model of the three-phase voltage source inverter and its duals.

Then, we introduce additional charges q_E, q_A, q_B, and q_C and additional Lagrangian multipliers λ_E, λ_A, λ_B, and λ_C. Developing (3.40) in a similar manner as (3.19)–(3.21), we obtain

$$\begin{aligned} L_{tmp2} &= Nq_E\dot{\phi}_E + \lambda_E(q_E - q_\lambda) - Nq_A\dot{\phi}_1 - Nq_B\dot{\phi}_2 - Nq_C\dot{\phi}_3 \\ &\quad + \lambda_A\{q_A - (d_1 - d_2)q_\lambda + q_1\} + \lambda_B\{q_B - (d_2 - d_3)q_\lambda + q_2\} \\ &\quad + \lambda_C\{q_C - (d_3 - d_1)q_\lambda + q_3\} \\ &= -N\dot{q}_E\phi_E + \lambda_E(q_E - q_\lambda) + N\dot{q}_A\phi_1 + N\dot{q}_B\phi_2 + N\dot{q}_C\phi_3 \\ &\quad + \lambda_A\{q_A - (d_1 - d_2)q_\lambda + q_1\} + \lambda_B\{q_B - (d_2 - d_3)q_\lambda + q_2\} \\ &\quad + \lambda_C\{q_C - (d_3 - d_1)q_\lambda + q_3\}. \end{aligned} \tag{3.41}$$

The Lagrangian multiplier λ_E represents an obvious relation that $q_E = q_\lambda$. Thus, we substitute the relation into (3.41) to eliminate λ_E. In addition, with a view to helping the translation of (3.41) into a physical circuit, we additionally introduce the charge q_U, q_V, and q_W:

$$q_U = (d_1 - d_2)q_\lambda, \tag{3.42}$$

$$q_V = (d_2 - d_3)q_\lambda, \tag{3.43}$$

$$q_W = (d_3 - d_1)q_\lambda. \tag{3.44}$$

At the same time, we introduce additional Lagrangian multipliers λ_U, λ_V, and λ_W to introduce additional constraints (3.42)–(3.44) into (3.41). Then, we can rewrite (3.41) as

$$\begin{aligned} L_{tmp2} &= -N\dot{q}_\lambda\phi_E + N\dot{q}_A\phi_1 + N\dot{q}_B\phi_2 + N\dot{q}_C\phi_3 \\ &\quad + \lambda_A(q_A - q_U + q_1) + \lambda_B(q_B - q_V + q_2) \\ &\quad + \lambda_C(q_C - q_W + q_3) + \lambda_U\{q_U - (d_1 - d_2)q_\lambda\} \\ &\quad + \lambda_V\{q_V - (d_2 - d_3)q_\lambda\} + \lambda_W\{q_W - (d_3 - d_1)q_\lambda\}. \end{aligned} \tag{3.45}$$

Replacing the first, second, third, and eighth terms of (3.38) by (3.45), we obtain

$$\begin{aligned} L' &= -N\dot{q}_\lambda\phi_E + E\phi_E + N\dot{q}_A\phi_1 + N\dot{q}_B\phi_2 + N\dot{q}_C\phi_3 - \frac{q_1^2}{2P} - \frac{q_2^2}{2P} - \frac{q_3^2}{2P} \\ &\quad + \lambda_B(q_B - q_V + q_2) + \lambda_C(q_C - q_W + q_3) + \lambda_A(q_A - q_U + q_1) \\ &\quad + \lambda_U\{q_U - (d_1 - d_2)q_\lambda\} + \lambda_V\{q_V - (d_2 - d_3)q_\lambda\} + \lambda_W\{q_W - (d_3 - d_1)q_\lambda\}. \end{aligned} \tag{3.46}$$

Note that we always have the relation $q_U + q_V + q_W = 0$ from the definition and that the value of $d_1 - d_2$, $d_2 - d_3$, and $d_3 - d_1$ is one of 1, 0, or −1. Consequently, we can translate the Lagrangian (3.46) and the dissipation function (3.39) into the dual circuit illustrated in Fig. 3.5(c).

In order to derive another dual, we adopt the constraint $q_U + q_V + q_W = 0$ instead of $q_W = (d_3 - d_1)q_\lambda$ implemented by the term with λ_W in (3.46). This does not affect the system, because we can derive $q_W = (d_3 - d_1)q_\lambda$ from the newly introduced constraint $q_U + q_V + q_W = 0$ and the constraints already implemented by the terms with λ_U and λ_V. By rewriting the constraint term, we obtain (3.47), which is equivalent to (3.46):

$$\begin{aligned} L' = &-N\dot{q}_\lambda\phi_E + E\phi_E + N\dot{q}_A\phi_1 + N\dot{q}_B\phi_2 + N\dot{q}_C\phi_3 - \frac{q_1^{\,2}}{2P} - \frac{q_2^{\,2}}{2P} - \frac{q_3^{\,2}}{2P} \\ &+ \lambda_A(q_A - q_U + q_1) + \lambda_B(q_B - q_V + q_2) + \lambda_C(q_C - q_W + q_3) \\ &+ \lambda_U\{q_U - (d_1 - d_2)q_\lambda\} + \lambda_V\{q_V - (d_2 - d_3)q_\lambda\} \\ &+ \lambda_W(q_U + q_V + q_W). \end{aligned} \tag{3.47}$$

Now, we introduce an additional flux ϕ_W and an additional number of turns N_W. According to the similar process as in (3.24) and (3.25), we can replace the Lagrangian multiplier λ_W with $N_W\dot{\phi}_W$ to obtain an equivalent Lagrangian:

$$\begin{aligned} L' = &-N\dot{q}_\lambda\phi_E + E\phi_E + N\dot{q}_A\phi_1 + N\dot{q}_B\phi_2 + N\dot{q}_C\phi_3 - \frac{q_1^{\,2}}{2P} - \frac{q_2^{\,2}}{2P} - \frac{q_3^{\,2}}{2P} \\ &+ \lambda_A(q_A - q_U + q_1) + \lambda_B(q_B - q_V + q_2) + \lambda_C(q_C - q_W + q_3) \\ &+ \lambda_U\{q_U - (d_1 - d_2)q_\lambda\} + \lambda_V\{q_V - (d_2 - d_3)q_\lambda\} + N_W\dot{\phi}_W(q_U + q_V + q_W) \\ = &-N\dot{q}_\lambda\phi_E + E\phi_E + N\dot{q}_A\phi_1 + N\dot{q}_B\phi_2 + N\dot{q}_C\phi_3 - \frac{q_1^{\,2}}{2P} - \frac{q_2^{\,2}}{2P} - \frac{q_3^{\,2}}{2P} \\ &+ \lambda_A(q_A - q_U + q_1) + \lambda_B(q_B - q_V + q_2) + \lambda_C(q_C - q_W + q_3) \\ &+ \lambda_U\{q_U - (d_1 - d_2)q_\lambda\} + \lambda_V\{q_V - (d_2 - d_3)q_\lambda\} - N_W\phi_W(\dot{q}_U + \dot{q}_V + \dot{q}_W). \end{aligned} \tag{3.48}$$

Translating (3.48) and (3.39) into a physical circuit yields the dual illustrated in Fig. 3.5(b).

This result shows that the proposed method derives both of the duals presented in Fig. 3.1(b) and Fig. 3.1(c).

3. 4. Conclusions

The duality principle is one of the basic features that many power converters exhibit, and has been widely utilized in power electronics research. When utilizing the principle, we generally need to perform duality transformation, which derives the dual circuit from an original circuit. Although methods of duality transformation have been proposed in previous studies, they sometimes lead to different duals when applied to non-planar circuits. Moreover, the dual derived by one method is not necessarily derived by another. This seems to hinder systematic derivation of the duals of non-planar circuits, because we have to choose an appropriate method to obtain the desired dual.

As a probable candidate of a universal and systematic method that derives all possible duals, this paper proposes a novel method for duality transformation. The proposed method employs Lagrangian dynamics as the basis, whereas the conventional methods are based on topological transformation. Because the proposed method does not need a topological transformation, it is applicable to non-planar circuits in the same manner as to planar circuits. Thus, it probably avoids the abovementioned problem, which seems to be related to the difficulty in applying topological transformations to non-planar circuits.

In order to verify the proposed method, we presented two examples of duality transformation: One is the buck chopper, and the other is the three-phase inverter. Particularly, the latter is a representative non-planar circuit, from which the conventional methods lead to either one of two different duals. The proposed method succeeded to derive both of the two duals deductively. These examples suggest that the proposed method is a prospective candidate for a universal and systematic method of the duality transformation.

3. 5. Appendix: Equivalency of Additional Charge Introduced to Replace a Lagrangian Multiplier

This section shows that the two Lagrangian expressions L_1 and L_2 shown in (3.49) and (3.50) are equivalent, if the initial values of fluxes are given so that the holonomic constraint $f(\phi;s)$ equals zero. The constraint $f(\phi;s)$ is given as a function of fluxes.

$$L_1 = L + \lambda f(\phi;s), \tag{3.49}$$

$$L_2 = L + N_\lambda \dot{q}_\lambda f(\phi;s), \tag{3.50}$$

where L is the Lagrangian contained in both expressions, λ is a Lagrangian multiplier, N_λ is the turn number of an additionally introduced winding, and q_λ is additionally introduced charge. N_λ is a constant value and we can assign any arbitrary value to it, and q_λ is assumed to be contained in neither L nor the dissipation function.

We substitute (3.50) into the Euler-Lagrange equation (3.7) with respect to q_λ and perform time integration. Then, we obtain

$$\frac{\partial L_2}{\partial \dot{q}_\lambda} = N_\lambda f(\phi; s) = C, \tag{3.51}$$

where C is an integration constant.

Then, we introduce another Lagrangian L_3, defined as

$$L_3 = L_2 - C\dot{q}_\lambda . \tag{3.52}$$

Now, we substitute (3.51) into (3.52) and denote the result as L'_3. According to Lagrangian dynamics [17], L'_3 is a known equivalent to L_2. Expressing the substitution by introducing an additional constraint, we obtain L'_3 as

$$\begin{aligned} L'_3 &= L_2 - C\dot{q}_\lambda + \lambda'(N_\lambda f(\phi; s) - C) \\ &= L + \lambda'(N_\lambda f(\phi; s) - C) + \dot{q}_\lambda (N_\lambda f(\phi; s) - C), \end{aligned} \tag{3.53}$$

where λ' is an additional Lagrangian multiplier.

Because the Lagrangian multiplier term ensures $N_\lambda f(\phi;s) - C = 0$, we can eliminate the term $\dot{q}_\lambda (N_\lambda f(\phi; s) - C)$. Then, we have

$$L'_3 = L + \lambda'(N_\lambda f(\phi; s) - C). \tag{3.54}$$

According to (3.51), $f(\phi;s)$ is constant. Hence, C equals the initial value of $f(\phi;s)$, which is given as zero. Substituting $C = 0$ into (3.54) yields

$$L'_3 = L + \lambda' N_\lambda f(\phi; s). \tag{3.55}$$

Renaming $\lambda' N_\lambda$ as λ in the above equation, we obtain L_1. Consequently, L_1 is equivalent to L'_3 and therefore to L_2.

REFERENCES

[1] S. D. Freeland, “Techniques for the practical application of duality to power circuits,” IEEE Trans. Power Electron., vol. 7, no. 2, pp. 374-384, April 1992.

[2] P. J. Wolfs, “A current-sourced DC-DC converter derived via the duality principle from the half-bridge converter,” IEEE Trans. Ind. Electron., vol.40, no.1, pp. 139-144, February 1993.

[3] C. K. Tse, Y. M. Lai, R. J. Xie, and M. H. L. Chow, “Application of duality principle to synthesis of single-stage power-factor-correction voltage regulators,” Int. J. Theor. Appl., vol.31, pp. 555-570, Nov./Dec. 2003.

[4] Z. H. Bai and Z. C. Zhang, “Conformation of multilevel current source converter topologies using the duality principle,” IEEE Trans. Power Electron., vol.23, no.5, pp. 2260-2267, Sept. 2008.

[5] M. Milonovic, I. Godec, and F. Mihalic, “An application of the duality principle to resonant link converters,” in Proc. Power Electron. Specialist Conf. (PESC), 1996, vol.2, pp. 1294-1299.

[6] B. A. Bloch, “On method for the construction of networks dual to non-planar networks,” in Proc. Phys. Soc., 1946, vol. 58, pp. 677-694.

[7] P. J. Wolfs, G. F. Ledwich, and K. C. Kwong, “The application of the duality principle to nonplanar circuits”, IEEE Trans. Power Electron., vol. 8, no. 2, pp. 104-111, April 1993.

[8] J. W. Kolar, H. Ertl, and F. C. Zach, “Analysis of the duality of three phase PWM converters with DC voltage link and DC current link,” in Proc. Ind. Appl. Soc. Annu. Meeting, 1989, vol. 1, pp. 724-737.

[9] M. Bierhoff, F. W. Fuchs, and S. Pischke, “Theoretical output current spectra of three phase current source converters,” in Proc. Europ. Conf. Power Electron. Appl. (EPE), 2005, pp. P1-P9.

[10] V. G. Agelidis and G. Joos, “On applying graph theory toward a unified analysis of three-phase PWM inverter topologies,” in Proc. 24th IEEE Power Electron. Specialist Conf. (PESC1993), 1993, pp. 408-415.

[11] P. A. Dahono, T. Kataoka, and Y. Sato, “Dual relationships between voltage-source and current-source three-phase inverters and its applications,” in Proc. Intl. Conf. Power Electron. Drive Syst. (PEDS), 1997, vol. 2, pp. 559-565.

[12] D. A. Wells, “Applications of Lagrange’s equations to electrical and electromechanical systems,” in Schaum’s Outline of Theory and Problems of Lagrangian Dynamics, New York: McGraw-Hill, 1976, pp.302-315.

[13] J. M. A. Scherpen, D. Jeltsema, and J. B. Klaasens, “Lagrangian modeling of switching electrical networks,” Syst. Control Lett., vol. 48, pp. 365-374, April 2003.

[14] K. Umetani, “A generalized method for Lagrangian modeling of power conversion circuit with integrated magnetic components,” IEEJ Trans. Elect. Electron. Eng., vol. 7, no. S1, pp. S146–S152, Nov. 2012.

[15] L. D. Landau and E. M. Lifshitz, “Damped oscillations” in Mechanics, Oxford, U. K.: Butterworth- Heinemann, 1976, pp.74-77.

[16] L. D. Landau and E. M. Lifshitz, “The equations of motion” in Mechanics, Oxford, U. K.: Butterworth- Heinemann, 1976, pp.2-4.

[17] C. Lanczos, “Kinosthenic or ignorable variables and their elimination,” in The Variational Principles of Mechanics, 4th ed., New York: Dover, 1970, pp.125-130.

Chapter 4

FLUX-BASED LAGRANGIAN FORMULATION FOR MODELING NONLINEARITY OF CONCENTRATED-WINDING SWITCHED RELUCTANCE MOTORS

4. 1. Introduction

Switched reluctance motors (SRMs) attract researchers' attention to their robust mechanical construction and cost effectiveness [1][2]. Nonetheless, practical applications of SRMs are still requiring control techniques that can solve the two difficulties: 1. large torque ripple, 2. large current ripple in the power supply to the motor drivers.

These difficulties are related with intense magnetic non-linearity of SRMs [1]–[3]. Therefore, SRM control should preferably consider the non-linearity. In addition, solving these difficulties often suffers from slow current response at the aligned position due to large inductance. Therefore, SRM control should preferably consider the flux waveforms to minimize the flux change rate, because it is limited by the voltage applicable to the phase winding. At the same time, SRM control may preferably consider behaviors of both the motor and its driver simultaneously, because the current ripple in the power supply, as well as the flux response, is dependent on both the motor and the driver. Consequently, progress in SRM control seems to be promoted by an analytical flux-based non-linear SRM model that can be directly combined with circuit models of motor drivers

As designing tools of SRM control, a number of analytical formulation for modelling SRMs have been proposed [4]–[15]. However, few of them meet the above requirements perfectly.

The purpose of this chapter is to propose a candidate that meets the requirements. This chapter employed Lagrangian dynamics as a modelling method because it can model kinetics and magnetics simultaneously. Furthermore, chapter 1 proposed Lagrangian formulation for electric circuits, enabling Lagrangian SRM models to be connected to motor driver models. Compared to the prior Lagrangian formulation reported in [13], the proposed formulation provides flux-based models and incorporates magnetic non-linearity.

This chapter is composed of the following 4 sections. Section 4.2 discusses Lagrangian expression of a system in which both kinetics and electromagnetics take place simultaneously. Particularly, we discuss the case of non-linear electromagnetic media. Section 4.3 derives the Lagrangian formulation of SRMs. First, we derive a generalized formulation of SRMs. Then, we discuss more simplified formulation, which the author believe to give more practical model of SRMs. Section 4.4 presents an operation analysis of a simple SRM driving system to show properness of the derived Lagrangian formulations. This section also shows that the proposed Lagrangian formulations

[†]Reproduced by permission of the Institution of Engineering & Technology, from K. Umetani, M. Yamamoto, and E. Hiraki, Simple flux-based Lagrangian formulation to model nonlinearity of concentrated-winding switched reluctance motors, 27 Oct. 2015.

provides flux-based non-linear models that can be analyzed in combination with Lagrangian models of motor driving circuits.

4. 2. Lagrangian Density of Kinetics and Electromagnetism

A. Lagrangian Density of Electromagnetic Fields in Non-Linear Media

This subsection derives an expression for Lagrangian density of electromagnetic field in non-linear media. We start our discussion from Maxwell's equations:

$$\operatorname{div}\mathbf{B}(t,\mathbf{x})=0\,, \tag{4.1}$$

$$\operatorname{rot}\mathbf{E}(t,\mathbf{x})+\frac{\partial\mathbf{B}(t,\mathbf{x})}{\partial t}=0\,, \tag{4.2}$$

$$\operatorname{div}\mathbf{D}(t,\mathbf{x})=\rho(t,\mathbf{x})\,, \tag{4.3}$$

$$\operatorname{rot}\mathbf{H}(t,\mathbf{x})-\frac{\partial\mathbf{D}(t,\mathbf{x})}{\partial t}=\mathbf{j}(t,\mathbf{x})\,, \tag{4.4}$$

where t is the time; $\mathbf{x}$ is the position vector; $\mathbf{D}$ and $\mathbf{B}$ are the electric and magnetic flux density vectors, respectively; $\mathbf{E}$ and $\mathbf{H}$ are the electric and magnetic field vectors, respectively; ρ is the electric charge; and $\mathbf{j}$ is the electric current vector.

We introduce the scalar potential $\psi(t,\mathbf{x})$ and the vector potential $\mathbf{A}(t,\mathbf{x})$ such that

$$\mathbf{B}(t,\mathbf{x})=\operatorname{rot}\mathbf{A}(t,\mathbf{x})\,, \tag{4.5}$$

$$\mathbf{E}(t,\mathbf{x})=-\frac{\partial\mathbf{A}(t,\mathbf{x})}{\partial t}-\operatorname{grad}\psi(t,\mathbf{x})=-\dot{\mathbf{A}}(t,\mathbf{x})-\operatorname{grad}\psi(t,\mathbf{x}), \tag{4.6}$$

where a dot over a variable is its time derivative.

Equations (4.5) and (4.6) automatically satisfy (4.1) and (4.2). Therefore, we only need to find a Lagrangian representing (4.3) and (4.4) as a function of ψ, $\mathbf{A}$, and $\dot{\mathbf{A}}$.

For convenience, we assume that $\mathbf{D}$ and $\mathbf{H}$ implicitly depend on ψ and $\mathbf{A}$ only through $\mathbf{E}$ and $\mathbf{B}$, respectively. In other words, $\mathbf{D}$ is a function of t, $\mathbf{r}$, and $\mathbf{E}$; and $\mathbf{H}$ is a function of t, $\mathbf{r}$, and $\mathbf{B}$. This indicates that we ignore the relativistic effects caused by moving media and regard the velocity of the media is sufficiently small compared to the light speed.

Particularly, in the linear media, in which $\mathbf{D}$ and $\mathbf{H}$ are proportional to $\mathbf{B}$ and $\mathbf{H}$, respectively, the Lagrangian density L_{d_lf} of the electromagnetic field is proposed in Chapter 1 as

$$L_{d\_lf}\left(\psi,\mathbf{A},\dot{\mathbf{A}}\right)=-\rho\psi+\mathbf{j}\cdot\mathbf{A}+\frac{1}{2}\varepsilon(t,\mathbf{x})\mathbf{E}\cdot\mathbf{E}-\frac{1}{2\mu(t,\mathbf{x})}\mathbf{B}\cdot\mathbf{B}, \tag{4.7}$$

where $\varepsilon(t,\mathbf{x})$ and $\mu(t,\mathbf{x})$ are the permittivity and permeability, respectively.

Now, we extend the Lagrangian density to include expressions for the electromagnetic field in the non-linear media, in which **D** and **H** are non-linear functions of **E** and **B**, respectively. As a possible candidate, we consider the Lagrangian density L_{d_nf} defined as

$$L_{d\_nf} = -\rho\psi + \mathbf{j}\cdot\mathbf{A} + \int_{\mathbf{0}}^{\mathbf{E}} \mathbf{D}\cdot d\mathbf{E} - \int_{\mathbf{0}}^{\mathbf{B}} \mathbf{H}\cdot d\mathbf{B}. \tag{4.8}$$

In linear media, we have $\mathbf{D}=\varepsilon\mathbf{E}$ and $\mathbf{H}=\mathbf{B}/\mu$. Therefore, (4.8) is a natural extension of L_{d_lf}. In order to confirm properness of this Lagrangian, we examine whether it yields (4.3) and (4.4).

We consider a system of electromagnetic field and integrate L_{d_nf} over a large region V containing this system. Then, the result of the integration gives Lagrangian L_a of this system. Hence, we have

$$L_a\left(\psi, \mathbf{A}, \dot{\mathbf{A}}\right) = -\int_V \rho\psi d\mathbf{x} + \int_V \mathbf{j}\cdot\mathbf{A} d\mathbf{x} + \int_V d\mathbf{x}\int_{\mathbf{0}}^{\mathbf{E}} \mathbf{D}\cdot d\mathbf{E} - \int_V d\mathbf{x}\int_{\mathbf{0}}^{\mathbf{B}} \mathbf{H}\cdot d\mathbf{B}, \tag{4.9}$$

where $d\mathbf{x}$ is the volume element.

Next, we take the variation of L_a with respect to ψ, **A**, and $\dot{\mathbf{A}}$. We consider arbitrary infinitesimal changes $\delta\psi$ and $\delta\mathbf{A}$ in ψ and **A** inside the region V. Therefore, we assume $\delta\psi$=0 and $\delta\dot{\mathbf{A}} = \delta\mathbf{A} = \mathbf{0}$ at the surface of V. We replace ψ **A**, and $\dot{\mathbf{A}}$ in (4.9) by $\psi+\delta\psi$, $\mathbf{A}+\delta\mathbf{A}$ and $\dot{\mathbf{A}}+\delta\dot{\mathbf{A}}$, respectively. Then, we subtract L_a from the resultant Lagrangian $L_a+\delta L_a$. Noting that **D** and **H** depend implicitly on ψ and **A** through **E** and **B**, we obtain the infinitesimal change δL_a in Lagrangian L_a as

$$\delta L_a = -\int_V \rho\delta\psi d\mathbf{x} + \int_V \mathbf{j}\cdot\delta\mathbf{A} d\mathbf{x} + \int_V \mathbf{D}\cdot\delta\mathbf{E} d\mathbf{x} - \int_V \mathbf{H}\cdot\delta\mathbf{B} d\mathbf{x}, \tag{4.10}$$

where $\delta\mathbf{E} = -\mathrm{grad}\,\delta\psi - \delta\dot{\mathbf{A}}$ and $\delta\mathbf{B} = \mathrm{rot}\,\delta\mathbf{A}$.

The third right-hand term can be developed as follows:

$$\begin{aligned}\int_V \mathbf{D}\cdot\delta\mathbf{E} d\mathbf{x} &= -\int_V \mathbf{D}\cdot\mathrm{grad}\,\delta\psi d\mathbf{x} - \int_V \mathbf{D}\cdot\delta\dot{\mathbf{A}} d\mathbf{x} \\ &= -\int_\Omega \delta\psi\mathbf{D} d\Omega + \int_V \mathrm{div}\,\mathbf{D}\,\delta\psi d\mathbf{x} - \int_V \mathbf{D}\cdot\delta\dot{\mathbf{A}} d\mathbf{x} \\ &= \int_V \mathrm{div}\,\mathbf{D}\,\delta\psi d\mathbf{x} - \int_V \mathbf{D}\cdot\delta\dot{\mathbf{A}} d\mathbf{x},\end{aligned} \tag{4.11}$$

where Ω is the surface of the region V and $d\Omega$ is its area element.

Similarly, the fourth right-hand term in (4.10) can be developed as follows:

$$
\begin{aligned}
-\int_V \mathbf{H}\cdot\delta\mathbf{B}d\mathbf{x} &= \int_\Omega \mathbf{H}\times\delta\mathbf{A}d\Omega - \int_V \operatorname{rot}\mathbf{H}\cdot\delta\mathbf{A}d\mathbf{x} \\
&= -\int_V \operatorname{rot}\mathbf{H}\cdot\delta\mathbf{A}d\mathbf{x}
\end{aligned}
\tag{4.12}
$$

Substituting (4.11) and (4.12) into (4.10) yields

$$
\begin{aligned}
\delta L_a = &\int_V \left(-\rho + \operatorname{div}\mathbf{D}\right)\delta\psi d\mathbf{x} - \int_V \mathbf{D}\cdot\delta\dot{\mathbf{A}}d\mathbf{x} \\
&+ \int_V \left(\mathbf{j} - \operatorname{rot}\mathbf{H}\right)\cdot\delta\mathbf{A}d\mathbf{x},
\end{aligned}
\tag{4.13}
$$

Hence, we obtain functional derivatives $\delta L_a / \delta\psi$, $\delta L_a / \delta\mathbf{A}$, $\delta L_a / \delta\dot{\mathbf{A}}$ as follows:

$$
\frac{\delta L_a}{\delta\psi} = -\rho + \operatorname{div}\mathbf{D}, \quad \frac{\delta L_a}{\delta\dot{\mathbf{A}}} = -\mathbf{D}, \quad \frac{\delta L_a}{\delta\mathbf{A}} = \mathbf{j} - \operatorname{rot}\mathbf{H}. \tag{4.14}
$$

The functional derivatives of a Lagrangian must satisfy Euler-Lagrange's equation. Hence, we have

$$
\frac{d}{dt}\left(\frac{\delta L_a}{\delta\dot{\mathbf{A}}}\right) - \frac{\delta L_a}{\delta\mathbf{A}} = 0, \tag{4.15}
$$

$$
-\frac{\delta L_a}{\delta\psi} = 0. \tag{4.16}
$$

Substituting (4.14) into (4.15) and (4.16) yields (4.3) and (4.4). Consequently, the Lagrangian density L_{d_nf} is confirmed to be a proper Lagrangian of the electromagnetic field in non-linear media.

B. Lagrangian Density Incorporating Kinetics and Electromagnetism

Although the Lagrangian density L_{d_nf} provides proper equations of the electromagnetism, it is not sufficient to derive a Lagrangian formulation for modeling a SRM. The reason is that the motor converts the electromagnetic energy into the kinetic energy, or vice versa. Hence, the Lagrangian model of a motor must comprise the kinetics as well as the electromagnetism, whereas L_{d_nf} defined in (4.8) does not comprise the kinetics.

In order to incorporate both the kinetics and the electromagnetism, we introduce a Lagrangian density L_d defined as

$$
L_d\left(\mathbf{r}_s, \dot{\mathbf{r}}_s, \psi, \mathbf{A}, \dot{\mathbf{A}}\right) = \sum_s \frac{1}{2} m_s \dot{\mathbf{r}}_s^{\,2}\delta\left(\mathbf{x} - \mathbf{r}_s\right) - \sum_s U_s\left(\mathbf{x}\right)\delta\left(\mathbf{x} - \mathbf{r}_s\right) + L_{d\_nf}, \tag{4.17}
$$

where s is an identifier of point masses, m_s is the mass of a point mass s, $\mathbf{r}_s(t)$ is the position vector of the point mass s, δ is the Dirac's delta function in 3 dimensions, and $U_s(\mathbf{x})$ is the kinetic potential for the point mass s.

Because now we discuss the motion of point masses with or without electric charge, we give definitions to $\rho(t,\mathbf{x})$ and $\mathbf{j}(t,\mathbf{x})$ in L_{d_nf} incorporated in L_d as a distribution and a flow of charged point masses, e.g. electrons:

$$\rho(t,\mathbf{x}) = \sum_s q_s \delta(\mathbf{x} - \mathbf{r}_s), \tag{4.18}$$

$$\mathbf{j}(t,\mathbf{x}) = \sum_s q_s \dot{\mathbf{r}}_s \delta(\mathbf{x} - \mathbf{r}_s), \tag{4.19}$$

where q_s is the charge of the point mass s. As for a point mass without electric charge, we regard q_s=0.

The first and second right-hand terms of (4.17) do not contain the scalar and vector potentials, i.e. ψ or $\mathbf{A}$. In addition, the above definitions are also free from ψ or $\mathbf{A}$. Therefore, the newly introduced Lagrangian density also yields the proper equations of the electromagnetic field, i.e. (4.3) and (4.4), as a result of taking variation with respect to ψ, $\mathbf{A}$, and $\dot{\mathbf{A}}$.

Accordingly, we only need to confirm that L_d yields a proper equation of motion of a point mass. For this purpose, we take variation with respect to $\dot{\mathbf{r}}_s$ and $\mathbf{r}_s$.

Again, we consider a system in which the kinetics and the electromagnetics take place and integrate L_d over a spatial region V that covers the system. Then, the result of integration is Lagrangian L_b of the system. Hence, we have

$$L_b(\mathbf{r}_s, \dot{\mathbf{r}}_s, \psi, \mathbf{A}, \dot{\mathbf{A}}) = \int_V L_d d\mathbf{x}. \tag{4.20}$$

Now, we consider arbitrary infinitesimal changes $\delta\mathbf{r}_s$ and $\delta\mathbf{r}_s$ in $\dot{\mathbf{r}}_s$ and $\mathbf{r}_s$. We replace $\dot{\mathbf{r}}_s$ and $\mathbf{r}_s$ in (4.20) by $\dot{\mathbf{r}}_s + \delta\dot{\mathbf{r}}_s$ and $\mathbf{r}_s+\delta\mathbf{r}_s$, respectively. Then, we subtract L_b from the resultant Lagrangian to obtain infinitesimal change δL_b in the Lagrangian. As a result, we have

$$\begin{aligned}\delta L_b &= \int_V \{\nabla_{\mathbf{r}_s} \delta(\mathbf{x} - \mathbf{r}_s) \cdot \delta\mathbf{r}_s\} T_s d\mathbf{x} + \int_V \{(m_s \dot{\mathbf{r}}_s + q_s \mathbf{A}) \cdot \delta\dot{\mathbf{r}}_s\} \delta(\mathbf{x} - \mathbf{r}_s) d\mathbf{x} \\ &= \int_V \{\nabla_{\mathbf{r}_s} \delta(\mathbf{x} - \mathbf{r}_s) \cdot \delta\mathbf{r}_s\} T_s d\mathbf{x} + (m_s \dot{\mathbf{r}}_s + q_s \mathbf{A}(t, \mathbf{r}_s)) \cdot \delta\dot{\mathbf{r}}_s,\end{aligned} \tag{4.21}$$

where $T_s(t, \dot{\mathbf{r}}_s, \mathbf{x}) \equiv \frac{1}{2} m_s \dot{\mathbf{r}}_s^{\,2} - U_s - q_s\psi + q_s \dot{\mathbf{r}}_s \cdot \mathbf{A}$. The operator $\nabla_{\mathbf{r}_s}$ is the three dimensional nabla with respect to position vector $\mathbf{r}_s$; namely, $\nabla_{\mathbf{r}_s} = {}^T(\partial/\partial r_{sx}, \partial/\partial r_{sy}, \partial/\partial r_{sz})$ in 3D Cartesian coordinate, if we express $\mathbf{r}_s$ as a vector

$^{T}(r_{sx}, r_{sy}, r_{sz})$ in the coordinate. In the rightmost equality, we used the fact that $\mathbf{r}_S$ is confined inside the region *V* of the system.

The first term of the rightmost side can be developed as follows:

$$\begin{aligned}
&\int_V \{\nabla_{\mathbf{r}_s} \delta(\mathbf{x}-\mathbf{r}_s)\cdot \delta\mathbf{r}_s\} T_s d\mathbf{x} = -\int_V \{\nabla_{\mathbf{x}} \delta(\mathbf{x}-\mathbf{r}_s)\cdot T_s \delta\mathbf{r}_s\} d\mathbf{x} \\
&\quad = -\int_V \nabla_{\mathbf{x}} \cdot \{\delta(\mathbf{x}-\mathbf{r}_s) T_s \delta\mathbf{r}_s\} d\mathbf{x} + \int_V (\nabla_{\mathbf{x}} \cdot T_s \delta\mathbf{r}_s)\delta(\mathbf{x}-\mathbf{r}_s) d\mathbf{x} \\
&\quad = -\int_V \nabla_{\mathbf{x}} \cdot \{\delta(\mathbf{x}-\mathbf{r}_s) T_s \delta\mathbf{r}_s\} d\mathbf{x} + \int_V (\nabla_{\mathbf{x}} T_s \cdot \delta\mathbf{r}_s)\delta(\mathbf{x}-\mathbf{r}_s) d\mathbf{x},
\end{aligned} \tag{4.22}$$

where the operator $\nabla_{\mathbf{x}}$ is the three dimensional nabla with respect to position vector **x**; namely, $\nabla_{\mathbf{x}} = (\partial/\partial x, \partial/\partial y, \partial/\partial z)^t$ in 3D Cartesian coordinate, if we express **x** as a vector $(x, y, z)^t$ in the coordinate.

If we apply the Gauss' divergence theorem to the first term of the rightmost side, we can find that the term vanishes because the value represented by braces in the term equals to zero anywhere on the surface of the region *V*. As a result, we obtain

$$\begin{aligned}
&\int_V \{\nabla_{\mathbf{r}_s} \delta(\mathbf{x}-\mathbf{r}_s)\cdot \delta\mathbf{r}_s\} T_s d\mathbf{x} = \int_V (\nabla_{\mathbf{x}} T_s \cdot \delta\mathbf{r}_s)\delta(\mathbf{x}-\mathbf{r}_s) d\mathbf{x} = \nabla_{\mathbf{r}_s} T_s(t, \dot{\mathbf{r}}_s, \mathbf{r}_s)\cdot \delta\mathbf{r}_s \\
&\quad = \{-\nabla_{\mathbf{r}_s} U_s(\mathbf{r}_s) - q_s \nabla_{\mathbf{r}_s} \psi(t, \mathbf{r}_s) + q_s(\dot{\mathbf{r}}_s \cdot \nabla_{\mathbf{r}_s})\mathbf{A}(t, \mathbf{r}_s) + q_s \dot{\mathbf{r}}_s \times \{\nabla_{\mathbf{r}_s} \times \mathbf{A}(t, \mathbf{r}_s)\}\}\cdot \delta\mathbf{r}_s.
\end{aligned} \tag{4.23}$$

According to (4.21) and (4.23), we obtain functional derivatives:

$$\frac{\delta L_b}{\delta \mathbf{r}_s} = -\nabla_{\mathbf{r}_s} U_s(\mathbf{r}_s) - q_s \nabla_{\mathbf{r}_s} \psi(t, \mathbf{r}_s) + q_s(\dot{\mathbf{r}}_s \cdot \nabla_{\mathbf{r}_s})\mathbf{A}(t, \mathbf{r}_s) + q_s \dot{\mathbf{r}}_s \times \{\nabla_{\mathbf{r}_s} \times \mathbf{A}(t, \mathbf{r}_s)\}, \tag{4.24}$$

$$\frac{\delta L_b}{\delta \dot{\mathbf{r}}_s} = m_s \dot{\mathbf{r}}_s + q_s \mathbf{A}(t, \mathbf{r}_s). \tag{4.25}$$

Consequently, Euler-Lagrange's equation with respect to $\dot{\mathbf{r}}_s$ and $\mathbf{r}_S$ yields

$$\begin{aligned}
&\frac{d}{dt}\{m_s \dot{\mathbf{r}}_s + q_s \mathbf{A}(t, \mathbf{r}_s)\} + \nabla_{\mathbf{r}_s} U_s(\mathbf{r}_s) + q_s \nabla_{\mathbf{r}_s} \psi(t, \mathbf{r}_s) \\
&\qquad - q_s(\dot{\mathbf{r}}_s \cdot \nabla_{\mathbf{r}_s})\mathbf{A}(t, \mathbf{r}_s) - q_s \dot{\mathbf{r}}_s \times \{\nabla_{\mathbf{r}_s} \times \mathbf{A}(t, \mathbf{r}_s)\} \\
&\qquad = m_s \ddot{\mathbf{r}}_s + q_s \dot{\mathbf{A}}(t, \mathbf{r}_s) + \nabla_{\mathbf{r}_s} U_s(\mathbf{r}_s) + q_s \nabla_{\mathbf{r}_s} \psi(t, \mathbf{r}_s) - q_s \dot{\mathbf{r}}_s \times \{\nabla_{\mathbf{r}_s} \times \mathbf{A}(t, \mathbf{r}_s)\} = 0.
\end{aligned} \tag{4.26}$$

The rightmost equality in (4.26) can be simplified using **E** and **B** according to (4.5) and (4.6):

$$m_s \ddot{\mathbf{r}}_s = -\nabla_{\mathbf{r}_s} U_s(\mathbf{r}_s) + q_s\{\mathbf{E}(t, \mathbf{r}_s) + \dot{\mathbf{r}}_s \times \mathbf{B}(t, \mathbf{r}_s)\}. \tag{4.27}$$

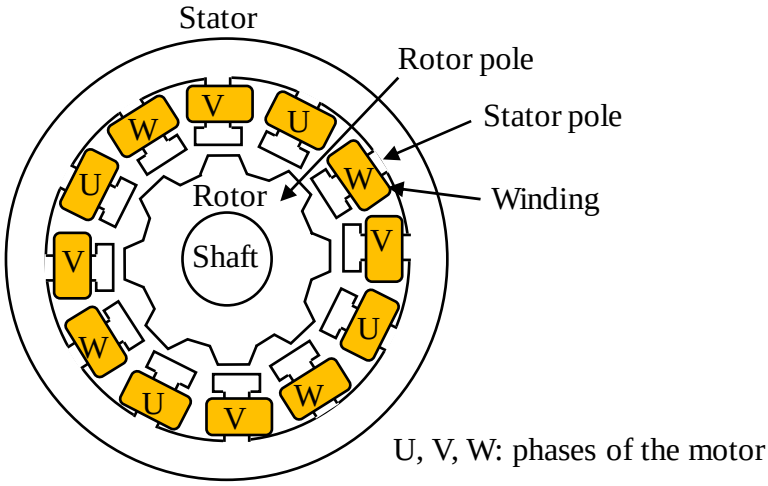

Fig. 4.1. Example of a concentrated-winding switched reluctance motor.

Equation (4.27) is a proper equation of motion of a point mass under influence of Lorenz force.

Consequently, the Lagrangian density L_d is confirmed to provide the kinetics as well as the electromagnetism in non-linear media, indicating that we can compose a Lagrangian expression for a SRM based on L_d.

4. 3. Lagrangian Formulation of a Switched Reluctance Motor

This section derives the Lagrangian formulation for modeling a concentrated-winding SRM. The motor is assumed to have multiple rotor pole pairs; and each rotor pole pair has as many stator poles as the phases, likewise the motor shown in Fig. 4.1. Hence, each phase consist of series-connected as many windings as the rotor pole pairs.

The Lagrangian model L_m of the SRM can be obtained by integrating the Lagrangian density L_d over a spatial region V_m that covers the motor; namely,

$$L_m = \int_{V_m} L_d \, d\mathbf{x}. \tag{4.28}$$

For convenience, we assume that effect of the kinetic potential $U_s(\mathbf{x})$, e.g. the gravity, is sufficiently small and that the motor is electrically neutral at any part of the motor. Hence, we can substitute $U_s(\mathbf{x})=0$ and $\rho(t,\mathbf{x})=0$. In addition, we can also ignore $\mathbf{D}(\mathbf{x})$ because of (4.3) and $\rho(t,\mathbf{x})=0$. As a result, we obtain:

$$\begin{aligned} L_m &= \int_{V_m} \sum_s \frac{1}{2} m_s \dot{\mathbf{r}}_s^{\,2} \delta(\mathbf{x}-\mathbf{r}_s) d\mathbf{x} + \int_{V_m} \mathbf{j}\cdot\mathbf{A} d\mathbf{x} - \int_{V_m} d\mathbf{x} \int_{\mathbf{0}}^{\mathbf{B}} \mathbf{H}\cdot d\mathbf{B} \\ &= \sum_s \frac{1}{2} m_s \dot{\mathbf{r}}_s^{\,2} + \int_{V_m} \mathbf{j}\cdot\mathbf{A} d\mathbf{x} - \int_{V_m} d\mathbf{x} \int_{\mathbf{0}}^{\mathbf{B}} \mathbf{H}\cdot d\mathbf{B}. \end{aligned} \tag{4.29}$$

The first term of the rightmost side of (4.29) represents the total kinetic energy of the system. As for a normal motor with a rotating rotor, only the rotor is a moving part. Hence, the term equals to the kinetic energy of the rotor, obtaining

$$\sum_s \frac{1}{2} m_s \dot{\mathbf{r}}_s^{\,2} = \frac{1}{2} I_r \dot{\theta}^2, \tag{4.30}$$

where I_r is the moment of inertia of the rotor and θ is the mechanical angle.

The second term of the rightmost side is the volume integration of the scalar product of the current density vector **j** and the vector potential **A**. Because the windings on a stator and a rotor is the only parts that carry the current, the term can be obtained by integrating the scalar product over the windings. According to Chapter 1, the result can be expressed as follows:

$$\int_{V_m} \mathbf{j} \cdot \mathbf{A} d\mathbf{x} = \sum_i N_i \dot{q}_i \phi_i, \tag{4.31}$$

where i is the index of the phase, N_j is the number of turns of a winding belonging to the phase i, and ϕ_i is the sum of the flux interlinking with the windings of the phase i. The variable q_i is the cumulative charge of the phase i defined as

$$q_i = \int_{t_o}^{t} dt \int_S \mathbf{j} \cdot d\mathbf{S}, \tag{4.32}$$

where t_0 is the initial time, S is the cross-section of the wire of a winding belonging to the phase i, and $d\mathbf{S}$ is the area element.

The third term of the rightmost side represents the total magnetic energy stored in the motor. Because the mechanical angle θ and the fluxes ϕ_1, ϕ_2, …suffice to determine the magnetic state of the motor, the third term can be expressed as a function only of θ and ϕ_1, ϕ_2, … .

Now, we seek for the function. We imagine that the rotor position is fixed. We denote the energy inflow per second to the motor through the phase i as P_i. If the voltage V_i is applied to the phase i, then P_i can be expressed as

$$P_i = V_i I_i = N_i \frac{d\phi_i}{dt} \frac{N_i I_i}{N_i} = F_i \frac{d\phi_i}{dt}, \tag{4.33}$$

where I_i is the current through the winding i and $F_i \equiv N_i I_i$ is the magneto-motive force of the winding. The magneto-motive force F_i is generally the function of the mechanical angle θ and the fluxes ϕ_1, ϕ_2, … .

We consider making an infinitesimal change $\delta\phi_i$ in ϕ_i by applying the voltage V_i during small period δt. Then, the energy δE_i added to make the change $\delta\phi_i$ is

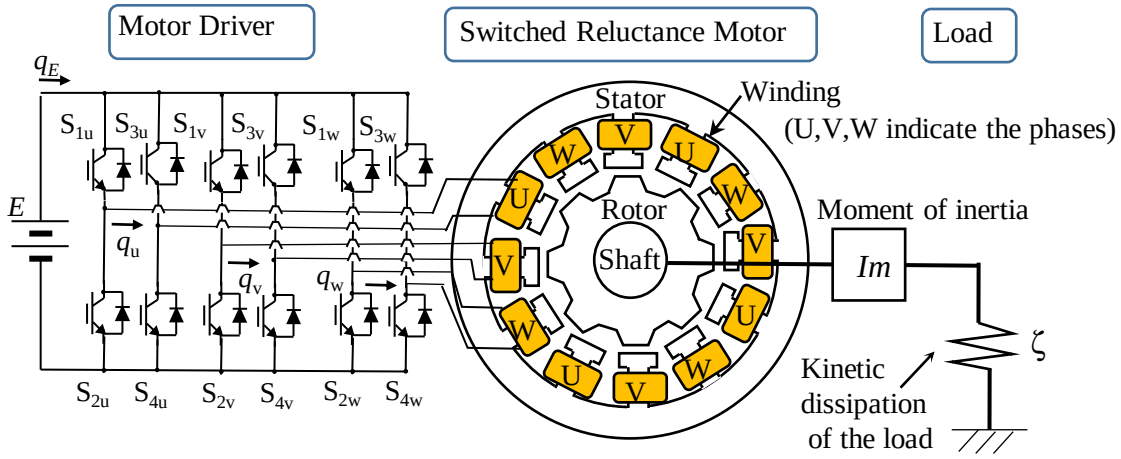

Fig. 4.2. Example of a switched reluctance motor driving system.

$$\delta E_i = P_i \delta t = F_i \frac{d\phi_i}{dt} \delta t = F_i \delta \phi_i. \tag{4.34}$$

Next, we consider making infinitesimal changes $\delta\phi_1$, $\delta\phi_2$, … in ϕ_1, ϕ_2, … during small period δt. The total energy δE added to make the changes is

$$\delta E = \sum_i \delta E_i = \sum_i F_i \delta \phi_i. \tag{4.35}$$

Because we assume that the rotor position is fixed, the energy δE equals to the increase in the magnetic energy stored in the motor. Hence, the magnetic energy in the rotor can be expressed as the total energy added through the windings to generate the fluxes ϕ_1, ϕ_2, … . If we denote the magnetic state of the motor as a vector $\boldsymbol{\varphi} = (\phi_1, \phi_2, \ldots)^t$, we obtain

$$\int_{V_m} d\mathbf{x} \int_{\mathbf{0}}^{\mathbf{B}} \mathbf{H} \cdot d\mathbf{B} = \int_{\mathbf{0}}^{\boldsymbol{\varphi}} \mathbf{F} \cdot d\boldsymbol{\varphi}, \tag{4.36}$$

where $d\boldsymbol{\varphi} = (d\phi_1, d\phi_2, \ldots)^t$ and is a function of θ and ϕ_1, ϕ_2, … defined as $\mathbf{F} = (F_1, F_2, \ldots)^t$.

Note that F_i cannot be replaced by another expression for the magneto-motive force $N_i \dot{q}_i$ because F_i is defined under the imaginary condition that the rotor position is fixed. The right-hand side of (4.36) is integrated under this imaginary condition. On the other hand, $N_i \dot{q}_i$ is the real magneto-motive force. Therefore, replacing F_i by $N_i \dot{q}_i$ will result in improper integration in (4.36).

As discussed above, all three terms in the right-most side of (4.29) has been simplified. As a result, we obtain a simplified expression for the motor Lagrangian L_m:

$$L_m = \frac{1}{2} I_r \dot{\theta}^2 + \sum_i N_i \dot{q}_i \phi_i - \int_{\mathbf{0}}^{\boldsymbol{\varphi}} \mathbf{F} \cdot d\boldsymbol{\varphi}. \tag{4.37}$$

Equation (4.37) employs the magneto-motive force to express the electric properties of the motor. However, the inductance may actually be more widely utilized than the magneto-motive force. If the inductance is more convenient, we can rewrite the motor Lagrangian L_m based on the inductance.

Let **M** be the inductance matrix of the windings in the motor. According to a definition of the inductance matrix, we have

$$\begin{aligned} &\frac{d}{dt}\begin{pmatrix} N_1\phi_1 \\ N_2\phi_2 \\ \vdots \end{pmatrix} = \mathbf{M}\frac{d}{dt}\begin{pmatrix} I_1 \\ I_2 \\ \vdots \end{pmatrix} \\ &\therefore \mathbf{N}\frac{d\boldsymbol{\varphi}}{dt} = \mathbf{M}\mathbf{N}^{-1}\frac{d\mathbf{F}}{dt}, \end{aligned} \tag{4.38}$$

where **N** is a diagonal matrix whose diagonal element is N_i:

$$\mathbf{N} = \begin{pmatrix} N_1 & 0 & 0 \\ 0 & N_2 & 0 \\ 0 & 0 & \ddots \end{pmatrix}. \tag{4.39}$$

Generally, each element of the inductance matrix M is a function of the mechanical angle θ and the fluxes ϕ_1, ϕ_2, … . Integrating (4.38) with respect to time, we obtain the magneto-motive force vector **F** expressed using the inductance matrix:

$$\mathbf{F} = \int_{\mathbf{0}}^{\boldsymbol{\varphi}} \mathbf{M}^{-1}\mathbf{N}^2 d\boldsymbol{\varphi}. \tag{4.40}$$

Substituting (4.40) into (4.37), we obtain the motor Lagrangian L_m expressed using the inductance matrix.

$$L_m = \frac{1}{2} I_r \dot{\theta}^2 + \sum_i N_i \dot{q}_i \phi_i - \int_{\mathbf{0}}^{\boldsymbol{\varphi}} \left(\int_{\mathbf{0}}^{\boldsymbol{\varphi}} \mathbf{M}^{-1}\mathbf{N}^2 d\boldsymbol{\varphi} \right) \cdot d\boldsymbol{\varphi}. \tag{4.41}$$

If we can neglect the mutual inductances between the windings, we can approximate the inductance matrix as a diagonal matrix whose diagonal elements are the self-inductance Λ_1, Λ_2, … . In this case we can simplify the equation (4.41):

$$L_m = \frac{1}{2} I_r \dot{\theta}^2 + \sum_i N_i \dot{q}_i \phi_i - \sum_i \int_0^{\phi_i} d\phi_i \int_0^{\phi_i} \frac{N_i^{\,2}}{\Lambda_i} d\phi_i. \tag{4.42}$$

If we can further neglect magnetic saturation of the self-inductance, we can regard the self-inductance Λ_i as a constant and further simplify the motor Lagrangian:

$$L_m = \frac{1}{2} I_r \dot{\theta}^2 + \sum_i N_i \dot{q}_i \phi_i - \sum_i \frac{N_i^{\,2}}{2\Lambda_i} \phi_i^{\,2}. \tag{4.43}$$

4. 4. Analytical Verification of Lagrangian Formulation

This section theoretically confirms that the motor Lagrangian L_m can yield proper equations of motor driving. We consider a simple motor driving system as shown in Fig. 4.2. In this system, a 3-phase concentrated winding SRM is driven by a battery (i.e. a constant voltage source) and a basic inverter under a basic load. We analyze this system using L_m to verify that the result is the same as the well known equations.

In the first step, we compose Lagrangian L_{sys} of this whole system as a sum of Lagrangian of the inverter, the motor, and kinetic load:

$$L_{sys} = L_{inv} + L_m + L_{load}, \tag{4.44}$$

where L_{inv} and L_{load} are Lagrangian of the inverter and the kinetic load, respectively.

Lagrandian L_{inv} can be configured from Lagrangian modeling of the electronic circuit as discussed in Chapter 1. According to Chapter 1, we obtain

$$L_{inv} = E q_E + \lambda \left(q_E - \sum_i s_i q_i \right). \tag{4.45}$$

where E is the voltage of the power source, q_E is the charge supplied from the power source, λ is the Lagrangian multiplier, and ζ is the dissipation coefficient of the load. Parameter s_i is the switching-state indicator. If S_{1i}, S_{4i} are in the on-state, s_i=1; if S_{2i}, S_{3i} are in the on-state, s_i=−1; and if S_{1i}, S_{3i} or S_{2i}, S_{4i} are in the on-state, s_i=0.

Lagrangian L_{load} can be configured according to kinetics of a rigid body. According to [16], we have

$$L_{load} = \frac{1}{2} I_m \dot{\theta}^2. \tag{4.46}$$

where I_m is the moment of inertia of the kinetic load.

Besides, we introduce the dissipation function D_{sys} [17] of the driving system in order to express kinetic energy dissipation at the kinetic load. According to [17], we can express D_{sys} as

$$D_{sys} = \frac{1}{2} \zeta \dot{\theta}^2. \tag{4.47}$$

First, we adopt the general expression (4.37) as L_m. As a result, Lagrangian L_{sys} of the whole system can be expressed as follows:

$$L_{sys} = \frac{1}{2} I_m \dot{\theta}^2 + E q_E + \lambda \left(q_E - \sum_i s_i q_i \right) + \frac{1}{2} I_r \dot{\theta}^2 + \sum_i N_i \dot{q}_i \phi_i - \int_{\mathbf{0}}^{\boldsymbol{\varphi}} \mathbf{F} \cdot d\boldsymbol{\varphi} \,. \tag{4.48}$$

Now, we apply (4.47) and (4.48) to Euler-Lagrange equation (1.26). Euler-Lagrange equations with respect to q_E, λ, q_i, ϕ_i, and θ yield the following equations:

$$E + \lambda = 0 \,, \tag{4.49}$$

$$q_E - \sum_i s_i q_i = 0 \,, \tag{4.50}$$

$$N_i \dot{\phi}_i = -\lambda s_i \,, \tag{4.51}$$

$$N_i \dot{q}_i - F_i(\theta, \phi_1, \phi_2, \cdots) = 0 \,, \tag{4.52}$$

$$(I_m + I_r)\ddot{\theta} + \frac{\partial}{\partial \theta}\bigg|_{\phi} \int_{\mathbf{0}}^{\boldsymbol{\varphi}} \mathbf{F} \cdot d\boldsymbol{\varphi} = -\zeta \dot{\theta} \,, \tag{4.53}$$

where a bar with subscript 'ϕ' indicates that the partial derivative is taken while keeping all ϕ_i constant. We eliminate the Lagrangian multiplier from (4.49) and (4.51), and rewrite (4.49)–(4.53). Then, we have

$$q_E = \sum_i s_i q_i \,, \tag{4.54}$$

$$N_i \dot{\phi}_i = s_i E \,, \tag{4.55}$$

$$N_i \dot{q}_i = F_i(\theta, \phi_1, \phi_2, \cdots), \tag{4.56}$$

$$\tau = (I_m + I_r)\ddot{\theta} + \zeta \dot{\theta} = -\frac{\partial}{\partial \theta}\bigg|_{\phi} \int_{\mathbf{0}}^{\boldsymbol{\varphi}} \mathbf{F} \cdot d\boldsymbol{\varphi} \,. \tag{4.57}$$

Equation (4.55) gives dynamics of the flux in the SRM. Furthermore, (4.56) and (4.57) give the phase current $\dot{q}_i$ and the torque τ as non-linear functions of the flux. Therefore, the proposed Lagrangian SRM formulation provides a flux-based model that can express non-linearity of SRMs.

Equations (4.54)–(4.56) are apparently proper. Equation (4.54) indicates the conservation of the electric charge at the inverter because the charge from the power supply equals to the charge flowing through high-side switches $S_{1u–w}$ and $S_{3u–w}$ of the motor driver. Equation (4.55) indicates Faraday's law. Equation (4.56) indicates that the phase current equals to the magnetomotive force $F_i(\theta, \phi_1, \phi_2, \ldots)$.

Equation (4.57) gives a torque; and is also appropriate because its right-most side equals to the partial derivative of magnetic co-energy W^* with respect to θ while keeping the phase current constant. In fact, W^* can be expressed as

$$W^* = \int_{\mathbf{0}}^{\mathbf{F}} \boldsymbol{\varphi}(\theta, F_1, F_2, \cdots) \cdot d\mathbf{F} = \boldsymbol{\varphi} \cdot \mathbf{F} - \int_{\mathbf{0}}^{\boldsymbol{\varphi}} \mathbf{F}(\theta, \phi_1, \phi_2, \cdots) \cdot d\boldsymbol{\varphi} \,. \tag{4.58}$$

If we assume infinitesimal change $\delta\theta$ in the mechanical angle θ under constant phase current, we can obtain the change δW^* in W^* as follows:

$$\delta W^* = \left.\frac{\partial \boldsymbol{\varphi}}{\partial \theta}\right|_{cur} \delta\theta \cdot \mathbf{F} - \left(\left.\frac{\partial}{\partial \theta}\right|_{cur} \int_{\mathbf{0}}^{\boldsymbol{\varphi}} \mathbf{F}(\theta, \phi_1, \phi_2, \cdots) \cdot d\boldsymbol{\varphi} \right) \delta\theta \,, \tag{4.59}$$

where bars with subscript '*cur*' indicate that the partial derivative is taken while keeping all the phase current constant. Developing (4.59), we obtain

$$\begin{aligned} \delta W^* &= \left.\frac{\partial \boldsymbol{\varphi}}{\partial \theta}\right|_{cur} \delta\theta \cdot \mathbf{F} - \left(\left.\frac{\partial}{\partial \theta}\right|_{\phi} \int_{\mathbf{0}}^{\boldsymbol{\varphi}} \mathbf{F}(\theta, \phi_1, \phi_2, \cdots) \cdot d\boldsymbol{\varphi} \right) \delta\theta \\ &\quad - \sum_i \left(\frac{\partial}{\partial \phi_i} \int_{\mathbf{0}}^{\boldsymbol{\varphi}} \mathbf{F}(\theta, \phi_1, \phi_2, \cdots) \cdot d\boldsymbol{\varphi} \right) \cdot \left.\frac{\partial \phi_i}{\partial \theta}\right|_{cur} \delta\theta \\ &= \left.\frac{\partial \boldsymbol{\varphi}}{\partial \theta}\right|_{cur} \delta\theta \cdot \mathbf{F} - \left(\left.\frac{\partial}{\partial \theta}\right|_{\phi} \int_{\mathbf{0}}^{\boldsymbol{\varphi}} \mathbf{F}(\theta, \phi_1, \phi_2, \cdots) \cdot d\boldsymbol{\varphi} \right) \delta\theta - \sum_i F_i \cdot \left.\frac{\partial \phi_i}{\partial \theta}\right|_{cur} \delta\theta \\ &= -\left(\left.\frac{\partial}{\partial \theta}\right|_{\phi} \int_{\mathbf{0}}^{\boldsymbol{\varphi}} \mathbf{F}(\theta, \phi_1, \phi_2, \cdots) \cdot d\boldsymbol{\varphi} \right) \delta\theta, \end{aligned} \tag{4.60}$$

where bars with subscript 'ϕ' indicate that the partial derivative is taken while keeping all the flux ϕ_i constant.

Finally, we obtain the following relation:

$$\left.\frac{\partial W^*}{\partial \theta}\right|_{cur} = -\left.\frac{\partial}{\partial \theta}\right|_{\phi} \int_{\mathbf{0}}^{\boldsymbol{\varphi}} \mathbf{F} \cdot d\boldsymbol{\varphi}. \tag{4.61}$$

Equation (4.61) indicates that (4.57) is a proper equation of torque.

Consequently, the generalized motor Lagrangian given by (4.37) is found to yield proper equations of motor driving.

Next, we adopt the simplified formulation (4.43) as L_m. Substituting (4.43), (4.45), and (4.46) into (4.44), Lagrangian L_{sys} of the whole system can be obtained as

$$L_{sys} = \frac{1}{2} I_m \dot{\theta}^2 + E q_E + \lambda \left(q_E - \sum_i s_i q_i \right) + \frac{1}{2} I_r \dot{\theta}^2 + \sum_i N_i \dot{q}_i \phi_i - \sum_i \frac{N_i^{\,2}}{2\Lambda_i} \phi_i^{\,2} \,. \tag{4.62}$$

Now, we apply (4.47) and (4.62) to Euler-Lagrange equation (1.26). Euler-Lagrange equations with respect to q_E, λ, q_i, ϕ_i, and θ yield the following equations after eliminating the Lagrangian multiplier:

$$q_E = \sum_i s_i q_i \,, \tag{4.63}$$

$$N_i \dot{\phi}_i = s_i E \,, \tag{4.64}$$

$$\Lambda_i \dot{q}_i = N_i \phi_i \,, \tag{4.65}$$

$$\tau = \left(I_m + I_r \right) \ddot{\theta} + \zeta \dot{\theta} = -\sum_i \frac{\partial}{\partial \theta}\bigg|_{\phi} \left(\frac{N_i^{\,2}}{2\Lambda_i} \phi_i^{\,2} \right). \tag{4.66}$$

Equation (4.64) gives dynamics of the flux in the SRM. Furthermore, (4.65) and (4.66) give the phase current $\dot{q}_i$ and the torque τ as non-linear functions of the flux. Therefore, the simplified Lagrangian SRM formulation given by (4.37) also provides a flux-based model. Substituting (4.65) into (4.66), we obtain the well-known expression for torque:

$$\tau = -\sum_i \frac{\partial}{\partial \theta}\bigg|_{\phi} \left(\frac{N_i^{\,2}}{2\Lambda_i} \phi_i^{\,2} \right) = -\sum_i \frac{N_i^{\,2} \phi_i^{\,2}}{2} \frac{\partial}{\partial \theta} \left(\frac{1}{\Lambda_i} \right) = \sum_i \frac{N_i^{\,2} \phi_i^{\,2}}{2\Lambda_i^{\,2}} \frac{\partial \Lambda_i}{\partial \theta} = \sum_i \frac{1}{2} \frac{\partial \Lambda_i}{\partial \theta} \dot{q}_i^{\,2} \,. \tag{4.67}$$

In the second equality in the above equation, a bar at $\partial/\partial\theta$ is eliminated because Λ_i is assumed to be a function only of θ.

Consequently, the simplified motor Lagrangian given by (4.43) is also found to yield proper equations of motor driving.

4. 5. Conclusions

Practical applications of switched reluctance motors (SRMs) require control techniques that can solve large torque ripple and large current ripple in power supply. In order to promote development of these techniques, this chapter proposed a Lagrangian formulation for flux-based non-linear SRM models. This formulation can be analysed in combination with Lagrangian circuit models of motor drivers. Properness of the formulation is supported by an example of operation analysis of a simple SRM driving system.

REFERENCES

[1] Z. Q. Zhu, C. C. Chan, “Electrical machine topologies and technologies for electric, hybrid, and fuel cell vehicles”, in Proc. IEEE Vehicle Power Propulsion Conf., Harbin, China, 2008, pp. 1–6.

[2] D. Panda and V. Ramanarayanan, “Reduced acoustic noise variable DC-bus-voltage-based sensorless switched reluctance motor drive for HVAC applications,” IEEE Trans. Ind. Electron., vol. 54, no. 4, pp. 2065-2078, Aug. 2007.

[3] W. Suppharangsan and J. Wang, “Experimental validation of a new switching technique for DC-link capacitor minimization in switched reluctance machine drives,” in Proc. IEEE Intl. Elect. Mach. Drives Conf., Chicago, USA, 2013, pp. 1031–1036.

[4] L. Xu and E. Ruckstadter, “Direct method of switched reluctance machine by coupled field-circuit model,” IEEE Trans. Energy Convers., vol. 10, no. 3, pp. 446-454, Sept. 1995.

[5] M. Stiebler and K. Liu, “An analytical model of switched reluctance machines,” IEEE Trans. Energy Convers., vol. 14, no. 4, pp. 1100-1107, Dec. 1999.

[6] V. Vujicic and S. N. Vukosavic, “A simple nonlinear model of the switched reluctance motor,” IEEE Trans. Energy Convers., vol. 15, no. 4, pp. 395-400, Dec. 2000.

[7] C. Roux and M. M. Morcos, “On the use of a simplified model for switched reluctance motors,” IEEE Trans. Energy Convers., vol. 17, no. 3, pp. 400-405, Sep. 2002.

[8] D. N. Essah and S. D. Sudhoff, “An improved analytical model for the switched reluctance motor,” IEEE Trans. Energy Convers., vol. 18, no. 3, pp. 349-356, Sept. 2003.

[9] L. C. Lovatt, “Analytical model of a classical switched reluctance motor,” IEE Proc. Electr. Power Appl., vol. 152, no. 2, pp. 352-358, Mar. 2005.

[10] H. P. Chi, R. L. Lin, and J. F. Chen, “Simplified flux-linkage model for switched reluctance motors,” IEE Proc. Electr. Power Appl., vol. 152, no. 3, pp. 577-583, May 2005.

[11] M. Farshad, J. Faiz, and C. Lucas, “Development of analytical models of switched reluctance motor in two-phase excitation mode: extended miller model,” IEEE Trans. Magn., vol. 41, no. 6, pp. 2145-2155, Jun. 2005.

[12] A. Khalil and I. Husain, “A fourier series generalized geometry-based analytical model of switched reluctance machines,” IEEE Trans. Ind. Appl., vol. 43, no. 3, pp. 673-684, May/Jun. 2007.

[13] I. Moson and A. Wilk, “Lagrange’s energy method based approach for switched reluctance drive systems modelling,” in Proc. European Conf. Power Electron. Appl., Aalborg, Denmark, 2007, pp. 1–10.

[14] H. Chen, D. Jiang, J. Yang, and L. Shi, “A new analytical model for switched reluctance motors,” IEEE Trans. Magn., vol. 45, no. 8, pp. 3107–3113, Aug. 2009.

[15] D. Lin, P. Zhou, S. Stanton, and Z. J. Cendes, “An analytical circuit model of switched reluctance motors,” IEEE Trans. Magn., vol. 45, no. 12, pp. 5368–5375, Aug. 2009.

[16] L. D. Landau and E. M. Lifshitz, “Motion of a rigid body” in Mechanics, Oxford, U. K.: Butterworth- Heinemann, 1976, pp.96-110.

[17] C. Lanczos, “Kinosthenic or ignorable variables and their elimination,” in The Variational Principles of Mechanics, 4th ed., New York: Dover, 1970, pp.125-130.

PART II:

Practical Applications of Lagrangian Methodology

Chapter 5

MAGNETIC STRUCTURE INTEGRATING DIFFERENTIAL-MODE AND COMMON-MODE INDUCTORS WITH IMPROVED TOLERANCE TO DC SATURATION

5. 1. Introduction

Recently, high power density is intensely required for switching converters. Accordingly, their circuit components are also required to be miniaturized. Particularly, magnetic devices for EMC filters, such as differential-mode (DM) inductors and common-mode (CM) inductors, often occupy a significant volume. Therefore, a number of techniques [1]–[11] have been proposed to miniaturize DM and CM inductors.

A promising approach is to integrate a DM inductor and a CM inductor into a single device. As well-known examples [1]–[3], highly integrated structures are proposed based on planar magnetic cores. These structures are beneficial in further integrating capacitors by inserting a dielectric layer between a pair of planar windings. However, these structures can suffer from excessive copper loss in high power applications because planar core generally requires long wire length for the windings. The same benefit and problem also tend to occur in the structures in which conductive foils are used as windings [4] because the foils tend to have large DC resistance compared to thick wires. Therefore, high power applications often prefer integration techniques based on bulk core with windings of thick wire.

This type of techniques has also been reported in a number of studies. These techniques can be classified into two major categories. One is the structural integration [5]–[8], which integrates DM and CM inductors on separate magnetic cores partly sharing the windings. Techniques of this category are beneficial in reducing the dead space because the cores can be closely placed by sharing the windings. The other category is the magnetic integration [9]–[11], which integrates DM and CM inductors on a single magnetic core. Techniques of this category allow sharing not only the windings but also the core between the DM and CM inductors. Compared to the structural integration, the magnetic integration can offer further miniaturization because the total core volume may also be reduced by sharing magnetic paths.

On the other hand, the magnetic integration has a drawback that the CM inductance, as well as the DM inductance, can saturate because the DC flux induced by the DM current can cause magnetic saturation in the shared magnetic path. This may require expanding the cross-section of magnetic paths to design necessary tolerance to the magnetic saturation not only of the DM inductance but also of the CM inductance. As a result, the miniaturizing effect of the magnetic integration may be hindered.

[†] Reprinted, with permission, from K. Umetani, T. Tera, and K. Shirakawa, A Magnetic Structure Integrating Differential-Mode and Common-Mode Inductors with Improved Tolerance to DC Saturation, IEEJ Journal of Industry Applications, May 2015.

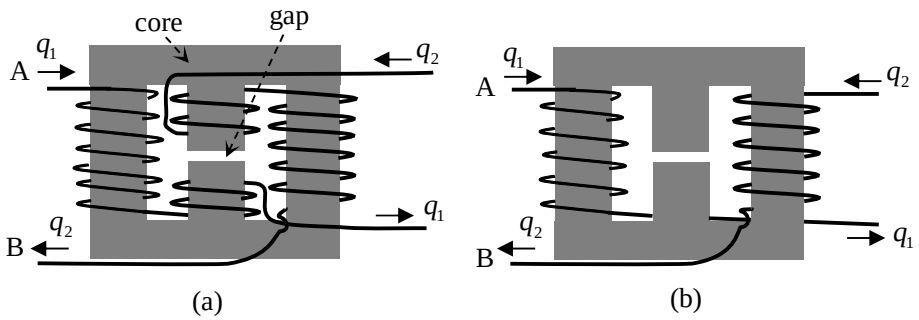

Fig. 5.1. Magnetic structures integrating DM and CM inductors. (a) Proposed structure. (b) Conventional structure.

An effective strategy to alleviate the problem is to suppress the DC flux. This strategy generally requires increasing the equivalent number of turns N_{DM} that link with the flux induced by the DM current. Below, we show the reason.

As an analogy to the basic inductor with a single magnetic path, we can define N_{DM} as the ratio [12] of the total flux linkage to the flux, when only DM current is applied. Hence, we obtain (5.1), if we assume constant DM inductance L_{DM}.

$$N_{DM} \equiv \frac{L_{DM} I_{DM}}{\phi_{DM}},$$

$$\therefore \phi_{DM} = \frac{L_{DM} I_{DM}}{N_{DM}}, \tag{5.1}$$

where ϕ_{DM} is the flux induced by the DM current I_{DM}.

Accordingly, we can express the DC flux ϕ_{DC} induced by the DC component I_{DC} in I_{DM} as follows:

$$\phi_{DC} = \frac{L_{DM} I_{DC}}{N_{DM}}. \tag{5.2}$$

Because L_{DM} and the maximum value for I_{DC} are generally specified as requirement, increasing N_{DM} is indispensable to suppressing ϕ_{DC}.

However, as shown in this chapter, N_{DM} is restricted to only half of the total number of turns on the conventional magnetic structure employed in the prior works [9]–[11]. Therefore, the conventional structure often suffer from large DC flux induction. Due to the problem, the conventional structure may not offer effective miniaturization of DM and CM inductors.

The purpose of this chapter is to address the problem by proposing a novel magnetic structure. In the proposed structure, more winding turns can be assigned to N_{DM} than the conventional structure in order to suppress the DC flux induction. As a result, further reduction in the core volume can be expected, if magnetic saturation is a determining

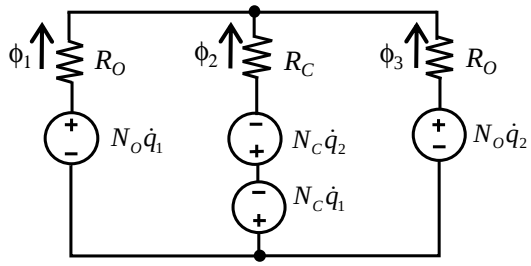

Fig. 5.2. Magnetic circuit model of the proposed structure.

factor in the cross-sectional area of the magnetic paths, as is often the cases when large L_{DM} or large I_{DC} is specified.

This chapter investigates the proposed structure in the following four sections. Section 5.2 analyzes the operating principles of the proposed structure theoretically. Then, Section 5.3 verifies the operating principles experimentally. Section 5.3 also verifies that the proposed structure can miniaturize the discrete DM and CM inductors by the magnetic integration. Section 5.4 analytically compares the core volume between the proposed and conventional structures to verify the core reduction effect of suppressing the DC flux. In this comparison, the core dimensions are estimated under the same wire length and under the same specifications in which magnetic saturation dominantly determines the cross-sectional area of magnetic paths. Finally, Section 5.5 presents the conclusions.

5. 2. Proposed Magnetic Structure

A. Operating Principles

Figure 5.1(a) illustrates the proposed magnetic structure. The structure has a core with three legs. The center leg has a gap and two windings with the same number of turns. The windings on the center leg are both wound so that DM current induce the same direction of flux. Each of the outer legs has a winding connected in series with one of the windings on the center leg. The windings on the outer legs have the same number of turns and are wound so that DM current induce the flux in the outer leg in the direction that reinforces the flux in the center leg.

On the other hand, the conventional magnetic structure employed in the prior works [9]–[11] is magnetically equivalent to Fig. 5.1(b). It differs from the proposed structure in the windings on the center leg.

Electrical functions of the proposed structure are equivalent to series-connected discrete DM and CM inductors, as well as the conventional structure. Below, we show the reason utilizing the Lagrangian modeling.

As discussed in Part I, the Lagrangian modeling offers a systematic method to transform an integrated magnetic component into an equivalent circuit of basic transformers and inductors, each of which consists of a single closed magnetic path. In this method, we first translate the physical magnetic structure into Lagrangian, which can be directly configured from their electric and magnetic networks. Then, we apply a point transformation [13] to the Lagrangian, obtaining another Lagrangian that belongs to a

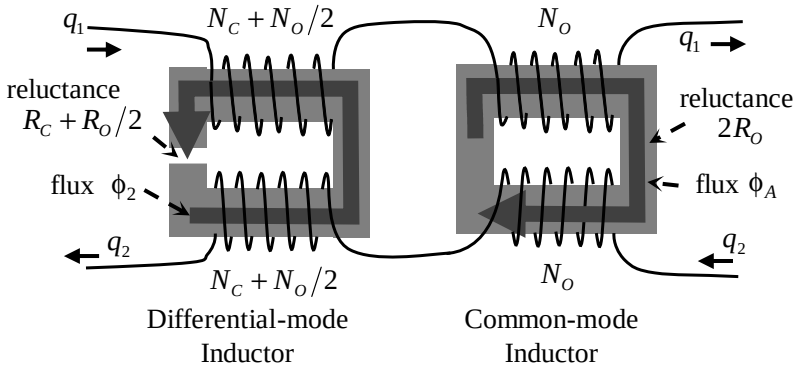

Fig. 5.3. Equivalent circuit of the proposed structure.

circuit of basic transformers and inductors. Finally, we again translate the resultant Lagrangian to obtain the equivalent circuit.

Now, we apply this method to the proposed structure. The magnetic circuit of the proposed structure can be expressed as Fig. 5.2. N_C and N_O are the numbers of turns of the center leg windings and the outer leg windings, respectively. R_C and R_O are the reluctance of the center leg and the outer legs, respectively. The two outer legs are designed to have the same reluctance R_O according to the designing concept of the proposed structure. We denote the electric charge that flows through the winding A and B as q_1 and q_2, respectively. Then, translating Fig. 5.2 yields the following Lagrangian L:

$$L = N_O\dot{q}_1\phi_1 + N_O\dot{q}_2\phi_3 - N_C\dot{q}_1\phi_2 - N_C\dot{q}_2\phi_2 - \frac{1}{2}R_O\phi_1^{\,2} - \frac{1}{2}R_C\phi_2^{\,2} - \frac{1}{2}R_O\phi_3^{\,2} + \lambda(\phi_1 + \phi_2 + \phi_3), \tag{5.3}$$

where λ is a Lagrangian multiplier; ϕ_1, ϕ_2, and ϕ_3 are the fluxes of the left outer leg, the center leg, and the right outer leg, respectively. A dot over a variable indicates its time derivative.

The Lagrangian multiplier can be eliminated by substituting $\phi_3 = -\phi_1 - \phi_2$ into (5.3). Then, we have

$$L = N_O\dot{q}_1\phi_1 - N_O\dot{q}_2(\phi_1 + \phi_2) - N_C\dot{q}_1\phi_2 - N_C\dot{q}_2\phi_2 - \frac{1}{2}R_O\phi_1^{\,2} - \frac{1}{2}R_C\phi_2^{\,2} - \frac{1}{2}R_O(\phi_1 + \phi_2)^2. \tag{5.4}$$

Next, we apply a point transformation to the result. The purpose of this transformation is to convert the magnetic energy terms in (5.4), i.e. the fifth, sixth, and seventh terms, into a diagonal form of the fluxes. Then, the resultant Lagrangian corresponds to a circuit of magnetic components each made of a single closed magnetic path. Introducing a flux ϕ_A defined as $\phi_A = \phi_1 + \phi_2/2$ to eliminate ϕ_1, we obtain

$$L = N_O(\dot{q}_1 - \dot{q}_2)\phi_A - \left(N_C + \frac{N_O}{2}\right)(\dot{q}_1 + \dot{q}_2)\phi_2 - R_O{\phi_A}^2 - \left(R_C + \frac{R_O}{2}\right)\frac{{\phi_2}^2}{2}. \tag{5.5}$$

Lagrangian obtained in (5.5) can be translated into a series connection of discrete DM and CM inductors as illustrated in Fig. 5.3. The flux ϕ_2 constitutes a DM inductor that has two windings with the number of turns N_C+N_O/2, whereas ϕ_A constitutes a CM inductor that has two windings with the number of turns N_O. Note that N_C=0 corresponds to the conventional structure. Because N_C=0 in Fig. 5.3 gives the equivalent circuit for the conventional structure, the number of turns on its equivalent DM inductor equals to only half of the total number of turns on the conventional structure. Thus, the proposed structure increases the number of turns on the DM inductor by $2N_C$ by adding two windings with the number of turns N_C. On the other hand, it keeps the number of turns on the CM inductor unchanged.

B. Merits and Drawbacks

Now, we examine whether the proposed structure allows its equivalent DM inductor to have greater number of turns than the conventional structure. For this purpose, we compare the number of turns on the equivalent DM inductor between the proposed and conventional structures under the same total wire length and the same core dimensions.

First, we investigate the wire length per turn on the center and outer legs. As we have seen in the previous subsection, the flux through the center leg ϕ_2 corresponds to the flux of the DM inductor. On the other hand, the relations $\phi_1 = \phi_A - \phi_2/2$ and $\phi_3 = -\phi_A - \phi_2/2$ indicate that the fluxes through the outer legs are the sum of the flux of the CM inductor and half the flux of the DM inductor. Hence, the cross-sectional area A_O of the outer leg should be designed at least greater than half the cross-sectional area A_C of the center leg. Accordingly, we have

$$A_C \le 2A_O. \tag{5.6}$$

If we assume the same cross-sectional shape among the center and outer legs, we obtain the following relation between the perimeter l_C of the center leg and the perimeter l_O of the outer leg using the fact that the perimeter is proportional to the square root of the cross-sectional area:

$$l_C \le \sqrt{2} l_O,$$

$$\therefore l_C < 2l_O. \tag{5.7}$$

Equation (5.7) shows that one turn on the center leg is shorter than two turns on the outer legs. On the other hand, one turn on the center leg is equivalent in the DM inductor in Fig. 5.3 to two turns on the outer leg. Therefore, the proposed structure can equip its DM inductor with the same number of turns using shorter wire than the conventional structure. In other words, the proposed structure can equip the DM inductor with a greater number of turns under the same total wire length.

Table. 5.1. Requirement specifications and evaluation results of the prototypes.

	Requirement	Proposed Structure	Discrete Inductors
DM Inductance[a]	60μH	61μH	60μH
DM Saturation Current[b]	22.5A	26.4A	22.8A
CM Inductance[a]	440μH	476μH	447μH
CM Saturation Current[b]	22.5A	31.1A	—
DC Resistance	16.5mΩ	16.1mΩ	16.4mΩ

a) Inductance is specified when the DM current of 16A is applied.

b) DM current when the DM or CM inductance decreases to 75% of its initial value.

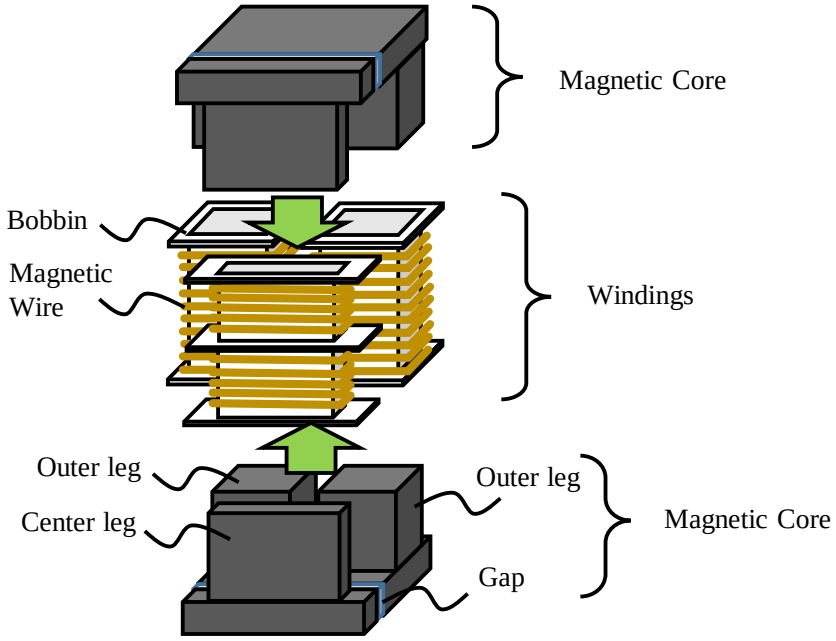

Fig. 5.4. Physical structure of the prototype of the proposed structure.

This indicates that the proposed structure can effectively suppress the DC flux induced by the DC component in the DM current. Because the DC flux flows in both the center and outer legs, excessive DC flux increases not only R_C but also R_O, causing saturation of both the DM and CM inductance. Hence, the proposed structure can suppress saturation of both the DM and CM inductance, thus avoiding the center and outer legs from being designed with expanded cross-section to ensure necessary tolerance to saturation.

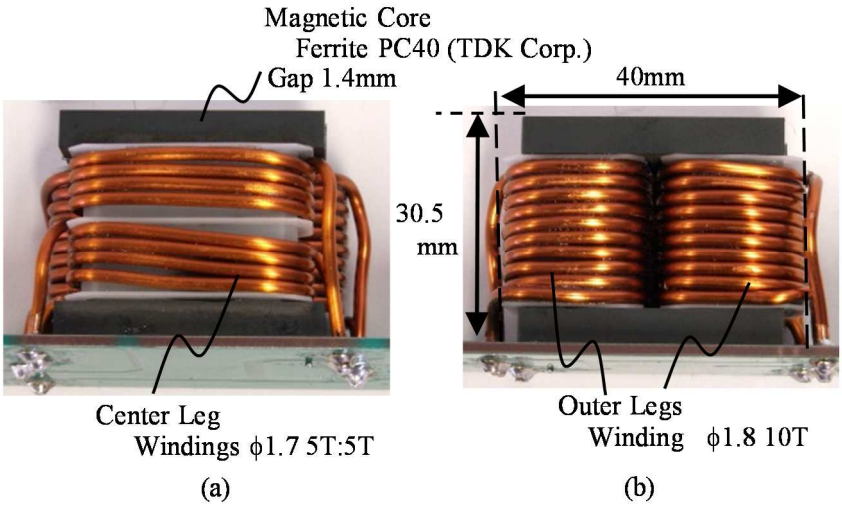

Fig. 5.5. Photographs of the prototype of the proposed structure. (a) Front side. (b) Rear side.

On the other hand, the proposed structure has smaller number of turns on the outer legs than the conventional structure under the same total wire length. Therefore, the proposed structure has a drawback that its equivalent CM inductor has a smaller number of turns than the conventional structure. This indicates that the proposed structure requires smaller R_O in order to keep the same CM inductance as the conventional structure.

If reducing R_O inevitably requires for expanding the cross-section of the outer legs, for example when we cannot employ a core material with higher permeability, the proposed structure may not lead to effective reduction in the core volume. However, the proposed structure can offer effective core reduction in other conditions, for example when designing necessary tolerance to the DC flux determines the cross-sectional area rather than designing necessary value for R_O. We present a case study to estimate the core reduction effect under this condition in Section 5.4.

5. 3. Experiments

The purpose of this section is to confirm experimentally the operating principles of the proposed structure. The experiment evaluated the following two subjects. One is the functional equivalence of the proposed structure to the discrete DM and CM inductors. The other is miniaturization of the discrete inductors by the magnetic integration using the proposed structure.

A. Prototypes

We developed two prototypes providing the DM and CM inductance under the same requirement specifications presented in Table 5.1. One is the proposed structure; and the other is the series-connected discrete DM and CM inductors. These specifications were designed as a part of an input filter of a PFC converter, whose maximum input AC current was set at 16Arms. In this application, the input current has the frequency far lower than

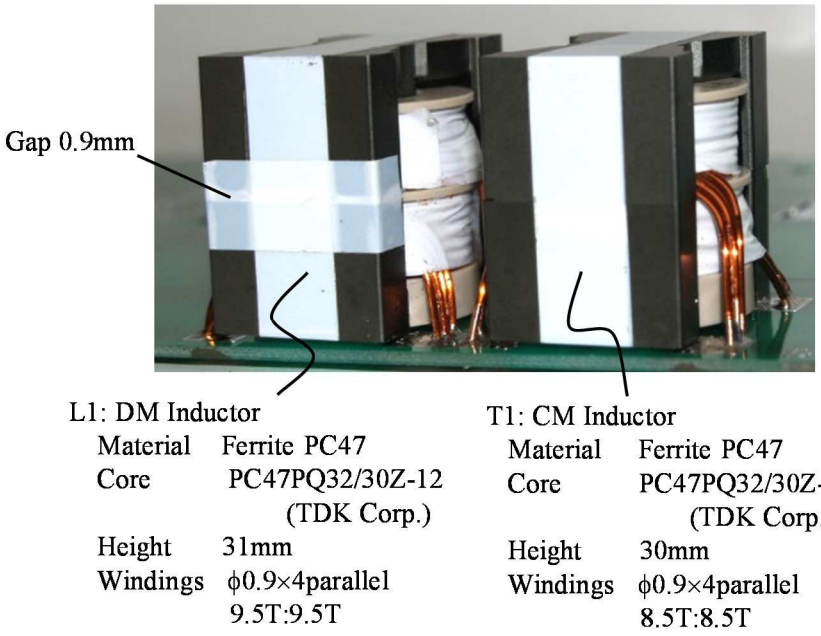

Fig. 5.6. Photograph of the prototype of the discrete inductors.

the DM noise. Hence, the input current can be regarded as the DC component in the DM current. We specified the DM and CM inductance at the instantaneous input current of 16A. In addition, we required the saturation current of the DM and CM inductance to be greater than the maximum instantaneous input current, i.e. 22.5A.

Both prototypes were made of ferrite cores with similar permeability and saturation flux density. The prototype of the proposed structure is made of PC40 (TDK Corporation), whereas that of the discrete inductors is made of PC47 (TDK Corporation). PC40 and PC47 have the typical relative permeability of 2300 and 2400, respectively; and they have the saturation flux density of 510mT and 530mT, respectively. We designed these prototypes to have the same vertical dimension and the same average height so that the horizontal dimension reflects the volume.

Figure 5.4 illustrates the physical structure of the prototype of the proposed structure. In the prototype, we placed the flattened center leg in the front side and the outer legs in the rear side. This disposition is beneficial in enhancing the CM inductance by minimizing flux path length through the two outer legs. Additionally, for easy assembly, we installed two gaps in the top and bottom beams near the center leg, respectively, to provide the reluctance R_C (corresponding to the gap on the center leg in Fig. 5.1). Contrarily, we installed no gap on the outer legs. The photographs of the prototype are presented in Fig. 5.5.

The cross-sectional area of the center leg was designed so that the maximum instantaneous input current approximately induces the saturation flux density there. Meanwhile, we designed the cross-sectional area of the outer leg 1.19 times as great as that of the center leg. Because the DC flux in the outer leg is half of that in the center leg, the DC flux density in the outer leg does not exceed 42% of the saturation flux density. Hence, the outer leg was designed with sufficient margin of the DC flux to suppress the CM inductance decrease.

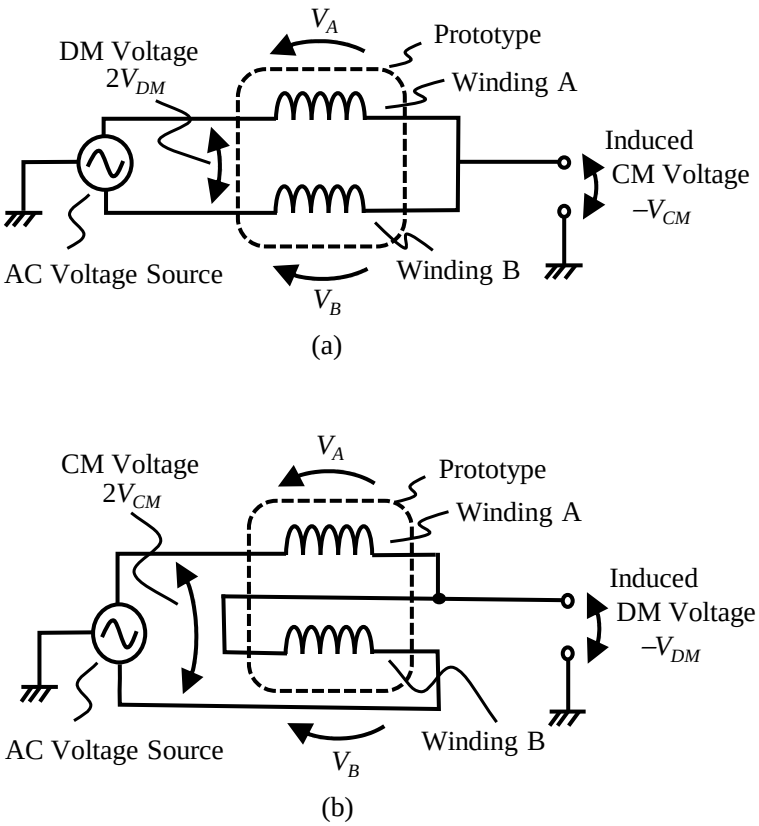

Fig. 5.7. Evaluation circuits of the conversion ratios between DM and CM noise. (a) Evaluation of CM noise response to DM noise excitation. (b) Evaluation of DM noise response to CM noise excitation.

On the other hand, the prototype of the discrete inductors was made of two basic PQ cores, as shown in Fig. 5.6. We designed wire of their windings to have the similar cross-sectional area as the prototype of the proposed structure. In addition, we designed this prototype to have similar DC resistance as the prototype of the proposed structure, as shown in Table 5.1.

B. Functional Equivalence between the Prototypes

We confirmed that the proposed structure is functionally equivalent to series-connected discrete inductors by evaluating conversion ratios between DM and CM noise, i.e. CM voltage response to DM noise excitation and DM voltage response to CM noise excitation. The conversion ratios must vanish in series-connected ideal DM and CM inductors. Hence, we need to verify that the prototype of the proposed structure shows as small conversion ratios as the prototype of the discrete inductors.

Evaluation circuits of the conversion ratios are presented in Fig. 5.7. We connected the windings A and B in series as shown in Fig. 5.7(a) and Fig. 5.7(b). Then, we applied AC voltage signal with the amplitude of ±5Vpeak to the series-connected windings.

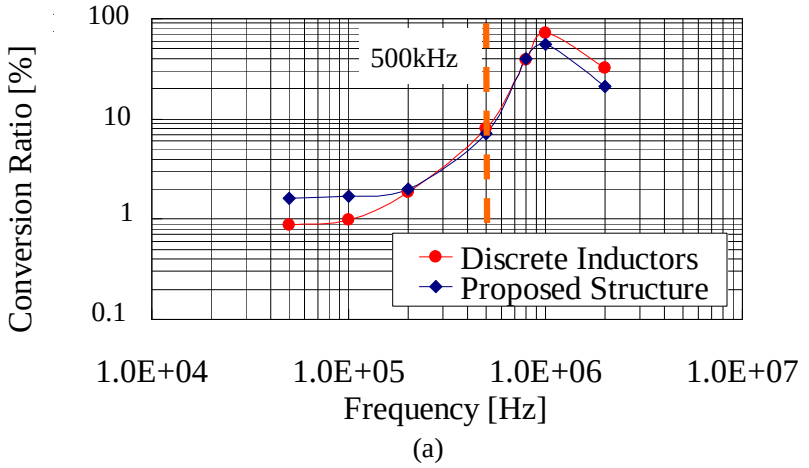

(a)

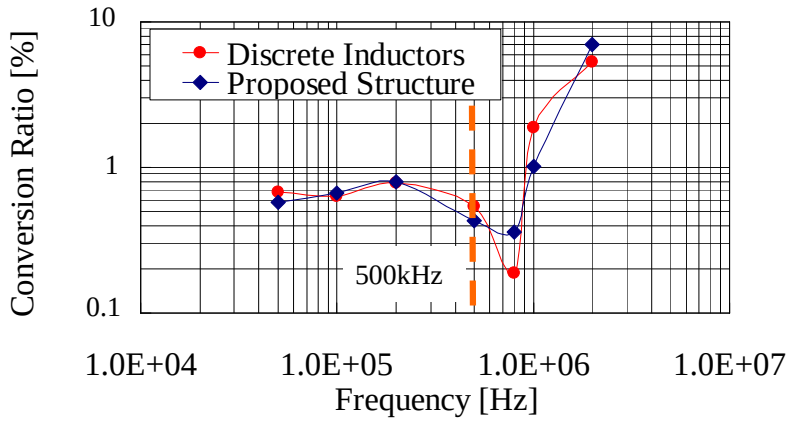

(b)

Fig. 5.8. Measured conversion ratios. (a) Ratio of CM noise response to DM noise excitation. (b) Ratio of DM noise response to CM noise excitation.

Now, we express the voltage induced in each winding using the DM voltage V_{DM} and the CM voltage V_{CM}. If we denote the induced voltage in the winding A and B as V_A and V_B, respectively, we have

$$\begin{cases} V_A = V_{CM} + V_{DM}, \\ V_B = V_{CM} - V_{DM}. \end{cases} \tag{5.8}$$

Note that the AC signal voltage corresponds to $V_A - V_B$, i.e. $2V_{DM}$, in Fig. 5.7(a) and to $V_A + V_B$, i.e. $2V_{CM}$, in Fig. 5.7(b). Hence, the AC signal is a DM voltage source that excites DM noise current in Fig. 5.7(a) and a CM voltage source that excites CM noise current in Fig. 5.7(b).

We connected the midpoint between the terminals of the AC signal to the ground. Then, we measured the voltage potential at the connecting point of the windings A and B. The measured voltage represents the CM voltage response $-V_{CM}$ in Fig 5.7(a) and the DM voltage response $-V_{DM}$ in Fig. 5.7(b). We obtained the conversion ratios by normalizing

the amplitude of the measured voltage by half the amplitude of the AC signal voltage. The normalized voltage in Fig. 5.7(a) corresponds to the ratio of CM noise response to DM noise excitation, and that in Fig. 5.7(b) corresponds to the ratio of DM noise response to CM noise excitation.

We examined the conversion ratios in the frequency range below 500kHz because the dimensional resonance may deteriorate the soft-magnetic property of the ferrite core above the frequency. Figure 5.8 shows the results. The ratios of the proposed structure were found approximately as small as those of the discrete inductors. Both the prototypes showed the ratio of CM noise response smaller than 7% and the ratio of DM noise response smaller than 1% below 500kHz.

Consequently, we concluded that the two prototypes are approximately equivalent each to the other in their electrical functions, as expected from the theory.

C. DM and CM Filtering Capability

Next, we confirmed that the two prototypes have similar filtering capability by evaluating the DM and CM inductance as well as the DM and CM saturation current. The evaluation methods are as follows.

Figure 5.9 illustrates the evaluation circuit of the DM inductance and the DM saturation current. The windings A and B were connected in series in a similar manner as in Fig. 5.7(a). Therefore, DM voltage was applied to the prototype during the on-state of the switch S1. We held S1 in the on-state until the DM current sufficiently saturated the prototype. At the same time, we measured the applied voltage V_{COIL} and the DM current I_{COIL}. The current I_{COIL} increased monotonically during the on-state of S1 as illustrated in Fig. 5.9(b). Hence, we obtained the DM inductance L_{DM} as the differential inductance [12] defined by

$$L_{DM} = \frac{V_{COIL}}{dI_{COIL}/dt}, \tag{5.9}$$

where t is the time. The DM inductance L_{DM} can be obtained as a function of I_{COIL}. The DM saturation current is the DM current I_{COIL} when L_{DM} decreases to 75% of its value at I_{COIL}=0A.

The method to evaluate the CM inductance is slightly more complicated than the method for the DM inductance. Figure 5.10(a) illustrates the evaluation circuit. In this experiment, we further connected the capacitor C1 with the capacitance of 1nF between the ground and the connecting point of the windings A and B. Then, we held the switch S1 in the on-state until the DM current increased to the predetermined level I_{DC} as illustrated in Fig. 5.10(b). After the turn-off of S1, the DM current circulated through the diode D1. The circulating DM current maintained itself for a while because no DM voltage was applied to the prototype.

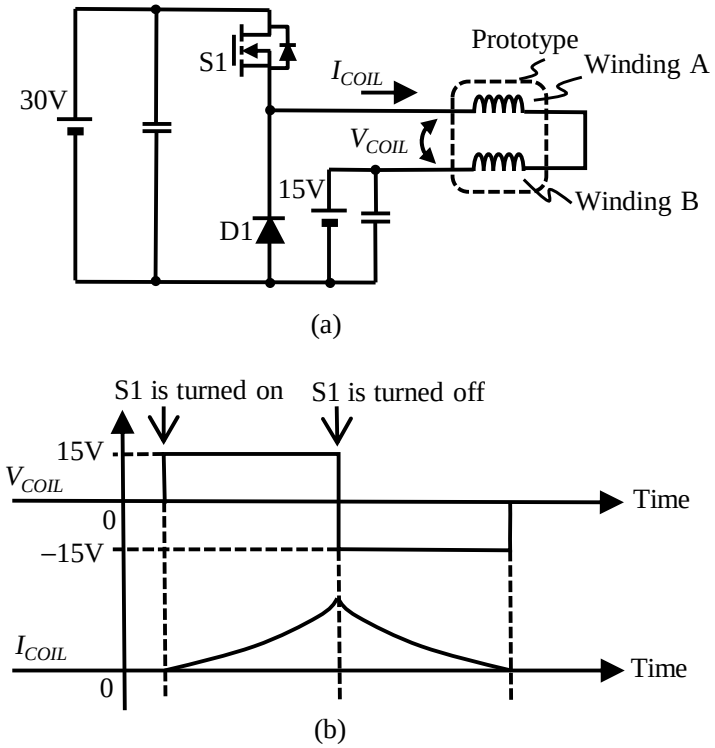

Fig. 5.9. Method to evaluate the DM inductance and the DM saturation current. (a) Evaluation circuit. (b) Voltage and current waveforms in the evaluation process.

At the same time, an LC oscillation occurred between the capacitor C1 and the prototype. This oscillation was excited at the turn-off of S1, because the voltage V_C of the capacitor C1 was approximately half of the supply voltage of 15V at the turn-off of S1 and then V_C was going to settle finally to zero as the oscillation was dissipated. As a result, the voltage and current waveforms can be illustrated as Fig. 5.10(b). Note that the voltage V_C equals to the CM voltage V_{CM} of the prototype when the DM current circulates through D1. Therefore, this oscillation corresponds to the LC oscillation between C1 and the CM inductance L_{CM} of the prototype. Hence, we obtained L_{CM} according to

$$L_{CM} = \frac{1}{C_1 \omega_{OSC}^{\ 2}}, \tag{5.10}$$

where C_1 is the capacitance of C1 and ω_{OSC} is the angular frequency of the oscillation. The CM inductance L_{CM} can be obtained as a function of I_{DC} by determining L_{CM} at various levels of I_{DC}. The CM saturation current is the DM current I_{DC} when L_{CM} decreases to 75% of its value at I_{DC}=0A.

The measurement results of L_{DM} and L_{CM} are presented in Fig. 5.11. As summarized in Table 5.1, evaluation results of both the prototypes met the requirement specifications. They showed approximately the same DM and CM inductance. On the other hand, the proposed structure showed slightly better DM saturation current than the discrete inductors. As for saturation of the CM inductance, only the proposed structure has the

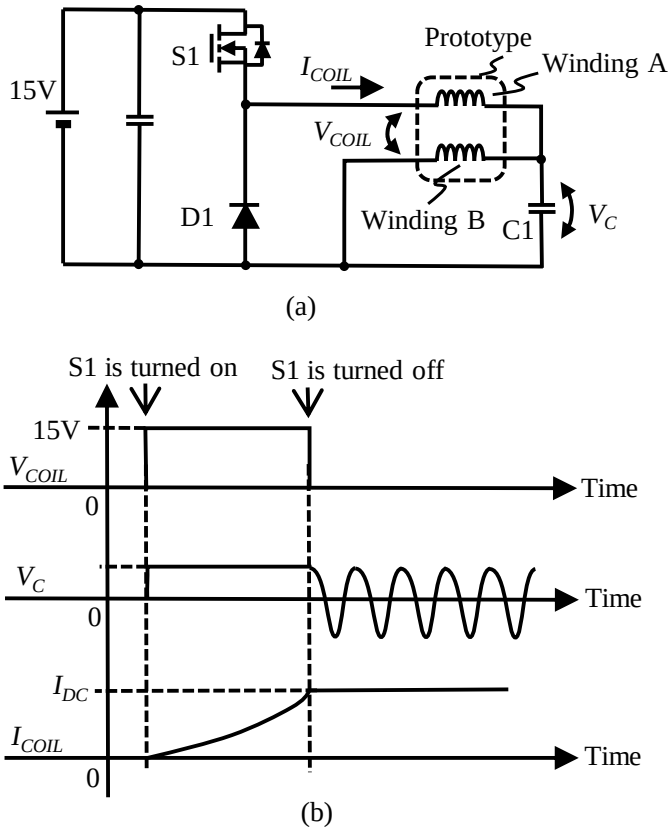

Fig. 5.10. Method to evaluate the CM inductance and the CM saturation current. (a) Evaluation circuit. (b) Voltage and current waveforms in the evaluation process.

saturation current because the discrete CM inductor does not saturate by the DM current. Nonetheless, the proposed structure showed CM saturation current far above the requirement specification.

Consequently, the prototypes are confirmed to have similar filtering capability.

D. Comparison of the Volume

Finally, we compared the volume between the prototypes. The result is shown in Fig. 5.12. Because the prototypes have the same vertical dimension and the same average height, the horizontal dimension reflects the total volume including the dead space. Comparing the horizontal dimension between the prototypes, we found that the proposed structure reduced the total volume by 31%.

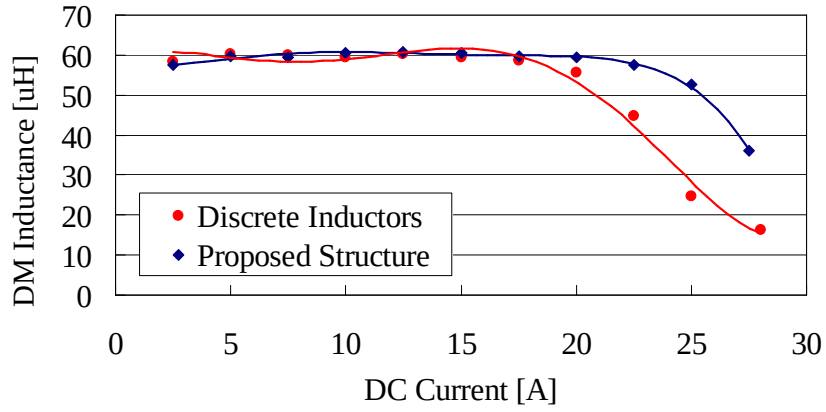

(a)

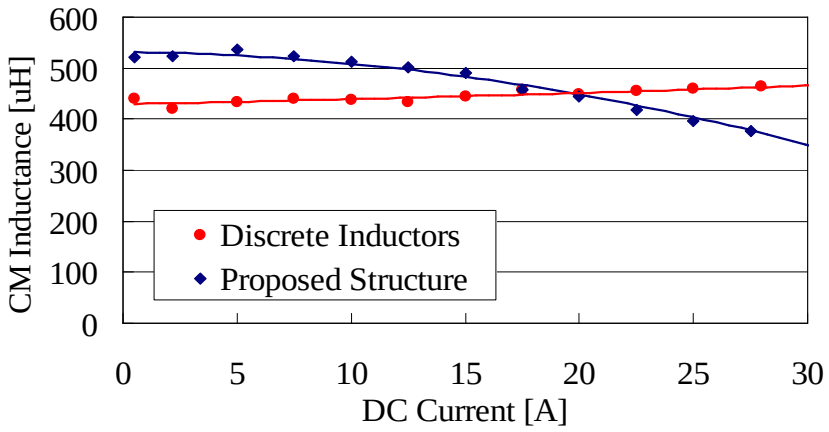

(b)

Fig. 5.11. Measurement results of (a) the DM inductance L_{DM} and (b) the CM inductance L_{CM}.

This reduction effect was contributed not only by eliminating dead space but also by reducing the core. According to comparison of the net core volume, we found that the proposed structure also reduced the core volume by 17%. Consequently, we concluded that the proposed structure successfully miniaturized the discrete inductors.

5. 4. Core Reduction Effect of Suppressing DC Flux

This section analytically estimates the core reduction effect of the proposed structure in comparison with the conventional structure shown in Fig. 5.1(b). For this purpose, we estimates the core dimensions of the conventional structure, when the same specifications as Table 5.1 is applied and the same physical core structure as Fig. 5.4 is employed. We determine the core dimensions of the conventional structure by modifying the prototype of the proposed structure discussed in the previous section. Then, we compare the core volume between the estimated conventional structure and the prototype of the proposed structure.

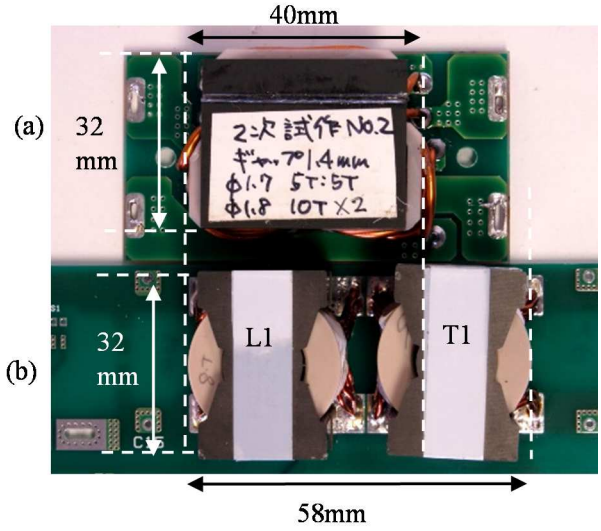

Fig. 5.12. Comparison of the volume between the prototypes. (a) Proposed structure. (b) Discrete inductors.

When estimating the conventional structure, we set the total wire length the same as the prototype of the proposed structure. Hence, the DC resistance can be kept the same without expanding the cross-section of the wire. On the other hand, we expand the cross-section of magnetic paths to keep the DM and CM saturation current the same as the prototype of the proposed structure. For convenience, we assume the same cross-sectional shapes of the center and outer legs as the prototype of the proposed structure, when we expand the cross-section. In addition, we adjust R_C and R_O to keep the DM and CM inductance the same as the prototype of the proposed structure. When we adjust R_O, we change the permeability of the core material while keeping the saturation flux density unchanged. As for adjusting R_C, we assume that reluctance of the air gaps mainly contributes R_C and we adjust the gap length to obtain appropriate value for R_C.

In the first step, we compose the conventional structure directly on the magnetic core employed in the prototype of the proposed structure. Because the total wire length is kept unchanged, this conventional structure has the outer leg windings with the number of turns N_{O_temp} set at 16.

Next, we expand the cross-section of the magnetic core. We assume to enlarge the cross-sectional area of the outer leg by a factor α. Then, the number of turns N_{O_mod} of the outer leg windings after this modification should be changed according to (5.11) because the perimeter of the cross-section is expanded by $\sqrt{\alpha}$.

$$N_{O\_mod} = N_{O\_temp} \Big/ \sqrt{\alpha} = 16 \Big/ \sqrt{\alpha}. \tag{5.11}$$

In order to estimate α that provides the same CM saturation current as the proposed structure, we consider the DC flux in ϕ_2 when the DC component in the DM current equals to the CM saturation current. We denote the DC flux in the expanded core at the CM saturation current as ϕ_{2_mod}, and that in the prototype of the proposed structure as ϕ_{2_org}.

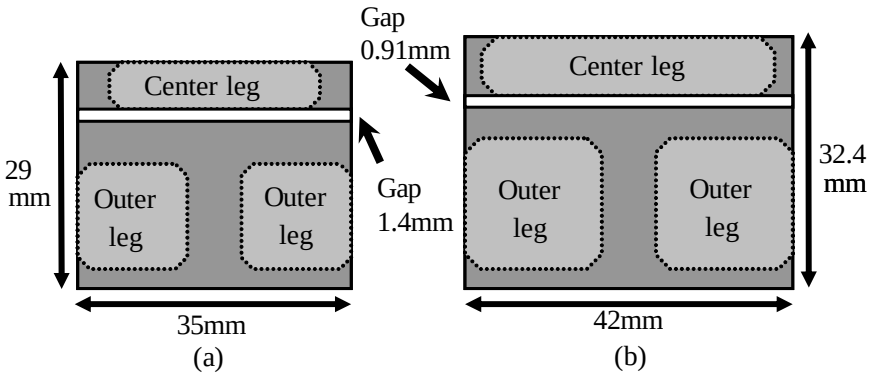

Fig. 5.13. Top view of (a) the core in the prototype of the proposed structure and (b) the estimated core of the conventional structure. The solid lines illustrate the outline of the top beam core; and the dotted lines illustrate the outline of the center and outer legs.

Because we require the same DM inductance L_{DM} and the same CM saturation current, we have the following relation according to (5.2) and Fig. 5.3:

$$\frac{\phi_{2\_mod}}{\phi_{2\_org}} = \frac{2N_{C\_org} + N_{O\_org}}{N_{O\_mod}} = \frac{20}{N_{O\_mod}}, \tag{5.12}$$

where N_{C_org} and N_{O_org} are the numbers of turns of the center leg windings and the outer leg windings in the prototype of the proposed structure, respectively.

Because the reluctance R_O determines the CM inductance, increase rate of R_O at the CM saturation current must be the same as the prototype of the proposed structure in order to accomplish the same CM saturation current. Accordingly, the DC flux density in the outer legs at the CM saturation current must be designed to be the same as the prototype of the proposed structure. Hence, we have

$$\alpha = \frac{\phi_{2\_mod}}{\phi_{2\_org}}. \tag{5.13}$$

Equations (5.11)–(5.13) determine α and N_{O_mod}:

$$\alpha \approx 1.56, \quad N_{O\_mod} \approx 13. \tag{5.14}$$

The DC flux density in the center leg at the DM saturation current must also be designed to be the same as the prototype of the proposed structure in order to accomplish the same DM saturation current. As a result, we also need to expand the cross-section of the center leg by α, according to similar discussion to obtain (5.13). In addition, we need to expand the cross-section of the top and bottom beams by α because the DC flux also flows through the beams.

The above discussion also determines the gap length at the top and bottom beams of the estimated core of the conventional structure. Let l_{g_mod} and l_{g_org} be the gap length of

the estimated core and the proposed structure, respectively. Applying Ampere's law to the closed flux path passing through the center leg and one of the outer legs, we obtain the following equation:

$$2\frac{B_{sat}}{\mu_g} l_{g\_org} = \left(2N_{C\_org} + N_{O\_org}\right) I_{sat}, \tag{5.15}$$

$$2\frac{B_{sat}}{\mu_g} l_{g\_mod} = N_{O\_mod} I_{sat}, \tag{5.16}$$

where B_{sat} is the DC flux density at the DM saturation current I_{sat}, and μ_g is the absolute permeability of the gap material. From (5.15) and (5.16), we obtain:

$$\frac{l_{g\_mod}}{l_{g\_org}} = \frac{N_{O\_mod}}{2N_{C\_org} + N_{O\_org}} = \frac{13}{20}. \tag{5.17}$$

Substituting l_{g_org}=0.0014m into (5.17), we obtain l_{g_mod}:

$$l_{g\_mod} \approx 0.00091. \tag{5.18}$$

Finally, we obtain the estimation result of the core dimensions as shown in Fig. 5.13. If we assume the height of the legs the same as the prototype of the proposed structure, the net core volume of the conventional structure is estimated as 3.5×10^4mm^3. On the other hand, the net core volume of the proposed structure is 2.0×10^4mm^3. Consequently, the proposed structure is found to reduce the core volume by 41% compared to the conventional structure.

5. 5. Conclusions

The magnetic integration is an attractive technique to miniaturize EMC filters. Prior works have reported EMC filters that applied this technique to integrate a DM inductor and a CM inductor. However, the conventional magnetic structure employed in these works can often suffer from the magnetic saturation of the DM or CM inductance, because the equivalent number of turns for the DM inductance is restricted to only half of the total number of turns and it can be insufficient to suppress DC flux induction. This may lead to expanding the cross-section of magnetic paths to ensure necessary tolerance to the magnetic saturation, thus hindering the miniaturization effect of the magnetic integration.

To address the problem, this chapter proposed a novel structure that allows assigning more turns to the DM inductance than the conventional structure. We confirmed that the proposed structure is equivalent to series-connected discrete DM and CM inductors both theoretically and experimentally. Furthermore, we confirmed experimentally that the proposed structure can miniaturize the discrete DM and CM inductors.

An analytical estimation was carried out to evaluate core reduction effect of the proposed structure in comparison with the conventional structure. The result revealed that the proposed structure reduced the core volume by 41% under the same total wire length and under the same specifications, in which saturation by the DC flux is a determining factor in the cross-sectional area of magnetic paths.

These results demonstrate effectiveness of the proposed structure for miniaturizing EMC filters.

REFERENCES

[1] R. Chen, J. D. van Wyk, S. Wang, and W. G. Odentaal, "Technologies and characteristics of the integrated EMI filters for switch mode power supplies," in *Proc. IEEE Power Electron. Specialist Conf. (PESC)*, Aachen, Germany, 2004, vol. 4, pp. 4873-4880.

[2] R. Chen, J. D. van Wyk, S. Wang, and W. G. Odentaal, "Improving the characteristics of integrated EMI filters by embedded conductive layers," *IEEE Trans. Power Electron.*, vol. 20, no. 3, pp. 611-619, May 2005.

[3] J. Biela, A. Wirthmueller, R. Waespe, M. L. Heldwein, K. Raggl, and J. W. Kolar, "Passive and active hybrid integrated EMI filters," *IEEE Trans. Power Electron.*, vol. 24, no. 5, pp. 1340-1349, May 2009.

[4] X. Wu, D. Xu, Z. Wen, Y. Okuma, and K. Mino, "Design, modeling, and improvement of integrated EMI filter with flexible multilayer foils," *IEEE Trans. Power Electron.*, vol. 26, no. 5, pp. 1344-1354, May 2011.

[5] P. Boonma, V. Tarateeraseth, and W. Khan-ngern, "A new technique of integrated EMI inductor using optimizing inductor-volume approach," in *Proc. Int. Power Electron. Conf. (IPEC)*, Niigata, Japan, 2005.

[6] L. Nan and Y. Yugang, "A common mode and differential mode integrated EMI filter," in *Proc. IEEE Intl. Power Electron. Motion Control Conf. (IPEMC)*, Shanghia, China, 2006, vol. 1, pp. 1-5.

[7] R. Lai, Y. Maillet, F. Wang, S. Wang, R. Burgos, and D. Boroyevich, "An integrated EMI choke for differential-mode and common-mode noise suppression," *IEEE Trans. Power Electron.*, vol. 25, no. 3, pp. 539-544, Mar. 2010.

[8] W. Tan, C. Cuellar, X. Margueron, and N. Idir, "A common-mode choke using troid-EQ mixed structure," *IEEE Trans. Power Electron.*, vol. 28, no. 1, pp. 31-35, Jan. 2013.

[9] A. K. Upadhyay, "Integrated common mode and differential mode inductor device," U.S. Patent 5 313 176, May 17 1994.

[10] T. P. Gilmore and G. Ray, "Method of configuring common mode/ differential mode choke," U.S. Patent 6 768 408 B2, Jul. 27 2004.

[11] F. Luo, D. Boroyevich, P. Mattevelli, K. Ngo, D. Gilham, and N. Gazel, "An integrated common mode and differential mode choke for EMI suppression using magnetic epoxy mixture," in *Proc. IEEE Appl. Power Electron. Conf. Expo.*, 2011, pp. 1715-1720.

[12] A. Van den Bossche, and V. C. Valchev, "Fundamentals of magnetic theory," in *Inductors and transformers for power electronics*, Florida: CRC Press, 2005, pp. 17-29.

[13] L. D. Landau and E. M. Lifshitz, “Canonical tranformations” in *Mechanics*, Oxford, U. K.: Butterworth- Heinemann, 1976, pp.143-146.

Chapter 6

UNIDIRECTIONAL BOOST CHOPPER WITH SNUBBER ENERGY REGENERATION USING AN INTEGRATED MAGNETIC COMPONENT

6. 1. Introduction

Recently, growing awareness of environmental protection gives rises to public concern to vehicles with less environmental burden, such as Electric Vehicles (EVs), Hybrid Vehicles (HVs), and Fuel Cell Vehicles (FCVs).

These vehicles are propelled by electric motors. The motors are driven by inverters, which convert DC power from battery into AC power. When the vehicles travel at high speed, the inverters need to provide large amplitude of AC voltage to the motors in order to overcome large induction of the counter electromotive force. Consequently, the inverters often require high DC voltage supply. For this reason, some practical propulsion systems equip boost choppers between the batteries and the inverters [1][2].

However, the additional boost choppers tend to lower the conversion efficiency. Moreover, there are risks that the resulting increase of energy loss may overload the limited cooling capability of the vehicle. Therefore, the choppers need to improve their efficiency.

As widely known, the soft-switching technique is a useful remedy for the purpose. Various circuits have been reported in the proceeding works [3]–[21]. However, their application to vehicular propulsion generally seems to be impeded by the fact that the load of the chopper, along with the output voltage, varies largely according to traveling conditions. Particularly, the following four difficulties can be listed as the probable reason.

First, some circuit topologies tend to suffer from a limitation on soft-switching capability in some operating conditions, as reported in the works [3][4]. This possibly results in considerable decrease of efficiency under certain driving conditions. Thus, a soft-switching circuit is preferably capable of soft-switching regardless of the input-output voltage relation and the operating modes, such as the continuous or the discontinuous conduction mode.

Second, some circuit topologies tend to need high computational capability or large-sized memory for implementing soft-switching control. For example, many circuits, as reported in the works [5]–[10], utilize LC oscillation as the mechanism to achieve soft-switching. In such cases, the soft-switching control may require calculation of trigonometric functions or reference to large-sized table in order to find optimal timing

† Reprinted, with permission, from K. Umetani, F. Iwamoto, and K. Yagyu, A unidirectional boost chopper with snubber energy regeneration using a coupled inductor, IEEJ Transactions on Electrical and Electronic Engineering, May 2014.

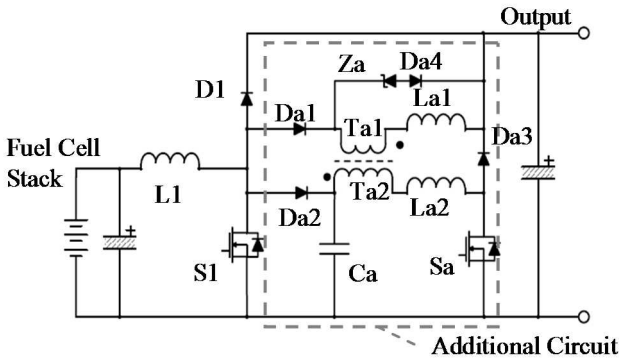

Fig. 6.1. Proposed boost chopper.

for the switching to coincide with the oscillation. Thus, a soft-switching circuit is preferably controlled by a simple algorithm composed of basic calculations as arithmetic operations.

Third, some circuit topologies tend to suffer from large cost-up due to additional switches for implementing soft-switching function. For example, many circuits, including those reported in the works [11]–[17], have one or more additional switches, which conduct the inductor current to an alternative current path during switching operation of the main switches. Consequently, current rating of the additional switches is designed to tolerate maximum inductor current of all possible operations. If the range of load power is large, as is often the cases in vehicular propulsion, the additional switches may contribute the cost-up significantly due to their large current rating.

Certainly, there is a soft-switching technique [18][19] in which this drawback is alleviated by utilizing a transformer. In this technique the additional switch can be designed to conduct smaller current than the inductor current. However, the switch still needs to conduct at least half of the inductor current. Thus, a soft-switching circuit is preferably implemented by fewest additional switches and they preferably conduct far smaller current than the inductor current.

Fourth, some circuit topologies require additional voltage or current stress on the main switch of the boost chopper. For example, the circuits proposed in the works [20][21] are beneficial in meeting all the first three preferable points. However, their main switch inevitably conducts greater current than the inductor current momentarily after their turn on. As a result, these techniques may require greater current rating for the main switch in order to tolerate the additional current stress under the momentary heavy load during sudden acceleration of vehicle. Thus, a soft-switching circuit is preferably free from additional stress on the main switch.

Solving the above mentioned difficulties possibly helps the soft-switching technique to be applied in practical vehicular choppers. Nevertheless, we have few candidates that meet all the preferable points so far. The purpose of this chapter is to propose a soft-switching unidirectional boost chopper as a candidate for a propulsion system of FCVs. In addition to solving the above mentioned difficulties, the proposed converter further reduces the circuit volume by integrating the magnetic components in the auxiliary circuit into an integrated magnetic component.

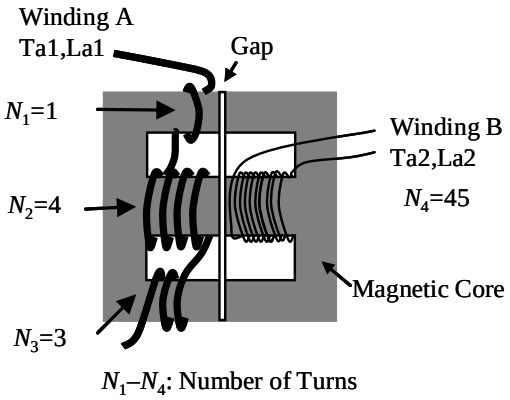

Fig. 6.2. An example of implementing Ta1, Ta2, La1, and La2 by a single magnetic core and two windings.

Section 6.2 presents the proposed circuit and explains its circuit behavior. Section 6.2 also presents the integrated magnetic component employed in the proposed converter. Section 6.3 discusses the soft-switching control. Section 6.4 then presents experimental results to confirm soft-switching operation and efficiency improvement.

6. 2. Proposed Chopper

A. Circuit Overview

The proposed unidirectional chopper is presented in Fig. 6.1. The circuit is composed of the basic chopper made of the main switch S1 and the main diode D1, and an additional circuit surrounded by the dotted line. The circuit diagram is similar to the previously reported technique [18][19]. However, the additional circuit enables S1 to achieve Zero-Current Switching (ZCS) at the turn on instead of Zero-Voltage Switching (ZVS). As for the turn off, it enables S1 to achieve ZVS. The auxiliary switch Sa also achieves ZCS at the turn on. Contrarily, Sa is not capable of soft-switching at the turn off. Nonetheless, its turn-off loss is generally ignorable compared to reduction of the switching loss of S1, because it conducts far less current than S1 does, as shown later.

The additional circuit contains magnetic devices expressed by an equivalent circuit of Ta1 (Ta2), La1, and La2. Ta1 and Ta2 are windings of a coupled inductor. Contrary to the preceding technique [18][19], in which Ta1 should have the larger winding turn number than Ta2, the proposed circuit allow Ta2 to have far larger turn number than Ta1, enabling small current in Ta2 suffice to induce far larger current in Ta1. The devices La1 and La2 are inductors. The inductor La1 is indispensable for soft-switching operation. On the other hand, La2 is not necessary for the circuit function. However, it is implemented naturally as leakage inductance of Ta2 in many cases because Ta2 tends to have a large number of turns and thus it is generally made of thin wire.

The inductors Ta1 (Ta2), La1, and La2 are able to be implemented on a single magnetic core, as shown in Fig. 6.2. The two windings A and B on a pair of E cores suffice to accomplish the circuit function of all the three inductors. The coupled inductor Ta1 (Ta2)

is implemented at the center leg, where the windings A and B are magnetically coupled each to the other. The inductor La1 is implemented by the windings at the outer legs, along with the leakage inductance of the winding A. The inductor La2 is the leakage inductance of the winding B. In the next subsection, we present the detailed demonstration that the magnetic device shown in Fig. 6.2 is equivalent to Ta1 (Ta2), La1, and La2 by means of the Lagrangian dynamics.

B. Equivalency of Integrated Magnetic Component

As shown in Chapter 2, Lagrangian dynamics can be utilized to transform a complicated magnetic circuit into an equivalent electric circuit. Here, we apply the method to the integrated magnetic component illustrated in Fig. 6.2.

First, we describe magnetic structure of the component as a magnetic circuit model of electromotive force and reluctance. The model is presented in Fig. 6.3(a). Each electromotive force corresponds to a winding on a magnetic path. We denote the number of turns by N_1–N_4. Additionally, we denote the electric current in the winding A and B by $\dot{q}_1$ and $\dot{q}_2$, respectively.

The reluctance R_{G1} represents the reluctance of gaps and core of outer legs, while R_{G2} represents that of center leg. We assume, for convenience, that the two outer legs have the same reluctance. Leakage magnetic paths of the windings are implemented as the reluctance R_{L1}–R_{L4}. The fluxes that flow through R_{G1}, R_{G2}, and $R_{L1–4}$ are denoted as $\phi_{1–3}$ and $\phi_{L1–4}$.

The Lagrangian L that belongs to Fig. 6.3(a) is expressed by the following equation:

$$\begin{aligned} L = {} & N_1\dot{q}_1(\phi_1 - \phi_{L1}) + N_2\dot{q}_1(\phi_2 - \phi_{L2}) - N_3\dot{q}_1(\phi_3 - \phi_{L3}) - N_4\dot{q}_2(\phi_2 - \phi_{L4}) \\ & - \frac{1}{2}R_{G1}\phi_1^{\,2} - \frac{1}{2}R_{G2}\phi_2^{\,2} - \frac{1}{2}R_{G1}\phi_3^{\,2} - \frac{1}{2}R_{L1}\phi_{L1}^{\,2} - \frac{1}{2}R_{L2}\phi_{L2}^{\,2} \\ & - \frac{1}{2}R_{L3}\phi_{L3}^{\,2} - \frac{1}{2}R_{L4}\phi_{L4}^{\,2} + \lambda(\phi_1 + \phi_2 + \phi_3), \end{aligned} \tag{6.1}$$

where λ is a Lagrangian multiplier.

As a Lagrangian multiplier is an ignorable variable [22], the Lagrangian multiplier term can be eliminated by substituting (6.2) into (6.1).

$$\phi_1 + \phi_2 + \phi_3 = 0. \tag{6.2}$$

As a result, we obtain:

$$\begin{aligned} L = {} & N_1\dot{q}_1(\phi_1 - \phi_{L1}) + N_2\dot{q}_1(\phi_2 - \phi_{L2}) + N_3\dot{q}_1(\phi_1 + \phi_2 + \phi_{L3}) \\ & - N_4\dot{q}_2(\phi_2 - \phi_{L4}) - \frac{1}{2}R_{G1}\phi_1^{\,2} - \frac{1}{2}R_{G2}\phi_2^{\,2} - \frac{1}{2}R_{G1}(\phi_1 + \phi_2)^2 - \sum_{i=1}^{4}\frac{1}{2}R_{Li}\phi_{Li}^{\,2}. \end{aligned} \tag{6.3}$$

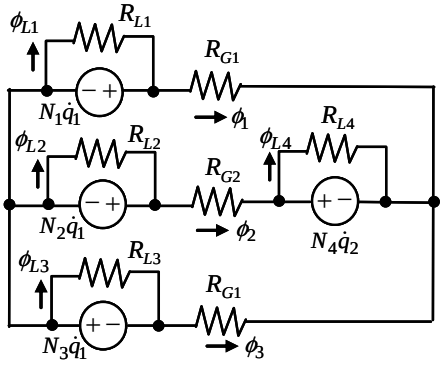

R_{L1-3}: Reluctance of Leakage Flux Path

R_{G1-2}: Reluctance of Gap and Core

$\dot{q}_1, \dot{q}_2$: Electric Current of Winding A and B

(a)

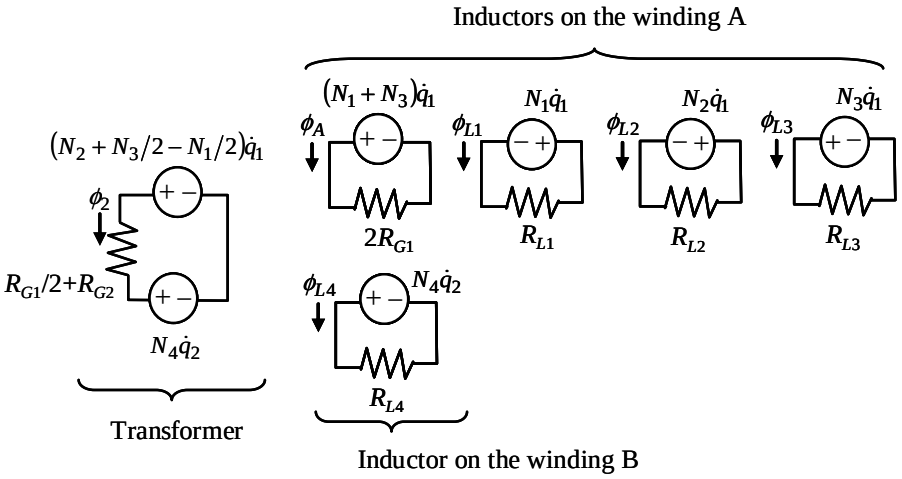

(b)

Fig. 6.3. Magnetic model of the integrated magnetic component and magnetic devices in its equivalent circuit. (a) Original integrated magnetic component. (b) Equivalent circuit.

Then, we introduce fluxes ϕ_A defined as follows:

$$\phi_A \equiv \phi_1 + \frac{1}{2}\phi_2 . \tag{6.4}$$

Now, we substitute (6.4) into (6.3). The result is obtained as follows:

$$L = \left\{ \left(N_2 + \frac{N_3 - N_1}{2} \right) \dot{q}_1 - N_4 \dot{q}_2 \right\} \phi_2 - \frac{1}{2} \left\{ \frac{R_{G1}}{2} + R_{G2} \right\} {\phi_2}^2$$

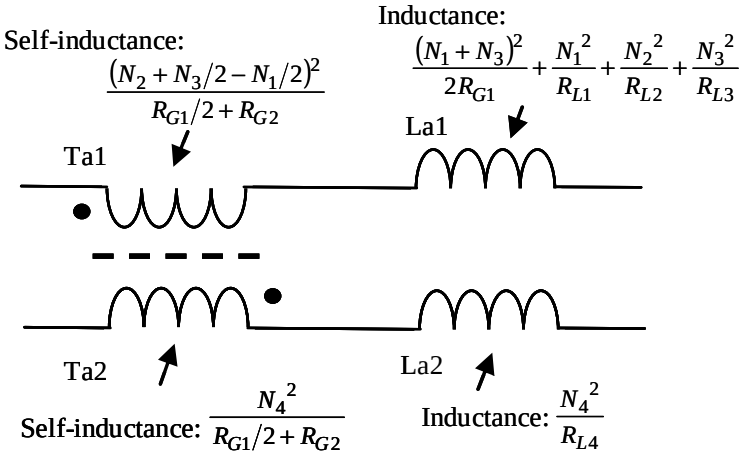

Fig. 6.4. Electric circuit translated from (6.5)

$$+(N_1+N_3)\dot{q}_1\phi_A - R_{G1}{\phi_A}^2 + N_3\dot{q}_1\phi_{L3} - \frac{1}{2}R_{L3}{\phi_{L3}}^2$$

$$- N_1\dot{q}_1\phi_{L1} - \frac{1}{2}R_{L1}{\phi_{L1}}^2 - N_2\dot{q}_1\phi_{L2} - \frac{1}{2}R_{L2}{\phi_{L2}}^2 + N_4\dot{q}_2\phi_{L4} - \frac{1}{2}R_{L4}{\phi_{L4}}^2. \qquad (6.5)$$

The Lagrangian given by (6.5) corresponds to an electric circuit that consists of basic magnetic devices, such as ideal transformers and inductors. The magnetic circuits translated from the Lagrangian are presented in app. Fig. 6.3(b). Note that the four inductors that consist of fluxes ϕ_A and ϕ_{L1}-ϕ_{L3} have windings that share the same electric current, i.e. they are connected in series. Thus, we can replace them by a single inductor whose inductance equals the sum of their inductance.

Consequently, we finally obtain the equivalent electric circuit presented in Fig. 6.4. The result indicates that the integrated magnetic component shown in Fig. 6.2 implements Ta1(Ta2), La1 and La2 of the proposed chopper.

C. Circuit Behavior

This subsection discusses the circuit behavior under the continuous conduction mode. The voltage and current waveforms are illustrated in Fig. 6.5; and the schematic illustration of current flow in each operating mode is shown in Fig. 6.6.

In Mode 1, the proposed chopper operates the same as the basic chopper. The main switch S1 is in the off-state and the current of L1 flows into the output terminal through the diode D1. Then, in Mode 2, Sa is turned on. The turn-on of Sa is ZCS, because the current of La2 is zero at the time and the inductance of La2 suppresses rising of the drain current of Sa. Because Sa is now in the on-state, the output voltage is applied to Ta2 and the induced voltage appears in Ta1, which is magnetically coupled with Ta2. The induced voltage is applied to La1, thus increasing the current that flows from L1 to the output terminal through Da1, Ta1, and La1. Consequently, the current path from L1 to the output shifts from the path through D1 to that through La1. The current of Ta2 is far smaller than

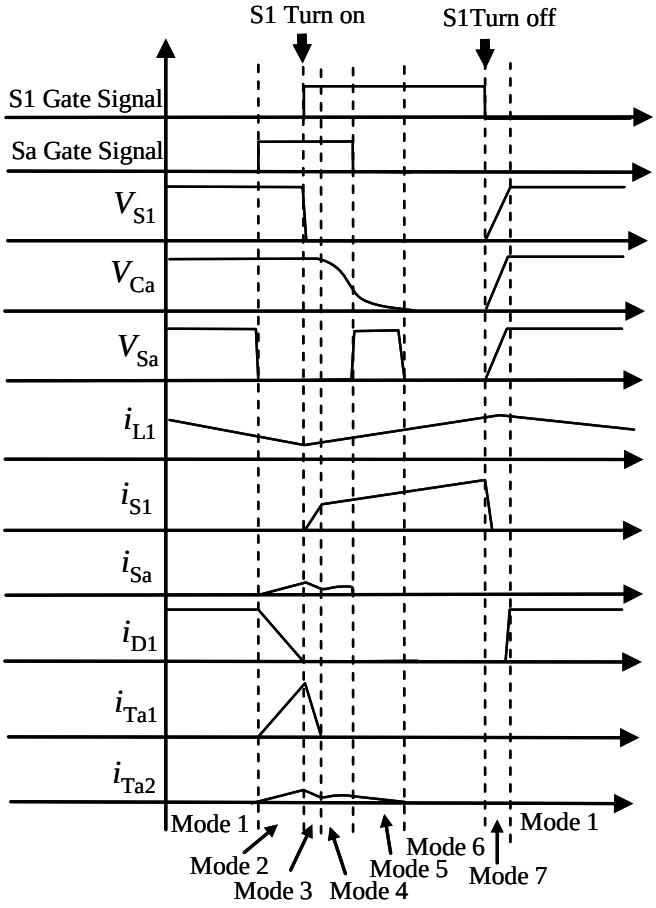

Fig. 6.5. Operating waveforms of the proposed chopper under the continuous current mode.

that of Ta1, because Ta2 has far greater number of turns than Ta1. Therefore, the current of Sa is far smaller than that of L1, which allows Sa to have smaller current rating compare to S1.

When the current of L1 has shifted the path entirely, the current of D1 falls to zero. Then, S1 is turned on, and the operation steps in Mode 3. Because most current of L1 flows through La1, the inductance of La1 suppresses rising of the drain current of S1 at the turn on. As a result, ZCS is achieved at the turn on of S1.

In Mode 3, the current of La1 decreases because negative voltage is applied to La1. After the La1 current falls to zero, instantaneous negative current flows until reverse recovery of Da1. The inductance of La1 forces to flow the negative current. In order to protect Da1 from overvoltage due to the current, the zenar diode Za and the diode Da4 are equipped in parallel with Ta1 and La1. They dissipate the destructive current by circulating it through La1, Ta1, Za, and Da4.

In Mode 4, the auxiliary switch Sa maintains the on-state, although the current of La1 has already fallen to zero. As the induced voltage in Ta1 is smaller than the inverse

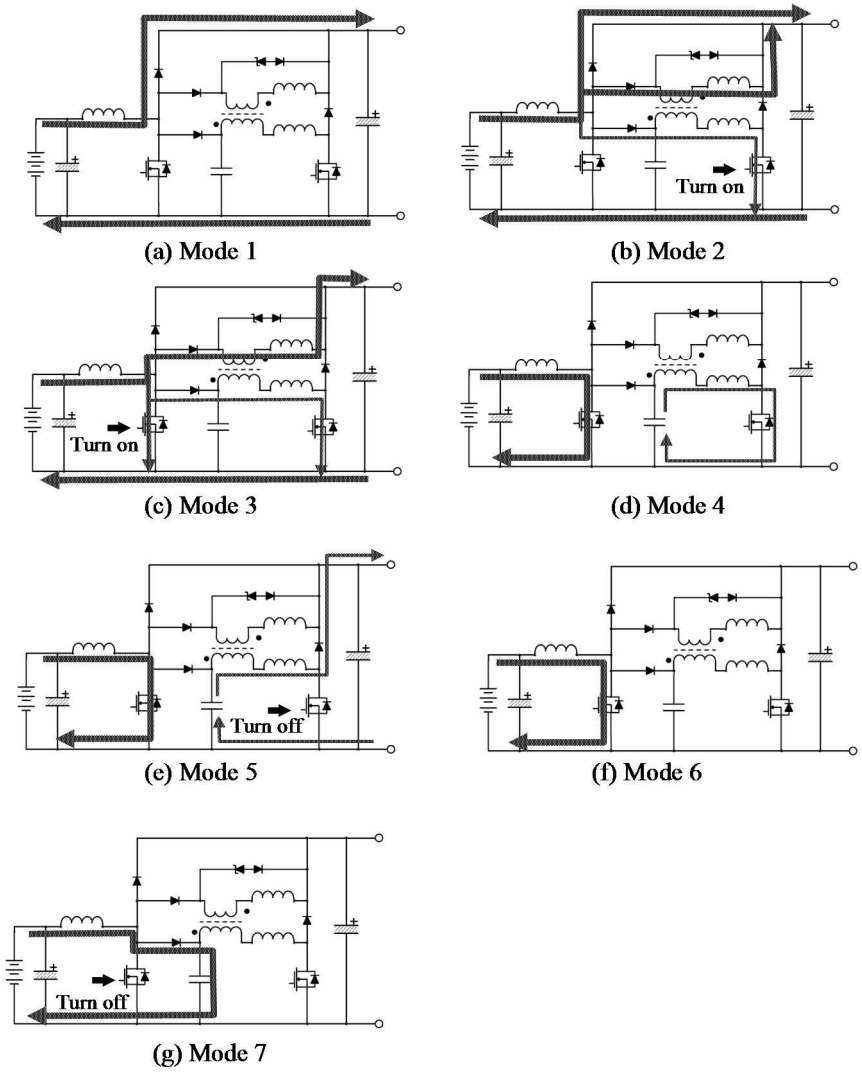

Fig. 6.6. Operating sequence of the proposed chopper under the continuous current mode.

voltage applied to Da1, no current is induced in La1. Thus, the coupled inductor Ta2 operates as an inductor, and the snubber capacitor Ca is discharged through Ta2 and La2.

After Ca is discharged below a predetermined voltage level, Sa is turned off and the operation steps in Mode 5. The current of Ta2 flows to the output terminal through La2 and Da3, to discharge Ca until its voltage falls to zero. Although the turn-off of Sa is hard-switching, the switching loss can be suppressed to an ignorable level compared to S1 because the conduction current of Sa is smaller than that of S1.

In Mode 5, the negative voltage induced in Ta1 should not induce circulating current through Ta1, which results in additional conduction loss. This is the reason why we do not employ a clamping diode [23] for Ta1 and La1, but employ the zenar diode Za and the diode Da4.

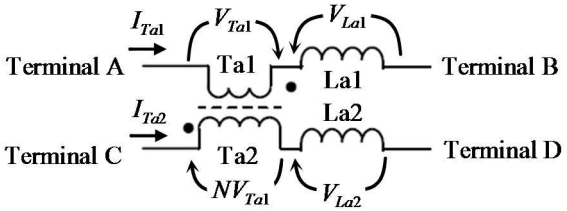

Fig. 6.7. Definition of voltage and current in the additional inductors.

The operation in Mode 5 determines the minimum zenar voltage for Za. The zenar voltage should be greater than the maximum induced voltage of Tal during Mode 5. Because the voltage applied to Ta2 does not exceed the output voltage, the induced voltage of Ta1 is less than the output voltage divided by the turn ratio of Tal to Ta2. Therefore, the zenar voltage should be greater than this voltage.

The circuit behavior in Mode 6 is the same as that in the normal chopper. The main switch S1 is in the on-state and the current of L1 gradually increase.

Then, S1 is turned off in Mode 7. Because Ca is entirely discharged at the beginning of the mode, the current of L1 flows into Ca through Da2. As a result, rising of the drain voltage of S1 is suppressed and ZVS is achieved at the turn off of S1.

After the capacitor Ca is entirely charged to the output voltage, the current of L1 then flows into the output terminal through D1. Finally, the circuit operation returns to Mode 1.

The circuit behavior in the discontinuous conduction mode is almost the same as the above. The only difference is that Mode 2 and Mode 3 is omitted, because the current of L1 has fallen to zero at the end of Mode 1 and thus the current no longer need to shift the path to that through Tal and Lal. Therefore, Sa is turned on simultaneously with the turn-on of Sl.

As discussed above, the additional circuit always conducts current from the drain of S1 to the output terminal, thus adding no current stress to S1. Besides, the voltage across S1 is confined between zero and the output voltage because of diode clamping by D1 and the body diode of S1. Hence, the proposed chopper adds the same voltage stress on S1 as the basic hard-switching chopper that consists of S1 and D1.

Consequently, the proposed chopper can operate under both the continuous conduction mode and the discontinuous conduction mode. Furthermore, the current of Sa is smaller than that of L1, which allows Sa to have smaller current rating compared to S1. And neither voltage nor current stress is added to S1 by the soft-switching operation.

The next section discusses the remaining requirements listed in the introduction, namely the soft-switching capability regardless to the input and the output voltage and that the control of Sa is implementable by basic arithmetic operations.

6. 3. Control of Auxiliary Switch Sa

In order to accomplish the soft-switching of S1, the controller of Sa is required to fulfill the following two operations. One is to shift the Ll current entirely from D1 to the

additional circuit in Mode 2. This operation ensures the ZCS turn-on. The other is to discharge Ca entirely at the end of Mode 5. And this operation ensures the ZVS turn-off.

This section discusses the control of Sa analytically to show that the above two requirements are both achievable regardless to the input and the output voltage and that they are able to be implemented arithmetically.

A. ZCS Turn-on

This subsection discusses the control of Sa for the ZCS turn-on.

Let V_{Ta1}, V_{La1}, and V_{La2} be the voltage of Ta1, La1, and La2, as shown in Fig. 6.7. In addition, we denote the current of Ta1 and Ta2 as I_{Ta1} and I_{Ta2}, and denote the inductance (self-inductance) of the inductors simply by their name. We regard the leakage inductance of the coupled inductor Ta1 (Ta2) is contained in La1 and La2. Thus, the coupling coefficient of the coupled inductor is regarded as 1. For convenience, we define the terminals A–D as shown in Fig. 6.7.

Throughout Mode 2, the voltage potential difference between the terminal A and B remains zero and that between the terminal C and D equals to the output voltage V_{OUT}. Therefore, we have the following relations in Mode 2:

$$NV_{Ta1}+V_{La2}=V_{OUT},\quad V_{La1}-V_{Ta1}=0; \tag{6.6}$$

$$V_{La1}=L_{a1}\frac{dI_{Ta1}}{dt},\quad V_{La2}=L_{a2}\frac{dI_{Ta2}}{dt},\quad V_{Ta1}=T_{a1}\left(N\frac{dI_{Ta2}}{dt}-\frac{dI_{Ta1}}{dt}\right), \tag{6.7}$$

where N is the turn ratio of Ta2 to Ta1.

Introducing the total current I_S that flows into the additional circuit, i.e. $I_S=I_{Ta1}+I_{Ta2}$, we obtain (6.8) from the above equations.

$$\frac{dI_S}{dt}=\frac{V_{OUT}}{L_{a2}}\left\{1+\left(\frac{N}{L_{a1}}-\frac{N^2}{L_{a2}}\right)\left(\frac{1}{T_{a1}}+\frac{1}{L_{a1}}+\frac{N^2}{L_{a2}}\right)^{-1}\right\}. \tag{6.8}$$

The right-hand side of (6.8) is almost constant, because the output voltage V_{OUT} is decoupled by the output capacitor. Hence, we can approximate the increase rate of I_S as constant. The duration of the Mode 2, which we denote as Δt_2, is obtained as the time for I_S to rise from zero to the current of L1 at the turn on, which we denote as I_{ON} .

$$\Delta t_2=\frac{L_{a2}}{\alpha}\frac{I_{ON}}{V_{OUT}}, \tag{6.9}$$

$$\text{where } \alpha\equiv 1+\left(\frac{N}{L_{a1}}-\frac{N^2}{L_{a2}}\right)\left(\frac{1}{T_{a1}}+\frac{1}{L_{a1}}+\frac{N^2}{L_{a2}}\right)^{-1}.$$

Equation (6.9) shows that Δt_2 can be determined for any input and output voltage and current, unless Δt_2 does not exceed the on-state period of S1. Note that α is a constant.

Therefore, Δt_2 is proportional to I_{ON}/V_{OUT} and thus can be set by multiplication and division.

B. ZVS Turn-off

Next, we step in Sa control for the ZVS turn-off.

The ZVS turn-off can be achieved at any input and output voltage and current. The reason is explained as follows. During Mode 3 and Mode 4, inverse voltage is applied to the diode Da2. As are result, the snubber capacitor Ca is electrically isolated from the main chopper made of S1 and D1. Hence, Ca can be entirely discharged at any conditions by maintaining the auxiliary switch Sa in the on-state for sufficiently long time.

Furthermore, the ZVS turn-off is also able to be controlled arithmetically. As shown in the successive discussion, the duration of Mode 3 (Δt_3) is approximately proportional to I_{ON}/V_{OUT}. If the duration of Mode 4 (Δt_4) is set, for example, at the constant time which suffice to discharge Ca entirely at all input and output conditions, then the on-state duration of Sa is calculated by summation, multiplication and division. The duration Δt_3 and Δt_4 can be determined according to the following discussion.

First, we determine the current I_A and I'_A which I_{Ta1} and I_{Ta2} reach at the end of Mode 2, respectively. The current I_A and I'_A is obtained from (6.6), (6.7) and (6.9), as follows:

$$\begin{cases} I_A = \dfrac{N}{1+N+L_{a1}/T_{a1}} I_{ON}, \\ I'_A = \dfrac{1+L_{a1}/T_{a1}}{1+N+L_{a1}/T_{a1}} I_{ON}. \end{cases} \tag{6.10}$$

We then determine Δt_3. In Mode 3, the voltage potential difference between the terminal A and B equals to $-V_{OUT}$. The difference between the terminal C and D approximately equals to V_{OUT} because Mode 3 is generally too short to discharge Ca. Thus, we obtain the following relation:

$$NV_{Ta1} + V_{La2} = V_{OUT}, \quad V_{La1} - V_{Ta1} = -V_{OUT}\ . \tag{6.11}$$

The decrease rate of I_{Ta1} is obtained from (6.7) and (6.11):

$$\frac{dI_{Ta1}}{dt} = V_{OUT}\left(NT_{a1}\frac{NT_{a1} - T_{a1} - L_{a1}}{N^2T_{a1} - NT_{a1} + L_{a2}} - T_{a1} - L_{a1} \right)^{-1}. \tag{6.12}$$

The right-hand side of (6.12) is again a constant. Hence, Δt_3 is obtained as the time for I_{Ta1} to fall from I_A to zero:

$$\Delta t_3 = \frac{N\beta}{1+N+L_{a1}/T_{a1}} \frac{I_{ON}}{V_{OUT}}, \tag{6.13}$$

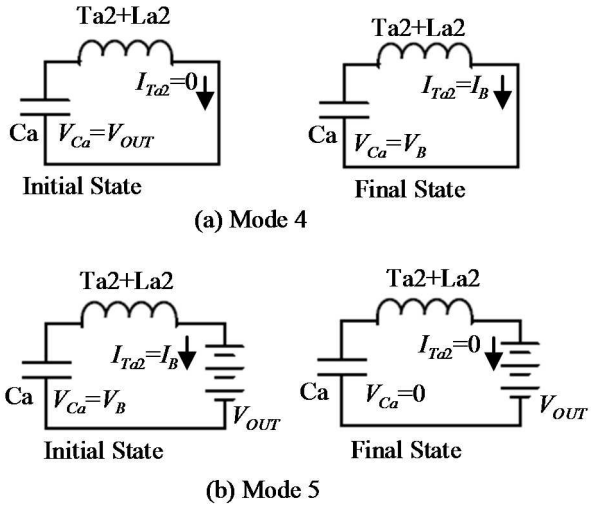

Fig. 6.8. Equivalent circuits of the additional circuit for Mode 4 and Mode 5.

where $\beta \equiv L_{a1} + T_{a1} - NT_{a1} \dfrac{NT_{a1} - T_{a1} - L_{a1}}{N^2 T_{a1} - NT_{a1} + L_{a2}}$.

Consequently, Δt_3 is shown proportional to I_{ON}/V_{OUT}.

Next, we determine the constant time for Δt_4. Here, we adopt the least time that suffices to discharge Ca entirely at the end of Mode 5 under all operating conditions. Note that the discharge time is longest, when I_{Ta2} is equals to zero and the voltage across Ca (V_{Ca}) equals to its maximum possible value, i.e. V_{OUT}, at the beginning of Mode 4. For this reason, the discontinuous conduction mode takes the longest discharge time, and Δt_4 is determined by discussing the operation under the mode.

In Mode 4 and Mode 5, the coupled inductor Ta2 works as an inductor. Accordingly, the additional circuits in the operation mode are expressed by the equivalent circuits illustrated in Fig. 6.8. The equivalent circuits show that V_{Ca} can be obtained by considering the LC oscillation made of Ta2, La2 and Ca. The voltage V_{Ca} oscillates around zero in Mode 4, and around V_{OUT} in Mode 5. For convenience, we denote the value of I_{Ta2} and V_{Ca} at the end of Mode 4 as I_B and V_B respectively. According to the conservation of oscillatory energy, we have the following simultaneous equations:

$$\begin{cases} \dfrac{1}{2} C_a {V_{OUT}}^2 = \dfrac{1}{2}(T_{a2} + L_{a2}) {I_B}^2 + \dfrac{1}{2} C_a {V_B}^2, \\ \dfrac{1}{2}(T_{a2} + L_{a2}) {I_B}^2 + \dfrac{1}{2} C_a (V_{OUT} - V_B)^2 = \dfrac{1}{2} C_a {V_{OUT}}^2. \end{cases} \tag{6.14}$$

Solving the above equations, we obtain $V_B = V_{OUT}/2$. On the other hand, V_{Ca} is expressed by the following equation, if we introduce the time t whose origin is set at the beginning of Mode 4:

Table. 6.1. Specifications of the prototype.

Rating	VOUT=400V, POUT*=5kW
Frequency	60kHz
S1	SPW47N60CFD, 600V, 47A
D1	HFA50PA60, 600V, 50A
Sa	STB4NK60Z, 600V, 4A
L1**	270μH (Nippon Chemi-Con: AW30201WLH)
La1**	1.21μH
La2**	45.6μH
Ta1**	1.24μH (5 Turns)
Ta2**	100μH (45 Turns)
Ca	4.4nF
Za	1N5374B × 2, 75V, 5W
Da1, Da2	HFA30TA60C, 600V, 15A
Da3, Da4	HFA16TA60C, 600V, 8A

* Maximum Output Power

** Inductance is measured by an impedance analyzer (Agilent 4294A)

$$V_{Ca} = V_{OUT} \cdot \cos\left(\frac{t}{\sqrt{(T_{a2} + L_{a2})C_a}} \right). \tag{6.15}$$

Finally, Δt_4 is obtained as the time when V_{Ca} falls to V_B:

$$\Delta t_4 = \sqrt{(T_{a2} + L_{a2})C_a} \cos^{-1}\frac{1}{2} = \frac{\pi\sqrt{(T_{a2} + L_{a2})C_a}}{3}. \tag{6.16}$$

Equations (6.13) and (6.16) show that the ZVS turn-off can be implemented by determining Sa control timing by arithmetic operations on I_{ON} and V_{OUT}.

6. 4. Experiment

Circuit behavior of the proposed boost chopper and resulting improvement of conversion efficiency are evaluated experimentally.

Circuit behavior is examined by observation of operating waveforms and switching waveform of S1. Improvement of efficiency is examined by comparing the efficiency between the proposed chopper and the basic hard-switching chopper, i.e. the chopper that only consists of S1 and D1. In addition, we estimated the breakdown of the total loss to confirm contribution of the soft-switching of S1 to the improvement.

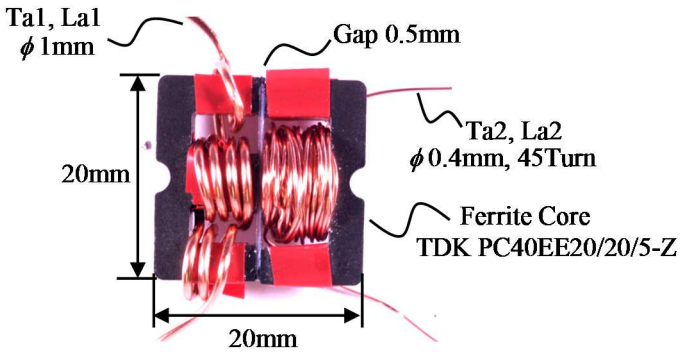

Fig. 6.9. Photograph of the integrated magnetic device, which implements Ta1 (Ta2), La1, and La2 of the prototype.

Table. 6.2. Measured Inductance of the Winding A and B.

Symbol	Winding A	Winding B	Inductance
L_{M1}	Measured	Opened	2.45μH
L_{M2}	Measured	Closed	1.60μH
L_{M3}	Opened	Measured	146μH
L_{M4}	Closed	Measured	95.4μH

A 5kW prototype chopper is employed in the experiment. The specifications are shown in Table 1. The main switch S1 and the main diode D1 is cooled on a water-cooling heat sink. The other circuit elements including the additional circuit are cooled with blower. The integrated magnetic device and the main inductor L1 is sufficiently cooled, because temperature indicator labels (Nichiyu Giken Kogyo Co., Ltd. Thermo Label A-90) attached on them indicated that their temperature is always kept below 50°C.

According to (6.10), the large ratio for N is beneficial in suppressing I_{Ta2} and the current of the auxiliary switch Sa. On the other hand, (6.9) indicates that excessively large N results in long period for Mode 2 and may constrain the minimum duration of the on-state of S1. In this prototype, we chose N=9.

The inductors Ta1 (Ta2), La1 and La2 are implemented on a pair of ferrite E cores in the same way as Fig. 6.2. As discussed in Subsection 6.2.B, Ta1 has the number of turns expressed as $N_2+N_3/2-N_1/2$, using the number of turns defined in Fig. 6.2. Thus, we set $N_2+N_3/2-N_1/2=5$ and $N_4=45$ to obtain N=9. While keeping the ratio, we can further adjust the inductance of La1 by increasing or decreasing N_1 and N_3 by the same turn number. As a result, we obtained N_1=1, N_2=4, and N_3=3.

The integrated magnetic device employed in the prototype is presented in Fig. 6.9. The circuit parameters of the equivalent circuit, shown in Table 6.1, are estimated from the measurement of the magnetic device according to the method presented in the next subsection.

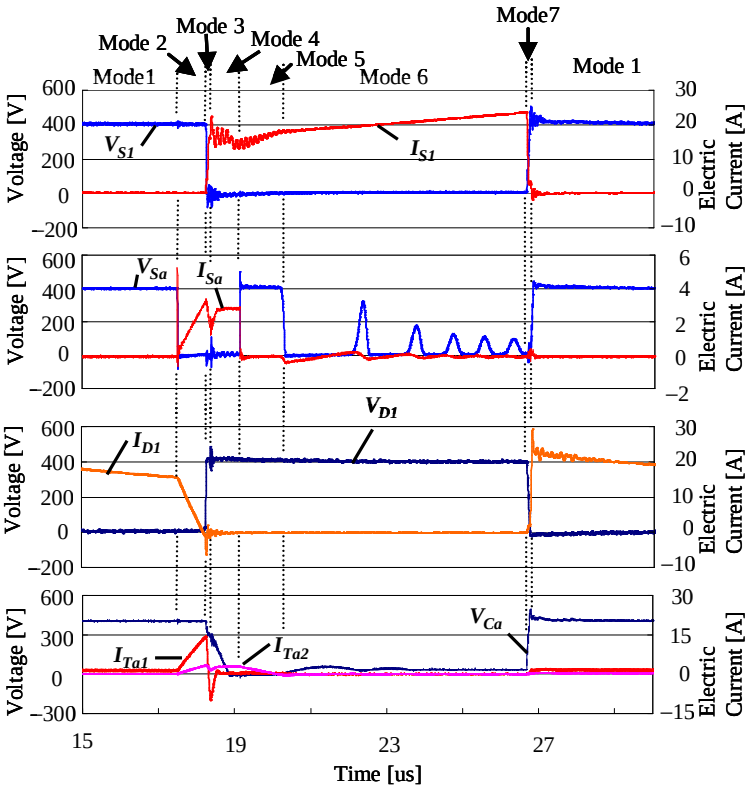

Fig. 6.10. Operating waveforms of the proposed boost chopper under the continuous conduction mode (Input:200V; Output:400V, 4kW; Duty=50%).

A. Inductance Estimation of the Integrated Magnetic Component

The inductance of the inductors in the equivalent circuit is estimated based on inductance measurement of the winding A and B, when the other winding is opened and closed, respectively. We present the result in Table 6.2. On the other hand, the measured inductance can be expressed analytically using parameters of the equivalent circuit. Therefore, equating the expression to the result of measurement, we can estimate the parameters.

Here, we discuss the estimation utilizing the symbols used in Section 6.3.

The expression for L_{M1} and L_{M3} are easily obtained, because they are the sum of the self inductance that constitutes the measured winding. Thus, we have:

$$L_{M1} = T_{a1} + L_{a1}, \tag{6.17}$$

$$L_{M3} = T_{a2} + L_{a2}. \tag{6.18}$$

As for L_{M2}, we calculate the relation between the voltage V and the current I_{Ta1} of the winding A. The voltage relation can be expressed as follows:

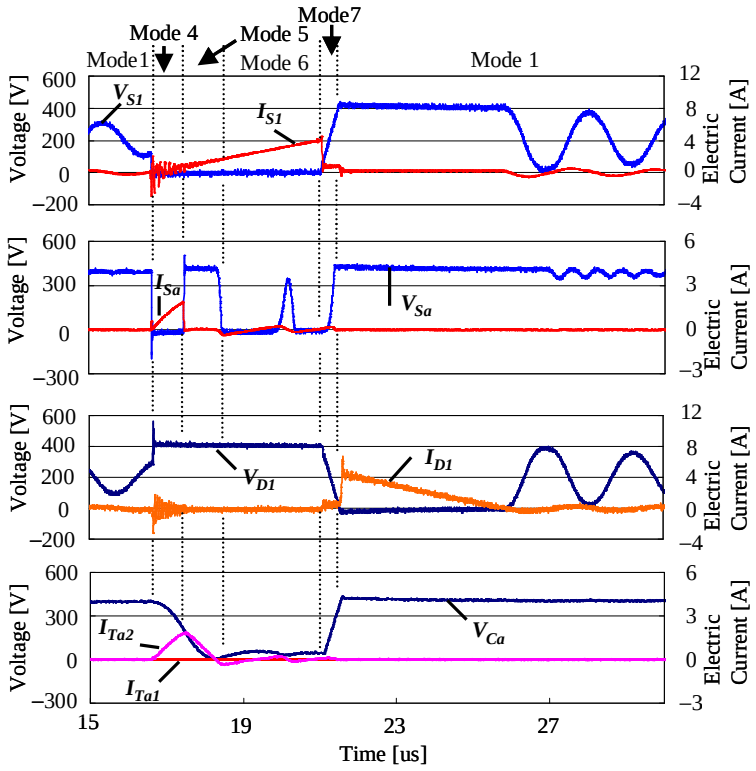

Fig. 6.11. Operating waveforms of the proposed boost chopper under the discontinuous conduction mode (Input:200V; Output:400V, 200W; Duty=26%).

$$NV_{Ta1}+V_{La2}=0,\quad V_{La1}-V_{Ta1}=V\,. \tag{6.19}$$

Solving (6.19) and (6.7), we obtain the following relation:

$$\left(L_{a1}+\frac{T_{a1}L_{a2}}{T_{a2}+L_{a2}}\right)\frac{dI_{Ta1}}{dt}=V\,. \tag{6.20}$$

Thus, we obtain

$$L_{M2}=L_{a1}+\frac{T_{a1}L_{a2}}{T_{a2}+L_{a2}}\,. \tag{6.21}$$

Similarly, we calculate the voltage and current relation for L_{M4}. Now, the voltage is set as follows:

$$NV_{Ta1}+V_{La2}=V,\quad V_{La1}-V_{Ta1}=0\,. \tag{6.22}$$

Solving (6.22) and (6.7) yields the following relation:

$$\left(L_{a2} + \frac{T_{a2} L_{a1}}{T_{a1} + L_{a1}} \right) \frac{dI_{Ta2}}{dt} = V$$

$$\therefore L_{M4} = L_{a2} + \frac{T_{a2} L_{a1}}{T_{a1} + L_{a1}} . \tag{6.23}$$

Comparing Table 6.2 with (6.17), (6.18), (6.21), and (6.23) resulted in the inductance La1, La2, Ta1, and Ta2 shown in Table 6.1.

B. Operating Waveforms

Current and voltage waveforms are observed by operating the experimental chopper for one operation cycle. Before the one cycle operation, we charged the inductor L1 with predetermined current in advance, so that the waveforms reflect the operation under a specific condition. We adopt 200V as the input voltage, 400V as the output voltage. The output power is set at 4kW and 200W so that the prototype is operated under the continuous and discontinuous conduction modes. We calculated the duration Δt_2–Δt_4 according to the previous section for gating control of the auxiliary switch Sa.

Figure 6.10 illustrates the voltage and current waveforms observed in the operation under the continuous conduction mode. The waveforms are found almost consistent with that expected in Subsection 6.2.C.

In addition, the requirements for the ZCS turn-on and the ZVS turn-off are found to be achieved as expected from the theoretical discussions. As for the ZCS turn-on, I_{Ta1} rises linearly during Mode 2 and S1 is turned on at the time when the current of D1 (I_{D1}) falls down to zero. And as for the ZVS turn-off, Ca is entirely discharged before the end of Mode 5.

The waveforms in Mode 4 and Mode 5 indicate the snubber energy regeneration. The current I_{Ta2} increases during the discharge of Ca. This fact indicates that electric energy charged in Ca is transferred to magnetic energy in Ta2 and La2. After Sa is turned off at the beginning of Mode 5, I_{Ta2} flows into the output terminal and gradually decreases to zero. Finally, energy of Ca, along with magnetic energy of Ta2 and La2, is regenerated as the output power.

On the other hand, two discrepancies are found in Mode 6 between the theory and the experiment. One is that V_{Ca} rises slightly after once it dropped to zero. And the other is that the voltage across Sa (V_{Sa}) oscillates several times during the mode. Both of them seem to be caused by the parasitic capacitance of Da3 and Sa, which is ignored in the theoretical discussions.

After I_{Ta2} falls to zero at the end of Mode 5, the voltage V_{Sa} drops. Then, electric charge stored in the parasitic capacitance of Da3 and Sa are released according to the voltage drop. The released charge flows into Ca, thus raising V_{Ca} again. In general, the capacitance of Ca is designed much larger than the parasitic capacitance of the semiconductor device, because small capacitance compared to the parasitic capacitances does not contribute significantly to ZVS at the turn-off. Therefore, the effect of raising V_{Ca} again tends to be ignorable compared to the output voltage and hardly affects soft-switching capability.

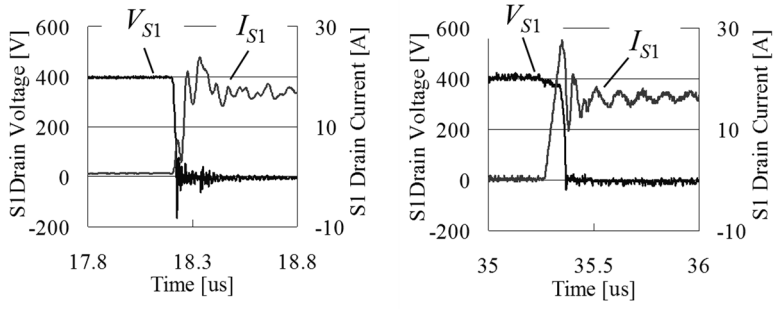

(a) Proposed chopper

(b) Conventional chopper
(the hard switching chopper)

Fig. 6.12. Turn-on waveforms of the main switch S1 operated under the continuous conduction mode. (Input: 200V; Output: 400V, 4kW; Duty=50%)

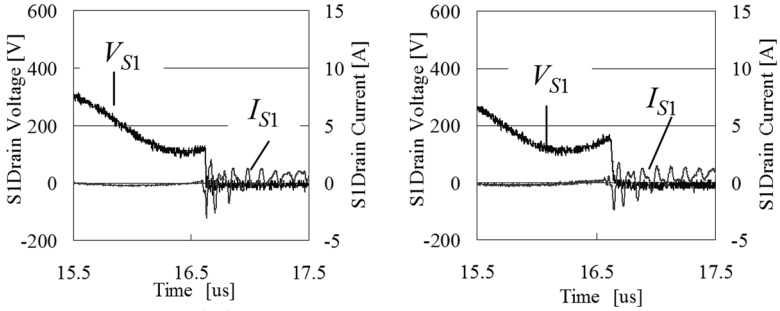

(a) Proposed chopper

(b) Conventional chopper
(the hard switching chopper)

Fig. 6.13. Turn-on waveforms of the main switch S1 operated under the continuous conduction mode. (Input: 200V; Output: 400V, 4kW; Duty=50%)

The recharge process of Ca also explains the oscillation found in V_{Sa}, because Ca is recharged through Ta2 and La2. There are a parasitic LC oscillator composed of Ta2, La2, and the parasitic capacitors. The recharge process excites the parasitic oscillator, resulting in the oscillation in V_{Sa}. This interpretation is supported by the fact that the frequency of the oscillation is in the order of the eigenfrequency of the oscillator.

The results of the discontinuous conduction mode, presented in Fig. 6.11, are also found consistent with that described in Subsection 6.2.C. In this operating mode, I_{Ta1} remains zero because the inductor current no longer needs to shift the path to Ta1 and La1. In addition, the waveforms of the current I_{Ta2} and the voltage V_{Ca} successfully showed the oscillation between Ta2, La2, and Ca in Mode 4 and 5, indicating energy regeneration of the snubber Ca. On the other hand, the above mentioned two discrepancies are also found in Mode 6, which are also reasonably explained by the parasitic capacitance in the additional circuit.

To summarize, the circuit behavior as a whole is consistent with that expected from theoretical discussions, regardless to the continuous or discontinuous conduction mode.

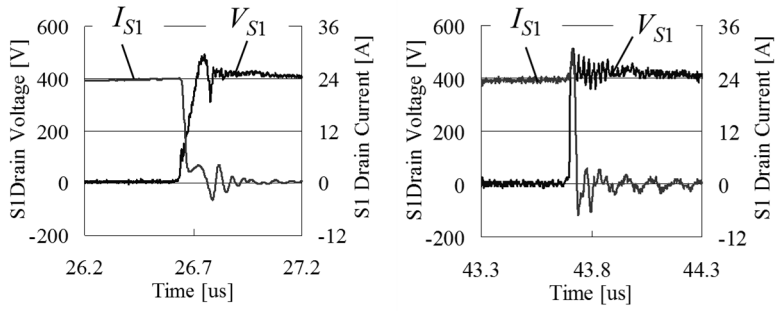

Fig. 6.14. Turn-off waveforms of the main switch S1 operated under the continuous conduction mode (Input: 200V; Output: 400V, 4kW; Duty=50%)

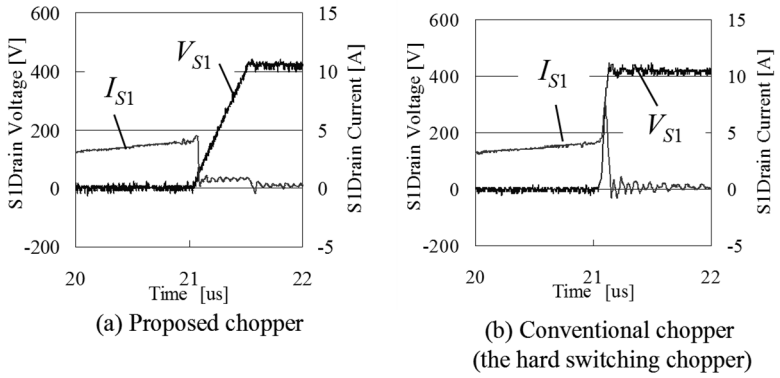

Fig. 6.15. Turn-off waveforms of the main switch S1 operated under the discontinuous conduction mode (Input: 200V; Output: 400V, 200W; Duty=26%)

Although parasitic oscillation occurs in Mode 6 due to residual charge in the parasitic capacitance of Da and Sa, the charge is generally insufficient to affect the voltage across Ca, thus scarcely hinders the soft-switching.

C. Switching Waveforms

Figures 6.12–6.15 present the switching waveforms of the proposed chopper and the basic hard-switching chopper, observed during the one cycle operation. Figure 6.12 and 6.13 show the voltage across S1 (V_{S1}) and the current of S1 (I_{S1}) of the turn on in the continuous and discontinuous conduction modes, respectively. And Fig. 6.14 and 6.15 show those at the turn off.

Comparing the waveforms between the proposed and the hard-switching chopper, we confirmed the soft-switching of the proposed chopper. As a result, I_{S1} is found to be

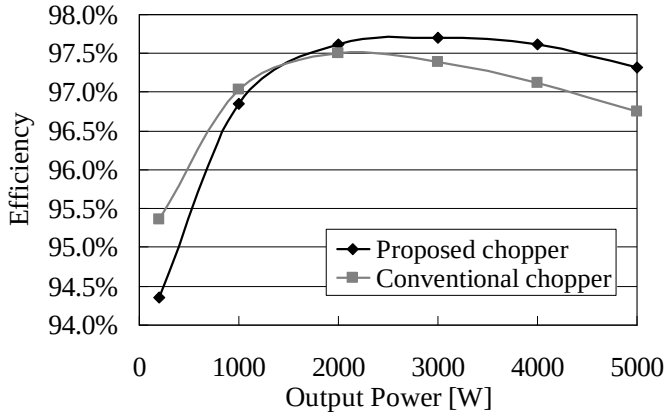

Fig. 6.16. Measured power efficiency for the proposed chopper in comparison with the hard-switching chopper. (Input: 200V, Output: 400V)

suppressed at the turn on of the proposed chopper even in the continuous conduction mode, which indicates the ZCS turn-on. Additionally, V_{S1} is also found to be suppressed at the turn off in the both conduction modes, which indicates the ZVS turn-off. Consequently, the ZCS turn-on and the turn-off ZVS is observed in the switching waveforms.

D. Conversion Efficiency

Improvement of conversion efficiency is evaluated by comparing efficiency between the proposed chopper and the basic hard-switching chopper. Efficiency is measured during operating the experimental choppers continuously. Gate resistors of S1 are selected in both choppers so that they exhibit the similar amount of the current surge in I_{S1} at the turn on and the voltage surge in V_{S1} at the turn off. We adopted 200V as the input voltage and 400V as the output voltage, the same as in Subsection 6.4.B. Six measurement points are set between 200W-5kW in the output power. We employed CROMA 63204 (6 parallel-connected) operated under CR mode as the power load.

Figure 6.16 illustrates the result. The proposed chopper showed improvement of efficiency when the output power exceeds 2kW. The maximum improvement is found to be 0.6%, when the output power is set at 5kW.

On the other hand, the proposed chopper did not show improvement when the output power is lower than 2kW. The possible reason is that efficiency of snubber energy regeneration is lower than efficiency of the main chopper, i.e. S1 and D1. The snubber energy stored in Ca is constant regardless to the output power. Therefore the efficiency of snubber regeneration affects more profoundly to the total efficiency as the output power becomes smaller. Meanwhile the switching loss becomes smaller according to the output power. Hence the reduction of switching loss may not cover worse efficiency of the regeneration process, especially when the output power is low.

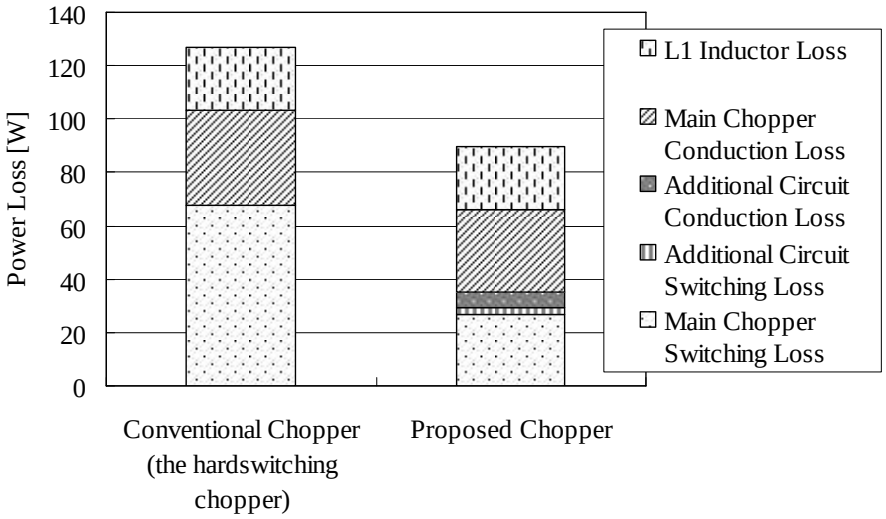

Fig. 6.17. Breakdown of total loss (Input: 200V; Output: 400V, 4kW; Duty=50%)

When the output power is high, the snubber energy is comparatively ignorable. Therefore the reduction of switching loss consistently contributed to the improvement of total conversion efficiency.

E. Breakdown of Total Loss

Figure 6.17 illustrates estimated breakdown of total loss, when the output power is set at 4kW. The estimation is based on the voltage and current waveforms measured in Subsection 6.4.B and 6.4.C. The estimation predicted the total loss observed experimentally within an error of 10%.

The conduction loss of diodes is estimated by approximating the voltage drop by their typical values. And that of MOSFETs are estimated by supposing typical resistance at their on-state. Both the typical voltage drop and resistance are determined by considering the dependency on the junction temperature. The temperature is estimated on the breakdown of the loss so that the loss of each semiconductor device consistently results in the junction temperature. Switching loss is calculated from the switching waveforms presented in Fig. 6.12 and 6.14. Loss of magnetic devices is estimated by summing loss created by AC and DC component of the current in each winding. The loss by AC and DC component is estimated by supposing constant AC and DC resistance, respectively. We adopted the AC resistance at switching frequency as the constant AC resistance.

The estimation result shows that the proposed chopper significantly reduced the switching loss in the main chopper and it is the main contributor of the reduction of the total loss. The reduction is greater than the loss of the additional circuit. Thus, it is consistent that the soft-switching effectively contributed to the improvement of the efficiency.

6. 5. Conclusions

Boost choppers are often utilized in EVs, HVs, and FCVs. These choppers tend to be strongly required to improve efficiency because of limited cooling capability of the vehicles. However, the soft-switching techniques are generally difficult to be reasonably applied, because the load power and the output voltage varies widely according to traveling conditions, resulting in limitation of soft-switching capability and large cost-up due to implementing additional circuits and soft-switching control.

This chapter proposed a novel soft-switching technique to overcome the difficulty in the unidirectional boost choppers of FCVs. The technique seems to be advantageous in the following four features:

1. Soft-switching is achievable regardless to the output power and voltage.
2. Soft-switching control can be implemented by arithmetic operations on the output voltage and the inductor current.
3. The additional circuit contains only one switch, which needs smaller current rating than the main switch.
4. Neither voltage nor current stress is added to the main switch by the soft-switching operation.

Experiments using the 5kW prototype were carried out to confirm circuit behavior. The observed behavior was consistent with that expected by theoretical discussion. The ZCS turn-on and the ZVS turn-off are also successfully observed in the switching waveforms.

Additionally, improvement of efficiency is evaluated on the prototype. The proposed chopper showed improvement, when the output power is greater than 2 kW. Maximum improvement is 0.6% at 5 kW output. According to the breakdown estimation of the total loss, the improvement was mainly contributed by reducing switching loss of the main switch S1. This suggests that the proposed chopper successfully improved efficiency by soft-switching.

This chapter focused on the circuit topology and the operational principles. However, a practical design method of the additional circuit seems also to be needed in order to apply the proposed circuit to practical applications. In future works, the author will investigate the inductance design method of the additional circuit, along with an optimizing design method of the integrated magnetic device with minimum copper and core volume.

REFERENCES

[1] A. Emadi, S. S. Wiliamson, and A. Khaligh, "Power electronics intensive solutions for advanced electric, hybrid electric, and fuel cell vehicular power system," *IEEE Trans. Power Electron.*, vol. 21, no. 3, pp.567-577, May 2006.

[2] M. R. Nikzad and A. Radan, "effects of fuel cell and dc-link voltage on boost converter efficiency in fuel cell-battery hybrid vehicles," in *Proc. IEEE Intl. Power Electron. Motion Control Conf. (IPEMC)*, Wuhan, China, 2009, pp.2313-2317.

[3] E. S. da Saliva, L. R. Barbosa, J. B. Vieira, L. C. de Freitas, "An improved boost pwm soft-single-switched converter with low voltage and current stresses," *IEEE Trans. Ind. Electron.*, vol. 48, no. 6, pp.1174-1179, Dec. 2001.

[4] Y. Tsuruta, M. Pavlovsky, and A. Kawamura, "Very high efficiency SAZZ chopper using high speed IGBT," in *Proc. IEEE Intl. Power Electron. Motion Control Conf. (IPEMC)*, Wuhan, China, 2009, pp.573-579.

[5] D. D.-C. Lu, D. K.-W. Cheng, and Y.-S. Lee, "A single-switch continuous-conduction-mode boost converter with reduced reverse-recovery and switching losses," *IEEE Trans. Ind. Electron.*, vol. 50, no. 4, pp.767-776, Aug. 2003.

[6] C.-M. Wang: "A new family of zero-current-switching (ZCS) PWM converters," *IEEE Trans. Ind. Electron.*, vol. 52, no. 4, pp.1117-1125, Aug. 2005.

[7] G. Calderon-Lopez and A. J. Forsyth, "High power dual-interleaved ZVS boost converter with interphase transformer for electric vehicles," in *Proc. IEEE Appl. Power Electron. Conf. Expo.*, Washington, USA, 2009, pp.1078-1083.

[8] M. R. Amini and H. Farzanehfard, "Novel family of PWM soft-single-switched DC-DC converters with coupled inductors," *IEEE Trans. Ind. Electron.*, vol. 56, no. 6, pp.2108-2114, June 2009.

[9] J.-J. Yun, H.-J. Choe, Y.-H. Hwang, Y.-K. Park, and B. Kang, "Improvement of ower-conversion efficiency of a DC-DC boost converter using a passive snubber circuit," *IEEE Trans. Ind. Electron.*, vol. 59, no. 4, pp.1808-1814, April 2012.

[10] C.-J. Tseng and C.-L. Chen, "Novel ZVT-PWM converters with active snubbers," *IEEE Trans. Power Electron.*, vol. 13, no. 5, pp.861-869, Sep. 1998.

[11] G. Hua, C.-S. Leu, Y. Jiang, and F. C. Y. Lee, "Novel zero-voltage-transition PWM converters," *IEEE Trans. Power Electron.*, vol. 9, no. 2, pp.213-219, Mar. 1994.

[12] T.-F. Wu, Y.-S. Lai, J.-C. Hung, and Y.-M. Chen, "Boost converter with coupled inductors and buck-boost type of active clamp," *IEEE Trans. Ind. Electron.*, vol. 55, no. 1, pp.154-162, Jan. 2008.

[13] M. Ahmadi, E. Galvan, and E. Adib, "New fully soft switched bi-directional converter for hybrid electric vehicles: analysis and control," in *Proc. 36th Annu. Conf. IEEE Ind. Electron. Soc. (IECON)*, Phoenix, Arizona, USA, 2010, pp.2340-2345.

[14] P. S. G. Giacomini, J. S. Scholtz, and M. Mezaroba, “Step-up / step-down DC-DC ZVS PWM converter with active clamping,” *IEEE Trans. Ind. Electron.*, vol. 55, no. 10, pp.3635-3643. Oct. 2008.

[15] S. Park and S. Choi, “Soft-switched CCM boost converter with high voltage gain for high power applications,” in *Proc. IEEE Energy Conversion Congr. Expo. (ECCE)*, San Jose, California, USA, 2009, pp.1999-2006.

[16] W. Li, W. Li, Y. Deng, and X. He, “Single-stage single-phase high-step-up ZVT boost converter for fuel-cell microgrid system,” *IEEE Trans. Ind. Electron.*, vol. 25, no. 12, pp.3057-3065, Dec. 2010.

[17] J. Bauman and M. Kazerani, “A novel capacitor-switched regenerative snubber for DC/DC boost converters,” *IEEE Trans. Ind. Electron.*, vol. 58, no. 2, pp.514-523, Feb. 2011.

[18] J. P. Gegner and C. Q. Lee, “Zero-voltage-transition converters using an inductor feedback technique,” in *Proc. IEEE Appl. Power Electron. Conf. Expo.(APEC)*, Orlando, Florida, USA, 1994, vol. 2, pp.862-868.

[19] R. L. Lin, Y. Zhao, and F. C. Lee, “Improved soft-switching ZVT converters with active snubber,” in *Proc. IEEE Appl. Power Electron. Conf. Expo.(APEC)*, Anaheim, California, USA, 1998, vol. 2, pp.1063-1069.

[20] X. Wu, X. Jin, L. Huang, and G. Feng, “A lossless snubber for DC/DC converters and its application in PFC,” in *Proc. IEEE Intl. Power Electron. Motion Control Conf. (IPEMC)*, Beijing, China, 2000, vol. 3, pp.1144-1149.

[21] M. Nakamura, T. Myoui, M. Ishitobi, and M. Nakaoka, “A soft-switching PWM boost chopper controlled DC-DC converter with a single passive auxiliary resonant snubber and its performance evaluation”, *IEEJ Trans. Ind. Appl.*, vol. 122-D, no. 10, pp.1006-1016, 2002. (in Japanese)

[22] C. Lanczos, “Kinosthenic or ignorable variables and their elimination,” in *The Variational Principles of Mechanics*, 4th ed., New York: Dover, 1970, pp.125-130.

[23] T. Mishima and M. Nakaoka, “A practical ZCS-PWM boost DC-DC converter with clamping diode-assisted active edge-resonant cell and its extended topologies”, IEEE Trans. Ind. Electron., vol. 60, no. 6, pp.2225-2236, June 2013.

Chapter 7

LAGRANGIAN-BASED DERIVATION OF A NOVEL SLIDING-MODE CONTROL FOR SYNCHRONOUS BUCK CONVERTERS

7. 1. Introduction

Synchronous buck converters have been utilized in a wide application area, such as communication, robotics, and consumer electronics. These converters are generally required to stabilize the output voltage against load change. A well-known specification for this stability is transient response to a step load change, which is a faster change beyond the possible response speed of the converter. However, in many practical applications, the load is designed to change within the response speed. In these applications, the dynamic load regulation against comparatively slow load changes, or the output impedance [1], may also be a useful specification.

With respect to the output voltage stability, the PWM-based sliding-mode control have been attracting great interest because it can offer fast transient response in wide operating range [2]. However, as shown later, the dynamic load regulation can be further improved by a novel sliding-mode control method proposed in this chapter.

We utilized Lagrangian modeling [3] to derive this control method because it can convert complicated energy conserving systems into simple dynamically equivalent systems [3][4]. In fact, this chapter converts the synchronous buck converter into two independent systems, which enables decoupling between the output voltage and the load current. Along with theoretical derivation of the proposed control, this chapter also presents simulation results that support improvement of the dynamic load regulation.

7. 2. Proposed Control Method

A. Lagrangian Modeling

This section derives Lagrangian model of a synchronous buck converter system shown in Fig. 7.1(a). To model this system as an energy conserving system, we regard the load as an imaginary synchronous boost converter that emulates the load by extracting the load current, as shown in Fig. 7.1(b). (We neglect the current ripple of this converter.) We regard that switch S4 operates at duty cycle D_2, which is unknown to the controller of the buck converter. For convenience, we assume that inductors L1 and L2 are the same. Let N and R be the number of their winding turns and the reluctance of their cores. We regard the switching-state indicators presented in [3] or Subsection 1.3 of this thesis as duty

[†] Reprinted, with permission, from K. Umetani, M. Yamamoto, and E. Hiraki, Lagrangian-based derivation of a novel sliding-mode control for synchronous buck converters, IEEJ Journal of Industry Applications, Nov. 2015.

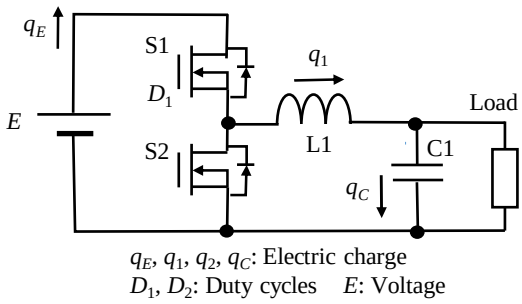

(a)

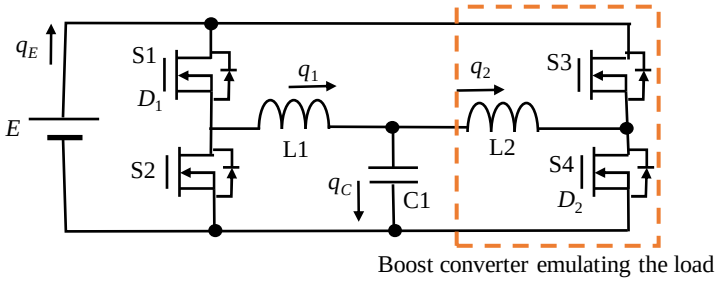

(b)

Fig. 7.1. Buck converter system analyzed in this chapter. (a) Synchronous buck converter with a load. (b) Analyzed equivalent system.

cycles to discuss a state-averaged model. Then, Lagrangian model [3] Λ for this system is

$$\Lambda = N\dot{q}_1\phi_1 + N\dot{q}_2\phi_2 - \frac{1}{2}R\phi_1^2 - \frac{1}{2}R\phi_2^2 - \frac{1}{2C}(Q+q_C)^2 + Eq_E$$
$$+ \lambda_1\{q_E - D_1q_1 + (1-D_2)q_2\} + \lambda_2(q_1 - q_2 - q_C)\cdot \tag{7.1}$$

where ϕ_1 and ϕ_2 are the fluxes in L1 and L2, q_1 and q_2 are the charge flowing through L1 and L2, Q is the initial charge of C1, q_C is the charge flowing into C1, E is the voltage of the power source, D_1 is the duty cycle of S1, λ_1 and λ_2 are the Lagrangian multipliers. A dot over a variable represents its time derivative.

Now, we apply a coordinate transformation [5] to (7.1) to obtain Lagrangian of a dynamically equivalent system. First, we eliminate Lagrangian multiplier terms by substituting $q_E=D_1q_1-(1-D_2)q_2$ and $q_1=q_C+q_2$ into (7.1). Second, we introduce new variables ϕ_A, ϕ_C and q_A defined as $\phi_A=(\phi_1+\phi_2)/2$, $\phi_C=\phi_1-\phi_2$ and $q_A=(q_1+q_2)/2$. Eliminating ϕ_1, ϕ_2, q_1 and q_2 from (7.1) yields

$$\Lambda = 2N\dot{q}_A\phi_A - R\phi_A^2 + ED_Aq_A + \frac{1}{2}N\dot{q}_C\phi_C - \frac{1}{4}R\phi_C^2 - \frac{1}{2C}(Q+q_C)^2 + ED_Cq_C\,. \tag{7.2}$$

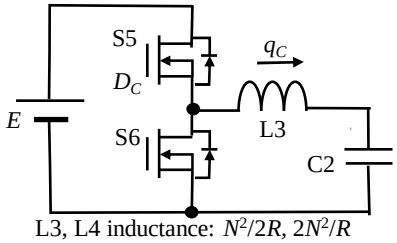

(a)

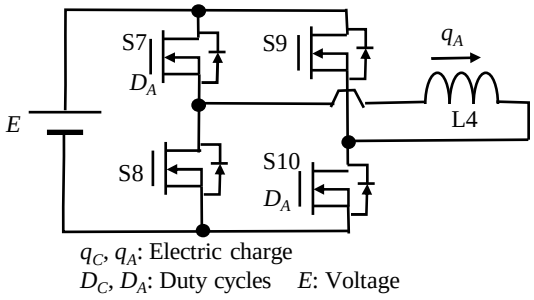

(b)

Fig. 7.2. Equivalent system of Fig. 1(b). (a) Converter of the charge q_C. (b) Converter of the charge q_A.

where D_A and D_C are imaginary duty cycles defined as $D_A=D_1+D_2-1$ and $D_C=(D_1-D_2+1)/2$. Note that D_A takes from −1 to 1; and D_C takes from 0 to 1. Hence, (7.2) can be translated into an equivalent system of two independent converters shown in Fig. 7.2, according to the method presented in [3] or Chapter 1.

Figure 7.2(a) is a closed system of q_C; therefore, it is unaffected by the load current incorporated in q_A. Because the output voltage V_{out} of Fig. 7.1(a) is equal to the C2 voltage V_{C2} in Fig. 7.2(a), controlling V_{C2} in Fig. 7.2(a) eliminates the effect of the load current on V_{out}.

In Fig. 7.2(a), q_C is controlled through D_C. In the actual circuit, however, we can only adjust D_1 to obtain appropriate D_C. Because of the relation $D_1=2D_C+D_2-1$, D_2 need to be inferred in order to calculate necessary D_1 from the required value for D_C.

According to the voltage relation at the inductor L2, we have

$$L_2 \frac{di_{\text{out}}}{dt} = V_{\text{out}} - (1 - D_2)E \tag{7.3}$$

where i_{out} is the load current, and t is the time. Substituting (7.3) into $D_1=2D_C+D_2-1$ and noting that L1 and L2 have the same inductance, we have

$$D_1 = 2D_C - \frac{V_{\text{out}}}{E} + \frac{L_1}{E}\frac{dI_{\text{out}}}{dt}. \tag{7.4}$$

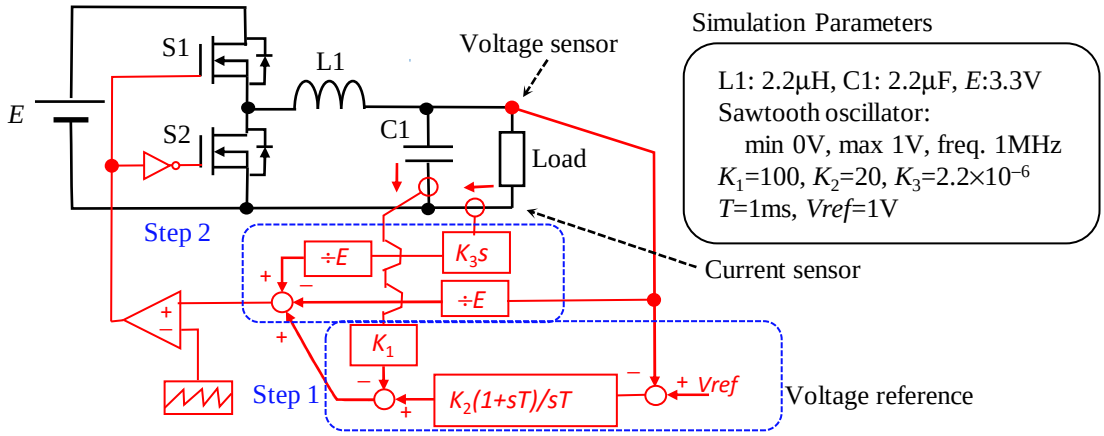

Fig. 7.3. Simulation model of the proposed control.

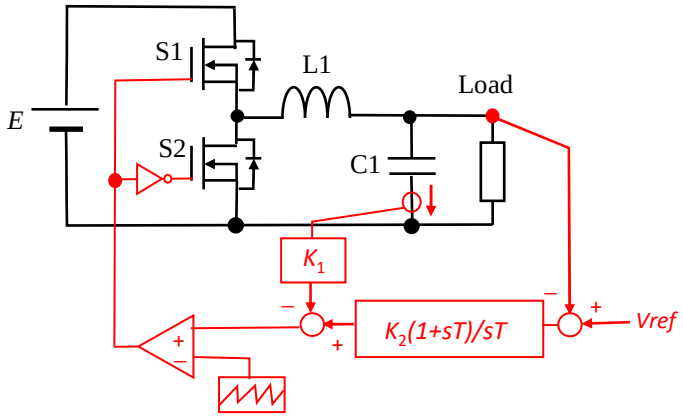

Fig. 7.4. Simulation model of the PWM-based sliding-mode control. (Parameter values are the same as Fig. 7.3)

B. Proposed Control

Based on the above discussion, we can formulate the proposed control of Fig. 7.1(a). The control consists of the following two steps: 1. Determine D_C according to the PWM-based sliding mode control of the imaginary converter, i.e. Fig. 7.2(a), and 2. Determine D_1 from D_C according to (7.4).

Figure 7.3 illustrates an example of the control algorithm. Step 1 observes the C1 voltage and current, which are the C2 voltage and current, to generate D_C for control of Fig. 7.2(a). Then, Step 2 calculates D_1 from D_C according to (7.4). Gain operators can replace division operators, i.e. $\div E$, if the input voltage is almost constant.

The proposed control is an extension of the PWM-based sliding-mode control shown in Fig. 7.4 because STEP2 is the only difference.

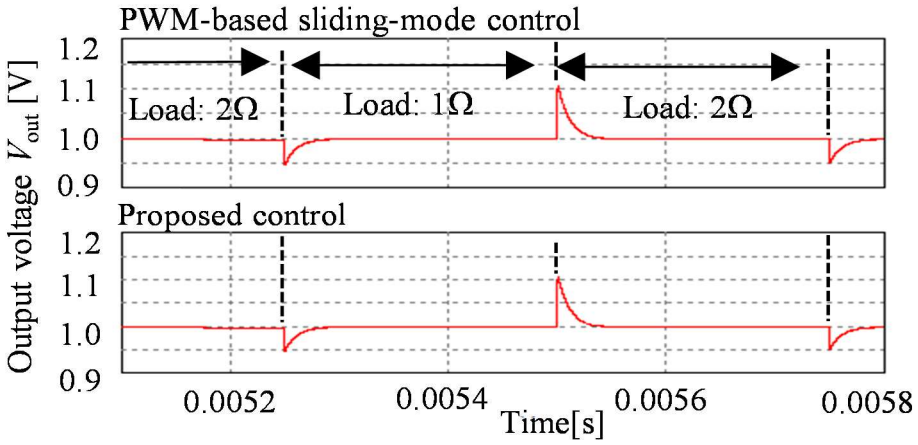

Fig. 7.5. Output voltage under step load change.

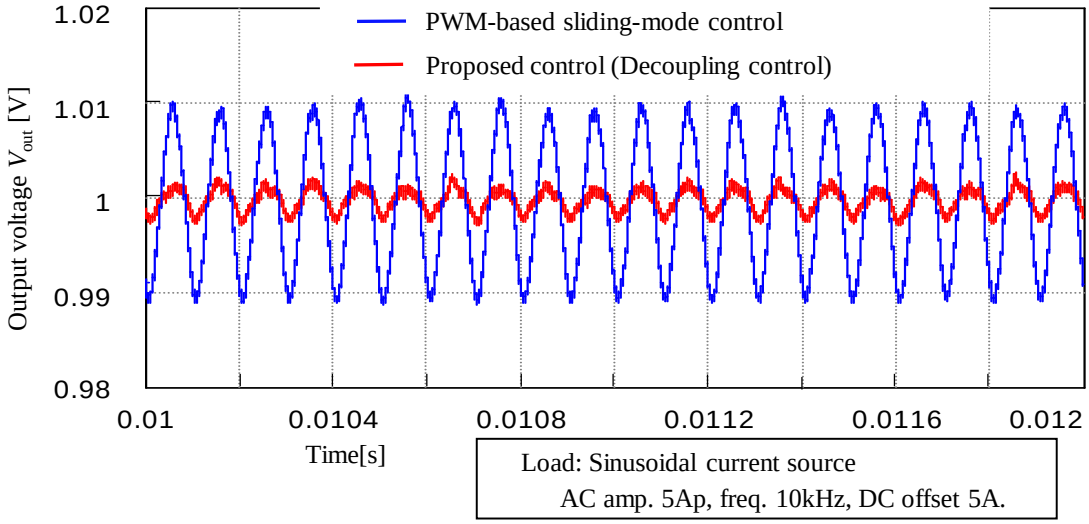

Fig. 7.6. Output voltage under sinusoidal load current.

7. 3. Simulation

Simulation was carried out to confirm effectiveness of the proposed control shown in Fig. 7.3 in comparison with the PWM-based sliding-mode control shown in Fig. 7.4. The simulation parameters are presented in Fig. 7.3. The simulator is PSIM9.3 (Myway Plus Corp.).

Figure 7.5 shows the transient response when the load resistance is switched between 1Ω and 2Ω. The result shows that the proposed control shows almost the same response as the PWM-based sliding-mode control. Therefore, the proposed control showed no improvement in the transient response to a step load change.

Figure 7.6 shows the output voltage fluctuations when the load is sinusoidal current sink with $5A_{peak}$ 10kHz. The output voltage fluctuation was effectively suppressed in the

proposed control. Therefore, the proposed converter improved the dynamic load regulation against slow load current fluctuation.

7. 4. Conclusions

Buck converters are generally required to stabilize the output voltage. To improve the stability, this chapter proposed a novel control method for synchronous buck converters. The proposed control can improve the dynamic load regulation against slow load current fluctuation. Simulation results revealed successful suppression of the output voltage fluctuation under sinusoidal load current, whereas no improvement was found in the transient response to a step load change. In future works, the author will evaluate the performance of the proposed control experimentally.

REFERENCES

[1] S. Abe, M. Hirokawa, T. Zaitsu, and T. Ninomiya, “Stability comparison of voltage mode and peak current mode control for bus converter in on-board distributed power system,” in *Proc. IEEE Annu. Intl. Telecommunications Energy Conf.*, 2006, 32-1, pp.1-5.

[2] S.-C. Tan, Y. M. Lai, and C. K. Tse, “General design issues of sliding-mode controllers in DC-DC converters,” *IEEE Trans. Ind. Electron.*, vol. 55, no. 3, pp. 1160-1174, Mar. 2008.

[3] K. Umetani, “A generalized method for Lagrangian modeling of power conversion circuit with integrated magnetic components”, *IEEJ Trans. Elect. Electron. Eng.*, vol. 7, no. S1, pp. S146-S152 Nov. 2012.

[4] K. Umetani, J. Imaoka, M. Yamamoto, S. Arimura, and T. Hirano, “Evaluation of the Lagrangian Method for Deriving Equivalent Circuits of Integrated Magnetic Components: a Case Study Using the Integrated Winding Coupled Inductor,” *IEEE Trans. Ind. Appl.*, vol. 51, no. 1, pp. 547-555 Jan. 2015

[5] L. D. Landau and E. M. Lifshitz, “Canonical tranformations” in Mechanics, Oxford, U. K.: Butterworth- Heinemann, 1976, pp.143-146.

CONCLUSIONS

Lagrangian dynamics is expected to promote analytical understandings of electric power conversion techniques because it has the following attractive features: 1. It can directly analyzes behavior of the electromagnetic fields rather than the voltage-current relations; 2. It can analyzes the electromagnetic non-linearity; 3. It can analyzes the systems that incorporates the electronics and the mechanics simultaneously. These features are probably essential to extend application of the power electronics to newly developing technical fields such as the integrated magnetic components, the induction heating, the wireless power transfer, the switching reluctance motor drive, the system integration and so on. However, we have few knowledge to apply Lagrangian dynamics to the power electronics, although Lagrangian dynamics has already been widely spread in the mechanical fields.

This thesis addressed this issue by proposing a methodology to apply Lagrangian dynamics to the power electronics. Part I presented four novel basic analytical methods for the power electronics based on Lagrangian dynamics. These methods enables analyses that the conventional circuit theory is difficult to conduct, and are useful for application to the newly developing technical fields. The followings are the main conclusions of Part I.

1. A Lagrangian modeling method of power conversion circuits was presented in Chapter 1. The method can also generates Lagrangian models of circuits that incorporates the complicated magnetic circuits. The proposed method offers easy procedure because the Lagrangian models are directly configurable from the physical structure of the electric and magnetic circuits. Behavior of the circuits can be systematically analyzed by applying the Lagrangian model to the well-known Euler-Lagrange equation. Furthermore, the state-space model of the circuit can also be obtained systematically under a simple predetermined procedure.

2. A Lagrangian method to derive the equivalent circuits of integrated magnetic components was presented in Chapter 2. This method can be expected to derive a simpler circuit than the conventional methods, when applied to an integrated magnetic component with a small number of flux paths that can be magnetized independently. The Lagrangian method was verified theoretically and experimentally by a case study using the integrated winding coupled inductor.

3. A Lagrangian method of the duality transformation was presented in Chapter 3. The conventional methods of the duality transformation suffer from complicated procedures when applied to non-planar circuits; and furthermore, they often suffer from different results, which cannot be derived by the other methods. On the other hand, the Lagrangian method offers a universal and systematic procedure that derives all possible duals. The Lagrangian method is easily applicable to non-planar circuits in the same manner as to planar circuits because it does not need the topological transformation. The Lagrangian method was verified by two examples. One of the examples is a typical non-planar circuit from which the conventional

methods are known to derive either one of two different duals. As a result, the Lagrangian method succeeded to derive both of the two duals deductively.

4. A Lagrangian method to formulate switched reluctance motor models was presented in Chapter 4. The proposed method can model intense magnetic non-linearity of the motors. Furthermore, this model can be connected to the propulsion circuits of the motor and the mechanical system of the load to form a Lagrangian model of the entire motor propulsion system. Therefore, the behavior of the entire system can be analyzed systematically using Euler-Lagrange equation. The formulation of the switched reluctance motor was verified by an example of operation analysis of a simple SRM driving system.

This thesis also gave some examples of these Lagrangian methods applied to practical industrial applications. Part II presented three novel techniques for practical applications in which Lagrangian dynamics took an essential role. The followings are the main conclusions of Part II.

1. A novel integrated magnetic component for EMC filters was developed and proposed in Chapter 5. The integrated magnetic components are expected to miniaturize EMC filters. However, conventional magnetic structures suffer from lowers tolerance to the magnetic saturation, which may reduce the miniaturization effect by the magnetic integration. Chapter 5 utilizes Lagrangian dynamics to analyze the proposed magnetic structure that improves the tolerance to the magnetic saturation. A theoretical analysis and experiments verified the operating principle of the proposed structure. Additionally, an analytical estimation revealed that the proposed structure successfully reduced the core volume by 41% compared with a conventional magnetic structure.

2. A novel soft-switching boost chopper with an integrated magnetic component was developed and proposed in Chapter 6. The integrated magnetic component is utilized for miniaturizing a novel lossless LC snubber in the proposed chopper which achieves the zero-current switching turn-on and the zero-voltage switching turn-off. Chapter 6 utilizes Lagrangian dynamics to develop the integrated magnetic component. Experiments successfully verified the operating principles of the proposed chopper as well as efficiency improvement by the soft-switching.

3. A novel control method for synchronous buck converters was developed and proposed in Chapter 7. Sliding-mode control for buck converters is beneficial in fast transient response to a step load change in wide operating range. The proposed control method further improved dynamic load regulation against load current fluctuations within the response speed of the converters. Simulation results revealed successful suppression of the output voltage fluctuations under sinusoidal load current.

ACKNOWLEDGEMENT

Foremost, I would like to express my sincere gratitude to my advisor, Prof. Masayoshi Yamamoto for continuous support of my Ph. D. study and research. His remarkable enthusiasm motivated me and sustained my interests into power electronics researches. As a result, I was motivated to enter the Ph. D. course and to begin a career as a professional researcher. His guidance helped me all the time in my Ph. D. course in Shimane University.

Besides, I would like to thank Prof. Eiji Hiraki for warm support of my Ph. D. study, encouragement, and insightful comments.

I would also like to thank Takanari Sasaya and Tomonori Kimura for their permission to enter the Ph. D. course during my career in DENSO Corporation and for their helpful comments to improve quality of my research papers.

My sincere thanks also goes to colleagues in DENSO Corporation: Keisuke Yagyu, Iwamoto Fujiyuki, Takahiro Tera, Kazuhiro Shirakawa, Dr. Seikoh Arimura, Hiroshi Taki and Tetsuo Hirano for helpful discussions, stimulating collaboration, and hard work before deadline. I really enjoyed working with them.

Many thanks go to Prof. Barry Roser for improving the English quality of my research paper related to Chapter 2.

Thanks also go to my labmates in Power Electronics Laboratory, Shimane University, for creative discussions and collaborations. Special thanks to Jun Imaoka, Wilmar Martinez, Hirokatsu Umegami, Humiya Hattori, Masato Sasaki, Taiki Tanada, Masashi Hama, Taichi Kawakami, Yuki Itoh, Yasuo Sasaki, Masaki Ishihara for their great contribution and cooperation in research.

Finally, I would like to thank my family, my wife Junko Umetani, and my son Haruki Umetani, my parents Dr. Takehiko Umetani and Kyoko Umetani, and my wife’s parents Hideaki Nakai and Kazuko Nakai, for big spiritual support throughout my life.